

**Titre:** An Anatomically-Realistic Simulation Framework for Ultrasound  
Title: Localization Microscopy

**Auteur:** Hatim Belgharbi  
Author:

**Date:** 2021

**Type:** Mémoire ou thèse / Dissertation or Thesis

**Référence:** Belgharbi, H. (2021). An Anatomically-Realistic Simulation Framework for  
Citation: Ultrasound Localization Microscopy [Master's thesis, Polytechnique Montréal].  
PolyPublie. <https://publications.polymtl.ca/9734/>

 **Document en libre accès dans PolyPublie**  
Open Access document in PolyPublie

**URL de PolyPublie:** <https://publications.polymtl.ca/9734/>  
PolyPublie URL:

**Directeurs de  
recherche:** Jean Provost  
Advisors:

**Programme:** Génie biomédical  
Program:

**POLYTECHNIQUE MONTRÉAL**

affiliée à l'Université de Montréal

**An Anatomically-Realistic Simulation Framework for Ultrasound  
Localization Microscopy**

**HATIM BELGHARBI**

Institut de génie biomédical

Mémoire présenté en vue de l'obtention du diplôme de *Maîtrise es sciences appliquées*

Génie biomédical

Décembre 2021

**POLYTECHNIQUE MONTRÉAL**

affiliée à l'Université de Montréal

Ce mémoire intitulé :

**An Anatomically-Realistic Simulation Framework for Ultrasound  
Localization Microscopy**

présenté par **Hatim BELGHARBI**

en vue de l'obtention du diplôme de *Maîtrise ès sciences appliquées*

a été dûment accepté par le jury d'examen constitué de :

**Samuel KADOURY**, président

**Jean PROVOST**, membre et directeur de recherche

**Hassan RIVAZ**, membre

## ACKNOWLEDGEMENTS

First, I would like to thank Jean Provost for introducing me to research during my undergraduate studies and for giving me the opportunity to undertake this exciting project. In an environment favoring learning, cohesion and teamwork, Jean's availability and continuous support were greatly helpful on either technical, academic, and professional levels. Most importantly, Jean always had my best interests at heart and for that I will forever be grateful.

I would also like to thank Frederic Lesage for his invaluable insight, prompt responses, and unwavering readiness to help.

I would also like to thank my lab colleagues for the various challenging discussions which contributed to keeping a pleasant working environment. Namely, Jonathan Porée for being an excellent advisor in various ultrasound-related topics, Rafat Damseh for his availability and advice for inquiries about graph modeling, Patrick Delafontaine-Martel for his advice on two-photon microscopy, Vincent Perrot for his precious mentoring, Chloé Bourquin for being an amazing experiment partner and advice on presentations, Samuel Desmarais for being an amazing friend and for the help in various projects, and Léo Milecki for the great discussions we had. To all lab members, I say thank you.

Finally, I thank my mother, father, brother, and sister, who constantly and unconditionally supported me throughout my endeavors and helped me build character striving for excellence.



## RÉSUMÉ

En imagerie vasculaire in-vivo, on tente d'élucider un réseau vasculaire très complexe mais a priori inconnu. Des cartographies impressionnantes de la vascularisation tissulaire sont obtenues à l'aide de la microscopie de localisation par ultrasons (ULM) en suivant des microbulles (MB) à travers des milliers, voire des centaines de milliers d'images. En revanche, les études de validation pour les systèmes d'imagerie n'ont été validés que sur des fantômes composés de tubes ou de microcanaux qui ne reflètent pas la complexité de la vascularisation tissulaire ont été réalisées dans des conditions in-vitro ou in-vivo où les positions de MBs sont inconnues. Des fantômes réalistes réalisés en simulation sont essentiels pour valider la précision de la cartographie vasculaire et optimiser les paramètres, car les positions de MBs de références sont disponibles pour quantifier l'erreur de localisation. Établir la concentration en MBs optimale est un représente un défi, car elle peut être augmentée pour réduire le temps nécessaire pour peupler le réseau vasculaire, mais elle doit rester suffisamment faible pour éviter les interactions indésirables entre les microbulles, ce qui causerait un flou dans l'image résultante. Sans image ou réseau vasculaire de référence, il est très difficile d'évaluer la précision d'un système d'imagerie dans des environnements in-vivo. Par conséquent, un cadre de simulation anatomiquement et hémodynamiquement réaliste a été développé utilisant des données de cerveau de souris in-vivo acquises par microscopie à deux photons. Ce cadre permet de tester en simulation divers paramètres d'acquisition tout en ayant accès à une vérité terrain hautement résolue pour l'évaluation de la performance de la cartographie vasculaire. A partir d'un modèle en graphe, un simulateur de trajectoires de particules a été conçu pour reproduire un flux de microbulles similaire à des données in-vivo. Le simulateur permet d'obtenir des positions de MBs de référence qui peuvent ensuite être utilisées pour simuler des signaux et des images ultrasonores et sur lesquelles des métriques peuvent être calculées pour évaluer la précision de la cartographie vasculaire. A titre d'exemple, le temps d'acquisition a été calculé en fonction de diverses fréquences de transmission de sondes et de diverses concentrations de MBs. Un lien entre la concentration maximale de microbulles et le volume de la réponse impulsionnelle a été établi, où la concentration optimale de microbulles peut être calculée pour obtenir la meilleure reconstruction vasculaire d'un système d'imagerie. Le cadre développé peut donc être utilisé pour des études paramétriques pour la validation d'algorithmes de formation d'images ULM.

## ABSTRACT

In in-vivo vascular imaging, we try to shed light on a very complex, yet unknown vascular network. Impressive mappings of tissue vasculature are achieved using Ultrasound Localization Microscopy (ULM) by following microbubbles (MB) through thousands to hundreds of thousands of images. However, all the validation studies for imaging systems were performed in in-vitro or in-vivo settings, where MB positions were unknown. Realistic simulation phantoms are essential to validate the accuracy of vascular mapping and parameters' optimization since reference MB positions are available. MB concentration is an example of a challenging parameter, since it can be increased to reduce the time needed to populate the vascular network but must remain low enough to avoid unwanted interactions between microbubbles which would cause unwanted blurring of the resulting image. Without a reference vascular network, it is very challenging to assess the accuracy of an imaging system in in-vivo settings. Therefore, we developed an anatomically and hemodynamically realistic simulation framework using in-vivo mouse brain data acquired with two-photon microscopy that allows us to test in simulation various acquisition parameters while having access to a highly resolved ground truth for performance assessment. From a graph model, a particle flow simulator was designed to reproduce a microbubble flow that is similar to in-vivo settings. The designed simulator allows to obtain reference microbubble positions that can be then used to simulate ultrasound signals and reconstruct images on which metrics can be computed to assess the accuracy of the vascular mapping. As an example application, acquisition time was computed as a function of various probe transmit frequencies and various MB concentrations. A link between the maximal microbubble concentration and the volume of the impulse response system was established, from which optimal microbubble concentration can be computed to obtain the best vascular reconstruction of an imaging system. The developed framework can therefore be used for parametric studies for the validation of ULM image formation algorithms.

## TABLE OF CONTENTS

ACKNOWLEDGEMENTS .....	III
RÉSUMÉ.....	IV
ABSTRACT .....	V
TABLE OF CONTENTS .....	VI
LIST OF TABLES .....	IX
LIST OF FIGURES.....	X
LIST OF SYMBOLS AND ABBREVIATIONS.....	XII
CHAPTER 1 INTRODUCTION.....	1
1.1 Motivation .....	2
1.2 Objectives.....	5
1.2.1 Publications .....	5
1.2.2 Presentations.....	6
CHAPTER 2 LITTERATURE REVIEW .....	8
2.1 Fundamentals of ultrasound imaging .....	8
2.1.1 Physical principles.....	8
2.2 Ultrasound localization microscopy .....	27
2.2.1 Major events in ULM.....	27
2.2.2 Ultrasound localization microscopy characteristics .....	29
2.3 Flow simulation.....	39
CHAPTER 3 METHODOLOGY .....	41
3.1 Simulation pipeline .....	41
3.1.1 Serial 2-photon data processing .....	41
3.1.2 Microbubble flow simulation.....	42

3.1.3	Ultrasound localization microscopy .....	48
3.2	Parametric studies .....	49
3.2.1	Metrics.....	49
CHAPTER 4 ARTICLE 1: AN ANATOMICALLY AND HEMODYNAMICALLY REALISTIC SIMULATION FRAMEWORK FOR 3D ULTRASOUND LOCALIZATION MICROSCOPY .....		51
4.1	Abstract .....	51
4.2	Introduction .....	52
4.3	Methods .....	55
4.3.1	In-vitro two-photon microscopy.....	55
4.3.2	Graph model.....	55
4.3.3	Particle trajectory generation .....	55
4.3.4	Steady-state flow .....	57
4.3.5	Scatterers' arrangement.....	58
4.3.6	Ultrasound Simulation.....	59
4.3.7	ULM image formation algorithm.....	59
4.3.8	MB simulator metrics.....	60
4.3.9	ULM metrics .....	61
4.4	Results .....	62
4.4.1	Simulated MB trajectories statistics match in-vivo data.....	62
4.4.2	Localization error is more sensitive to concentration at lower transmit frequency ...	64
4.4.3	Acquisition time is drastically reduced at higher transmit frequency .....	66
4.4.4	Higher concentrations reduce reconstruction fidelity .....	66
4.4.5	Maximal MB concentration is PSF size dependent .....	68

4.4.6	PSF volume dictates effective reconstruction time .....	68
4.5	Discussion .....	69
4.5.1	MB simulation.....	70
4.5.2	MB localization.....	70
4.6	Limitations .....	72
4.7	Conclusion.....	74
4.8	References .....	74
CHAPTER 5	GENERAL DISCUSSION.....	79
5.1	Develop an anatomically-realistic framework for the validation of Ultrasound Localization Microscopy in a mouse model. ....	79
5.2	Establish a link between optimal MB concentration and acquisition parameters of an imaging setup. ....	80
CHAPTER 6	CONCLUSION AND RECOMMANDATIONS .....	82
REFERENCES	.....	83

## LIST OF TABLES

Table 1: Current and potential metrics using ULM microbubble positions in time .....	3
Table 2: Comparison of a typical 128-element linear array and a custom 32x32 matrix array .....	22
Table 3: Acquisition parameters of a typical 128-element linear array, a custom 32x32 matrix array and a typical 32x32 matrix array .....	25
Table 4: FDA-approved and commercially available MBs. Adapted from [90]. .....	30
Table 5: Acquisition parameters .....	58

## LIST OF FIGURES

Figure 1: Example of microvascular mapping of a rat brain using Ultrasound Localization Microscopy. Courtesy of Jonathan Porée.....	2
Figure 2: Coordinate system of a matrix array probe for 3D ultrasound imaging.....	9
Figure 3: Example of two emission modes. (Left) Plane wave emission. (Right) Focused emission. .....	11
Figure 4: Ultrasound raw signal processing in temporal and frequency domains. Extracted from [67] .....	14
Figure 5: Dimensions and distances in a linear array.....	15
Figure 6: 3D Planewave imaging.....	19
Figure 7: Norm of the lower bound on localization error at different values of SNR for a 32x32 6 MHz matrix array probe.....	26
Figure 8: Norm of the lower bound on localization error at different transmit frequencies for a 32x32 matrix array probe. SNR = 10 dB. ....	26
Figure 9: Timeline of major events in ULM .....	27
Figure 10: Selected research groups in ULM on a world map .....	29
Figure 11: Ultrasound localization microscopy framework. Adapted from [86].....	32
Figure 12: MB steady-state flow simulation at three consecutive timeframes. ....	45
Figure 13: Raw MB positions of multiple timeframes accumulated in space to better visualize the Poiseuille parabolic velocity distribution.....	45
Figure 14: Pulsatile flow modulation for a mouse heart beating at 300 BPM.....	46
Figure 15: MB steady-state flow simulation. White dots represent individual MBs' velocities. They are only visible at a certain velocity threshold to visualize the propagation of the pulsatile flow. Snapshots from 1 to 3 correspond to three timestamps in a cardiac cycle (Figure 14).	46

Figure 16: Wave propagation illustration. (Top) Two views of a MB steady-state flow simulation with two regions of interest (ROI) used to calculate MB mean velocity at two locations along a vessel. (Middle) Zoomed views on ROIs. (Bottom) Mean MB velocity in each ROI.....47

Figure 16: Localization error vs 3D position for a single MB using a 32x32 matrix array with a transmit frequency of 6 MHz. Scale was normalized as a function of the transmit wavelength ( $\lambda \sim 257 \mu\text{m}$ ). Small black circle at the bottom represent the position of the elements of the transducer facing up towards the medium. Only one quadrant was computed because of x and y symmetry.....49

Figure 17: Norm of the lower bound on localization error at different values of SNR for a 32x32 6 MHz matrix array probe. The blue dashed line represents results from the ULM framework and the solid black represents the theoretical values extracted from equations (41)-(42). ....50

Figure 18: Unique microbubbles positions were randomly distributed in a  $10 \times 10 \times 10$  pattern to span over  $5 \times 5 \times 6.5$  mm. This example shows 1 million MB distributed in 1000 sub-regions, which results in 1000 MB in each sub-region. Even though fewer small vessels are present in each sub-region, this step is essential since the PSF is not uniform in the field of view and it also allows to span a usable MB concentration range. After the ULM framework and metrics computation, MB positions in sub-regions can be added back together in the original size volume to emulate a longer acquisition time for visualization purposes. ....57



## **LIST OF SYMBOLS AND ABBREVIATIONS**

2D	Two dimensions
3D	Three dimensions
2PM	Two-photon microscopy
FDA	Food and drug administration
MB	Microbubble
ms	Millisecond
PALM	Photo-acoustic localization microscopy
PSF	Point spread function
SNR	Signal to noise ratio
ULM	Ultrasound localization microscopy

## Chapter 1 INTRODUCTION

In ultrasound localization microscopy (ULM), microbubbles (MB) are used as a contrast agent and are injected into the bloodstream prior to imaging. The MBs consist of a gas surrounded by a lipid, lipopolymer, or polymer shell. They are nontoxic, approved by the FDA [1], and routinely used in clinic. Their appeal is mainly due to a large impedance difference that is created between tissue and gas, and resonant properties, which makes them highly echogenic. Put simply, we can easily isolate them from the surrounding tissue and track them individually.

In conventional ultrasound imaging, we are generally interested in imaging tissue or anatomical landmarks that are composed of densely packed scatterers and interfaces. The propagation of an ultrasonic pulse through interfaces and scatterers results in reflected and diffracted waves. These waves interfere with each other depending on their relative phase. The ability to distinguish between two anatomical structures is linked to the diffraction limit stated by the Rayleigh criterium [2]. This spatial resolution limit is in the order of the wavelength, which in the case of the ultrasonic pulse is in the order of 100-500 micrometers ( $\mu\text{m}$ ) for commonly used transmit frequencies of 3-15 MHz.

As opposed to tissue, a MB can be a single scatterer, and its exact location can be computed (Section 2.2.2.6). In ULM, we leverage that fact by acquiring images where only a few MBs are present to avoid interactions between microbubbles. For seconds or minutes, hundreds to thousands of images per second are acquired. After isolating and computing MB positions, we can add all MB positions together in that time period to map their trajectories. Since MBs only navigate in blood vessels, this allows us to map the vascular network at the micrometer scale (Figure 1) [3]–[6].

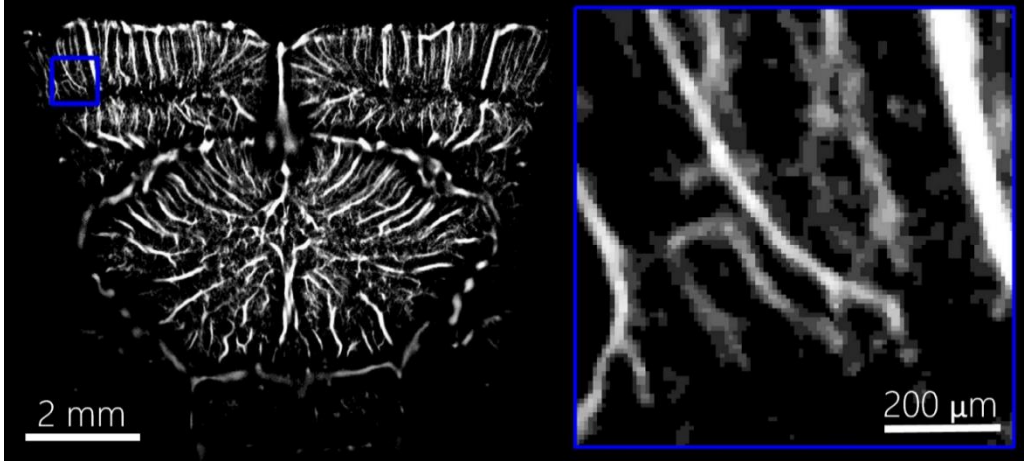


Figure 1: Example of microvascular mapping of a rat brain using Ultrasound Localization Microscopy. Courtesy of Jonathan Porée.

## 1.1 Motivation

Preclinical microvascular imaging using ULM was performed in various animal models, such as the mouse [7]–[9], rat [3], [10]–[15], rabbit [16]–[18] and chicken embryo [19], [20], in multiple tissues including brain, tumor, kidney, ear, skeletal muscle and lymph node. As for human pilot studies, ULM was performed in breast tumors [8], [21], [22], prostate tumors [23], lower limb [24], liver, pancreas, kidney [22] and brain [25].

Current issues related to ULM imaging include a long acquisition time and limited knowledge on MB optimal concentration. Since we need to accumulate data in the time domain, the position of the probe must stay constant during the whole acquisition, which can last several seconds and even minutes. The acquisition time and MB concentration are closely linked, since the higher the count of isolated MBs is in the image, the less time is required to populate the vascular network [6]. Even though short acquisition time and motion correction can mitigate the challenges that arise from involuntary movement and possible breathing [22], in-vivo validation of the produced images remains a challenge.

As for potential applications of ULM, we can look at the output data from the ULM framework. This output data consists of MB spatial positions in space and time. This information can be turned into biomarkers depending on the domain of validity and accuracy of the data and biomarker in question. Potential biomarkers can be derived from the accumulation of absolute MB positions,

from MB velocities and even from MB acceleration. For instance, the accumulation of absolute MB positions, also known as density maps, reflect the anatomical vasculature, while MB velocities combined with vessel diameter can reflect blood flow. Biomarker development can also include inspiration from other vascular imaging modalities such as diffusion MRI [26]–[30], two-photon imaging [31], [32], computed tomography [33], just to name a few. Table 1 reflects current and potential metrics that can be leveraged from ULM MB positions in time.

Table 1: Current and potential metrics using ULM microbubble positions in time

MB positions' accumulation	MB velocity	MB acceleration
Vascular density [31], [34]–[36]	Blood flow [6] <sup>1</sup>	Pulsatility <sup>2</sup> [37]
Vascular size distribution [32], [34], [35]		
Vascular tortuosity [11], [38]		

Metrics can be leveraged to develop biomarkers if they are proven to be an indicator for a clinical condition. For example, vascular density and tortuosity was shown to differentiate between tumor and healthy tissue [39].

The validation of ULM image formation algorithms is essential to establish the limitations of metrics and practices to optimize for biomarkers' accuracy.

In the literature, attempts to quantify ULM limitations were performed using rudimentary flow phantoms, simple microfluidic channels [40]–[43][41], or in-vivo using a chicken embryo [19], however, in none of these studies the MB positions were known. To our knowledge, there is no

---

<sup>1</sup> Requires vessel diameter from a density map

<sup>2</sup> Computed using velocity differential in a cardiac cycle

anatomically-realistic validation framework for ULM capable of replicating the interactions between MBs that occur in *in-vivo* settings while having access to reference MB positions. This means that current vascular maps from ULM setups may not precisely or fully reflect the vascular network since we cannot quantify the error committed when localizing MBs' positions.

Hence, this project was conducted to shed light on the current limitations of ULM and provide us with guidelines to achieve optimal vascular reconstruction. In practice, we developed a framework capable of simulating an anatomically-realistic flow of MBs, which can be used to populate a medium of scatterers in an ultrasound simulation. Then, ultrasound signals are reconstructed into either 2D images or 3D volumes, where MBs can be precisely detected and accumulated over time to generate vascular maps. Because we possess known MB positions and detected MB positions, we can quantify localization error and other metrics assessing the performance of our imaging system. Using this framework, parametric studies can be undertaken. For instance, we can change MB concentration – as would a clinician by changing the volume of injected MBs – and determine if there is an optimal concentration range for specific acquisition parameters. This is essential since MB concentration plays an important role in the acquisition time and fidelity of the vascular reconstruction. We can also quantify the percentage of vessels that we are able to map compared to the complete vascular network based on different ultrasound probe parameters, such as transmit frequency. To sum up, this work can be used as a guide for choosing optimal MB concentration for a specific imaging setup to achieve the best possible vascular reconstruction. Ultimately, this would allow for more precise biomarkers that would enable more precise diagnoses and monitoring in vascular imaging.

## 1.2 Objectives

The objective of this project is therefore to develop an anatomically-realistic framework for the validation of Ultrasound Localization Microscopy that can be used to conduct parametric studies capable of quantifying ULM image formation algorithms' limitations and optimal parameters. Our two specific aims are as follows:

Objective 1: Develop an anatomically-realistic framework for the validation of Ultrasound Localization Microscopy in a mouse model.

Objective 2: Establish a link between optimal MB concentration and acquisition parameters of an imaging setup.

These objectives led to the following publications and presentations.

### 1.2.1 Publications

H. Belgharbi, J. Porée, R. Damseh, L. Milecki, P. Delafontaine-Martel-, F. Lesage, J. Provost, “An Anatomically and Hemodynamically Realistic Simulation Framework for 3D Ultrasound Localization Microscopy”. Submitted to bioRxiv on October 9<sup>th</sup> and IEEE Transactions on Medical Imaging on October 10<sup>th</sup>, 2021. BioRxiv link : <https://doi.org/10.1101/2021.10.08.463259>

J. Porée, L. Milecki, H. Belgharbi, C. Bourquin, F. Lesage, J. Provost, “A Deep Learning Framework for Spatiotemporal Ultrasound Localization Microscopy “ <https://ieeexplore.ieee.org/document/9345725>. Published on IEEE Transactions on Medical Imaging, 2020.

E. Hardy, J. Porée, H. Belgharbi, C. Bourquin, F. Lesage, J. Provost, “Sparse Channel Sampling for Ultrasound Localization Microscopy (Sparse-ULM) “ <https://iopscience.iop.org/article/10.1088/1361-6560/abf1b6>. Published on Physics in Medicine and Biology, 2020.

### 1.2.2 Presentations

e-Flash Talk – IEEE IUS 2021 – Virtual Symposium 2021

**H. Belgharbi**, J. Porée, R. Damseh, V. Perrot, L. Milecki, P. Delafontaine-Martel-, F. Lesage, J. Provost,

“PSF Volume Dictates Optimal Microbubble Concentration and Acquisition Time in Ultrasound Localization Microscopy”

e-Lecture – IEEE IUS 2021 – Virtual Symposium 2021

Chloé Bourquin, Vincent Perrot, Jonathan Porée, **Hatim Belgharbi**, Nelson Cortés, Géraldine Miquel, Samuel Bélanger, Hugo Ladret, Lamyae Ikan, Christian Casanova, Eric Thorin, Frédéric Lesage, Jean Provost,

“3D Dynamic Ultrasound Localization Microscopy In Vivo Validation in Normal and Pathological Animal Models”

e-Lecture – IEEE IUS 2021 – Virtual Symposium 2021

Brice Rauby, Jonathan Porée, **Hatim Belgharbi**, Chloé Bourquin, Maxime Gasse, Jean Provost, “3D Spatiotemporal Ultrasound Localization Microscopy Using Deep Learning”

e-Flash Talk – IEEE IUS 2021 – Virtual Symposium 2021

A. Wu, V. Perrot, J. Porée, **H. Belgharbi**, M. Chassé, J. Provost. Aberration Correction in “Ultrasound Localization Microscopy Using a Spatiotemporal Matrix Image Formation Framework”.

e-Flash Talk – My Thesis in 180 Seconds – IVADO 2021

**H. Belgharbi**, J. Porée, R. Damseh, V. Perrot, L. Milecki, P. Delafontaine-Martel-, F. Lesage, J. Provost,

“PSF Volume Dictates Ultrasound Localization Microscopy”

e-Flash Talk – Virtual Scientific Days 2021 – Quebec Bio-Imaging Network 2021

**H. Belgharbi**, J. Porée, R. Damseh, V. Perrot, L. Milecki, P. Delafontaine-Martel-, F. Lesage, J. Provost,

“An Anatomically-Realistic Simulation Framework for Ultrasound Localization Microscopy”

e-Presentation – Imagining Imaging Symposium, Sherbrooke, QC, Canada 2020

**H. Belgharbi**, J. Porée, R. Damseh, L. Milecki, P. Delafontaine-Martel-, F. Lesage, J. Provost,

“An Anatomically-Realistic Simulation Framework for Ultrasound Localization Microscopy”

e-Poster – 2020 IEEE International Ultrasonics Symposium, Las Vegas, NV, US 2020

**H. Belgharbi**, J. Porée, R. Damseh, L. Milecki, P. Delafontaine-Martel-, F. Lesage, J. Provost,

“An Anatomically-Realistic Simulation Framework for Ultrasound Localization Microscopy”  
e-Presentation – 2020 IEEE International Ultrasonics Symposium, Las Vegas, NV, US 2020

J. Porée, L. Milecki, **H. Belgharbi**, C. Bourquin, F. Lesage, J. Provost,

“A Deep Learning Framework for Spatiotemporal Ultrasound Localization Microscopy “  
e-Poster – 2020 IEEE International Ultrasonics Symposium, Las Vegas, NV, US 2020

E. Hardy, J. Porée, **H. Belgharbi**, C. Bourquin, F. Lesage, J. Provost,

“Sparse Channel Sampling for Ultrasound Localization Microscopy (Sparse-ULM) “  
Poster – RBIQ Annual Scientific Day, Montreal, QC, Canada 2020

**H. Belgharbi**, J. Porée, R. Damseh, L. Milecki, P. Delafontaine-Martel-, F. Lesage, J. Provost,

“An Anatomically-Realistic Simulation Framework for Ultrasound Localization Microscopy”  
Presentation – 178<sup>th</sup> Acoustical Society of America Meeting, San Diego, CA, US2019

**H. Belgharbi**, J. Porée, R. Damseh, L. Milecki, P. Delafontaine-Martel-, F. Lesage, J. Provost,

“An Anatomically-Realistic Simulation Framework for Ultrasound Localization Microscopy”  
Presentation – 2019 IEEE International Ultrasonics Symposium, Glasgow, UK 2019

C. Bourquin, **H. Belgharbi**, P. Cormier, E. Hardy, M. Gesnik, G. Cloutier, F. Lesage, J. Provost,

“Pulsatility mapping using time-resolved ultrasound localization microscopy in the rodent’s brain  
in vivo”



## Chapter 2 LITTERATURE REVIEW

### 2.1 Fundamentals of ultrasound imaging

The first published article on medical ultrasound dates to 1942 and was written by the Austrian doctor Karl Theodore Dussik [44]. Today, ultrasound imaging and therapeutics can be seen in almost every field of medicine, from prevention, diagnosis, prognosis, monitoring, palliative care, and treatment. As for diagnostic ultrasound, it includes abdominal and pelvis sonography, small parts, carotid artery, and peripheral vessel sonography, obstetric and fetal sonography, pediatric sonography [45], eye scanning, extracranial & transcranial ultrasonography, skin & subcutaneous tissue scanning, echocardiography [46] and functional imaging [47], [48]. As for ultrasound therapeutics, it can induce effects through heating, ultrasonic cavitation, gas body activation, mechanical stresses or other undetermined processes [49]. Example applications include cancer therapy [50], cardiac ablation [51], blood brain barrier opening [52], neuromodulation [53], stone removal [54], blood clot breakdown [55], just to name a few. Each field is bound by specific limitations including 1) required penetration depth, 2) required spatial resolution, 3) contrast agent concentration, 4) motion, 5) target tissue accessibility. We will see from the ground up how do we generate an ultrasonic pulse, receive the backscattered signal, and reconstruct it to obtain spatial information about structures insonified by the original pulse.

#### 2.1.1 Physical principles

Ultrasound waves are mechanical waves. These waves transport energy in the form of a pressure propagation. The pressure variation in time is sinusoidal and is described with a frequency of oscillation  $f$  or a wavelength  $\lambda$  linked with the propagation velocity  $c$ .

$$\lambda = \frac{c}{f} \quad (1)$$

The ultrasound name arises from the fact that the frequency of oscillation is higher than the ear's maximum perceptible frequency of about 20 kHz. Medical ultrasound frequencies range from 1 MHz to 30 MHz, where 3-15 MHz is most common.

In practice, when the ultrasound wave meets an interface with a different acoustic impedance (measure of the opposition that a system presents to the propagation of a pressure wave), a few things can occur [56]:

- 1) Most of the energy is transmitted to the second medium.
- 2) A part of the energy is reflected as specular reflection or diffusion (more details in section 0).
- 3) Refraction.
- 4) Cavitation can occur if the negative pressure exceeds ambient hydrostatic pressure, which will result in a temporary void being created. Collapse of this void is what can cause other complications or can be harnessed for surgical and medical purposes [57].
- 5) Lastly, the energy can be transferred to the molecules in the form of heat.

An ultrasound probe is composed of piezoelectric elements disposed either linearly, in a curved manner, as a stack of rows and columns, or in a matrix disposition as in Figure 2. Piezoelectric elements are used since they deform when excited with an electrical current, which induces pressure on the medium.

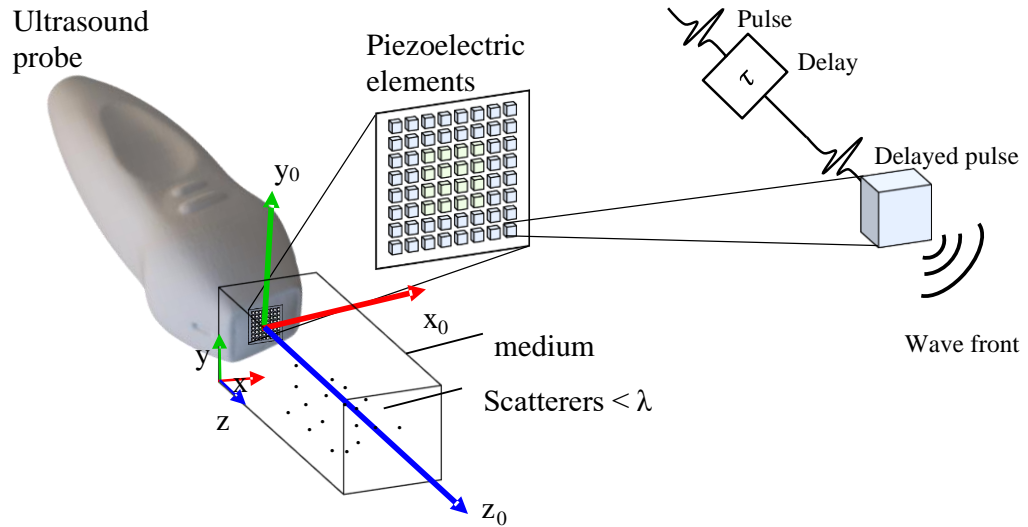


Figure 2: Coordinate system of a matrix array probe for 3D ultrasound imaging.

A mechanical wave is generated from the applied pressure, and it will propagate in the medium and will interact with scattering elements in the medium. The conventional ultrasound probe only

contains a linear array in the x axis, which permits 2D imaging in the z-x plane. In Figure 2, the coordinate system of an imaging system is depicted on a matrix array probe capable of imaging 3D data and a simplified schematic on piezoelectric activation using a delayed pulse. The x, y and z dimensions are referred to as follows:

- z: axial dimension (direction of plane wave propagation without steering)
- x: lateral dimension (dimension where lie transducer elements in a conventional array)
- y: elevation dimension

Other probe arrangements are possible for 3D imaging, namely the row-column disposition [48] and sparse array [58].

A pulse is a short sinusoidal function used to excite the piezoelectric element. It is characterized by its frequency content and length. Since the pulse is a finite function in the time domain and we want it to exhibit certain properties in the frequency domain, it is multiplied by a windowing function referred to as an apodization function such as the popular Hann and Blackman windows [59]. Electronic delays are applied to act on the timing of the pulse, which applied to a series of elements controls the shape of the wave front.

#### **2.1.1.1 Emission and reception of an ultrasonic wave**

The ultrasound scanner contains a transmit waveform generator capable of controlling the waveform, delays ( $\tau_i$ ) applied to each element independently and which elements are going to be active (apodization). All this information is programmed in advance in the scanner. Depending on the sequence of delays, we can generate different types of wavefronts. For example, we can focus the wave front at a specific point in space (Figure 3 a), or generate a wavefront that propagates as a line (2D) or as a plane (3D) for planewave imaging, where the focus point is infinitely far. We can also steer this wavefront at an angle  $\alpha$  from the transducer (Figure 3 b).

After the emission of the ultrasound wave, the ultrasound scanner is programmed to activate the sampling of received signals. A portion of the wave energy it is propagated back by scatterers in the medium and generate electrical signals when applying pressure on the piezoelectric elements. The scanner contains a time-dependent amplifier to compensate signal attenuation farther from the transducer, an analog-to-digital converter (ADC) to sample the signal, digital filters to reshape the

frequency spectrum and then written on local memory. The signal corresponds to raw radiofrequency (RF) data that is sent to the computer for image reconstruction (beamforming) where contributions of different echoes are summed in pixels or voxels from which they came from (Figure 3 c).

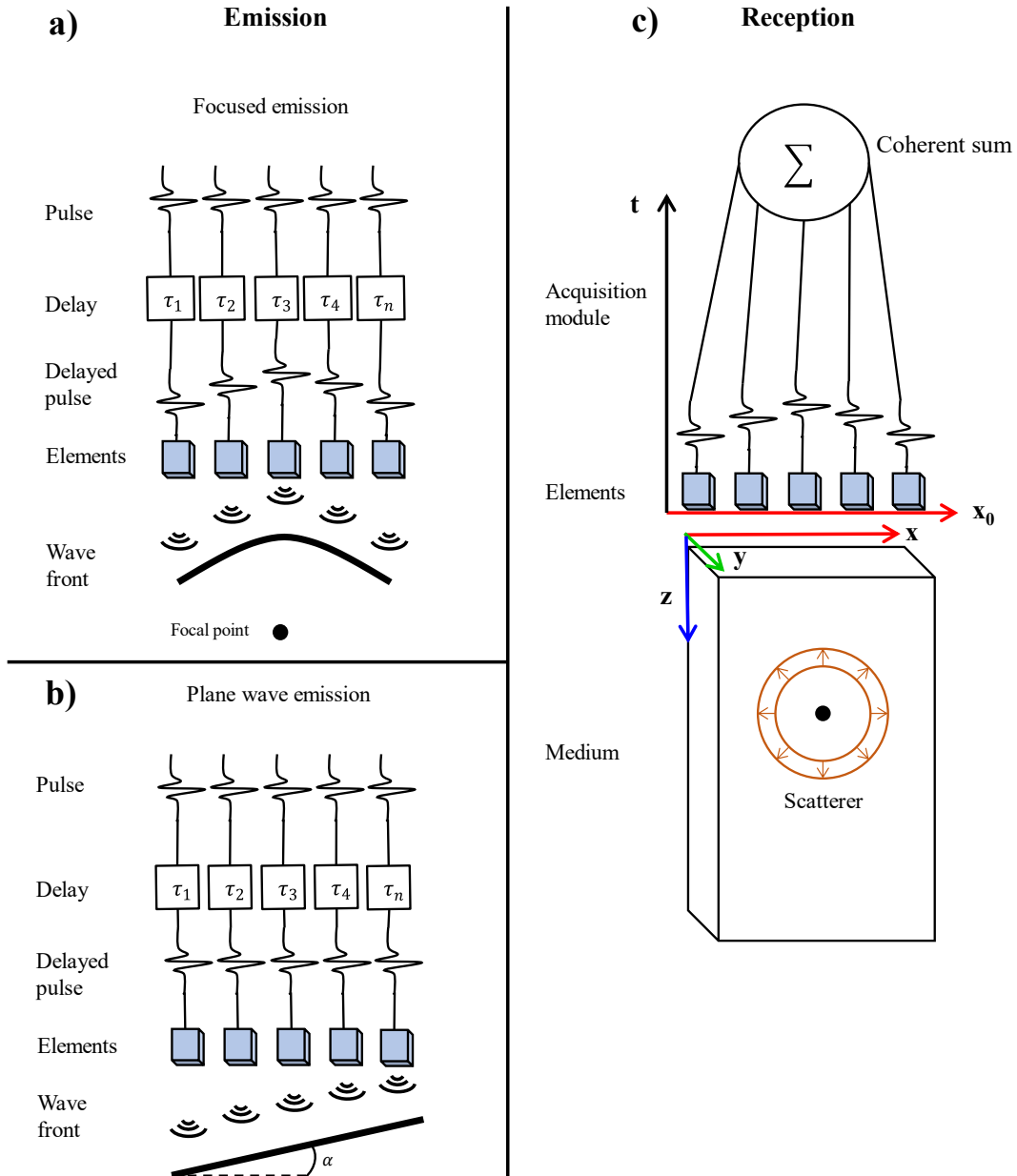


Figure 3: Example of two emission modes. (Left) Plane wave emission. (Right) Focused emission.

Emissions and receptions are cycled in time and this process is usually quantified with the pulse repetition frequency ( $PRF$ ), which is limited to the time of flight of the longest round trip between the elements and the farthest point in the medium ( $d_{max}$ ). We usually take  $d_{max}$  as the diagonal from the first element and opposite furthest corner of the defined medium.

$$PRF = \frac{c}{2d_{max}} \quad (2)$$

### 2.1.1.2 Propagation

In general, a wave can be defined as a field that is characterized by the wave propagation equation below. We will use the pressure field  $p$  in a point of space  $r$  and time  $t$ , where the wave propagates at a velocity  $c$ . We will simplify the medium as a perfectly homogeneous, where density and speed of sound are constant [60].

$$\nabla^2 p(\vec{r}, t) - \frac{1}{c^2} \frac{\partial^2 p(\vec{r}, t)}{\partial^2 t} = 0 \quad (3)$$

In practice, waves propagate through layers of different tissues which then propagate at different speeds of sound, but this effect can be minimized by selecting an average speed of sound [61].

### 2.1.1.3 Tissue interaction

Tissue interaction includes specular reflection and diffusion. Specular reflection only occurs if the wave interacts with a surface larger than the wavelength  $\lambda = c/f$ , where  $f$  is the wave oscillation frequency. Reflection of an ultrasound wave occurs at interfaces with different acoustic impedance  $Z = \rho c$ . Acoustic impedance is the analog to the electrical impedance or electrical resistance. The proportion of the wave energy transmitted and reflected are governed by the following equation:

$$R = \left( \frac{Z_2 - Z_1}{Z_2 + Z_1} \right)^2 \text{ and } T = 1 - R \quad (4)$$

Where  $R$  and  $T$  are the reflection and transmission coefficients of a wave propagating in a medium with impedance  $Z_1$  and meets another medium with impedance  $Z_2$ .

Most biological tissues interact with waves through diffusion, since the tissues are mostly composed of water, where impedance contrast is low and most of the wave's energy is transmitted. Diffusion occurs when the ultrasound wave interacts with structures that are smaller than the wavelength. In fact, small inhomogeneities in acoustic impedance are preponderant in biological tissue. These inhomogeneities act as punctual sources that reemit the incoming wave in the form of spherical acoustic waves.

When the sources are punctual (small in space) and the signal is very short in time, we can solve the wave propagation equation using the spatiotemporal Green's function  $g(\vec{r}, t)$ , where  $\delta$  is the Dirac delta function and  $\vec{r}_0$  the position of the source.

$$g(\vec{r}, t) = \frac{\delta\left(t - \frac{|\vec{r} - \vec{r}_0|}{c}\right)}{4\pi|\vec{r} - \vec{r}_0|} \quad (5)$$

The Green's function describes the propagation of the spherical wave that is reemitted by a punctual source in the medium. To solve for the pressure field, the Green's function is useful since it is the inverse of the operator  $\left(\nabla^2 - \frac{1}{c^2} \frac{\partial^2}{\partial t^2}\right)$  acting on the variable we are trying to solve, in our case the pressure field  $p(\vec{r}, t)$  in equation (6).

The requirement of punctual sources is met in the case in ultrasound imaging, since a transducer sends a short pulse in a complex medium of scatterers described as a source field  $s(\vec{r}_1, t)$ , where  $\vec{r}_1$  is the position of the field in the medium. The transducer records then a signal corresponding to the pressure field  $p(\vec{r}_2, t)$  where  $\vec{r}_2$  is the position along the transducer. The pressure field  $p(\vec{r}_2, t)$  is obtained using spatial and temporal convolution products and is given by the equation below [62]–[66].

$$p(\vec{r}_2, t) = em(t) \otimes^t s(\vec{r}_1) \otimes^{\vec{r}} h_e(\vec{r}_1, \vec{r}_2, t) \otimes^{\vec{r}} h_r(\vec{r}_1, \vec{r}_2, t) = s(\vec{r}_1, t) \otimes h(\vec{r}_1, t) \quad (7)$$

$em(t)$  describes the emitted vibration of the transducer and the electromechanical coupling of the elements,  $s(\vec{r}_1)$  the source field, which is considered constant in time, and  $h_e(\vec{r}_1, \vec{r}_2, t)$  and  $h_r(\vec{r}_1, \vec{r}_2, t)$  are the spatial impulse responses of the apertures in emission and reception respectively.

#### 2.1.1.4 Ultrasound signal representation

We saw earlier that RF signals are “beamformed” (reconstructed) to display an ultrasound image. The following section shows an intermediate framework that allows for a subsampling of at least a factor of 2 of RF data, without any loss of information. It can even be used for estimating blood velocity in Doppler imaging [67].

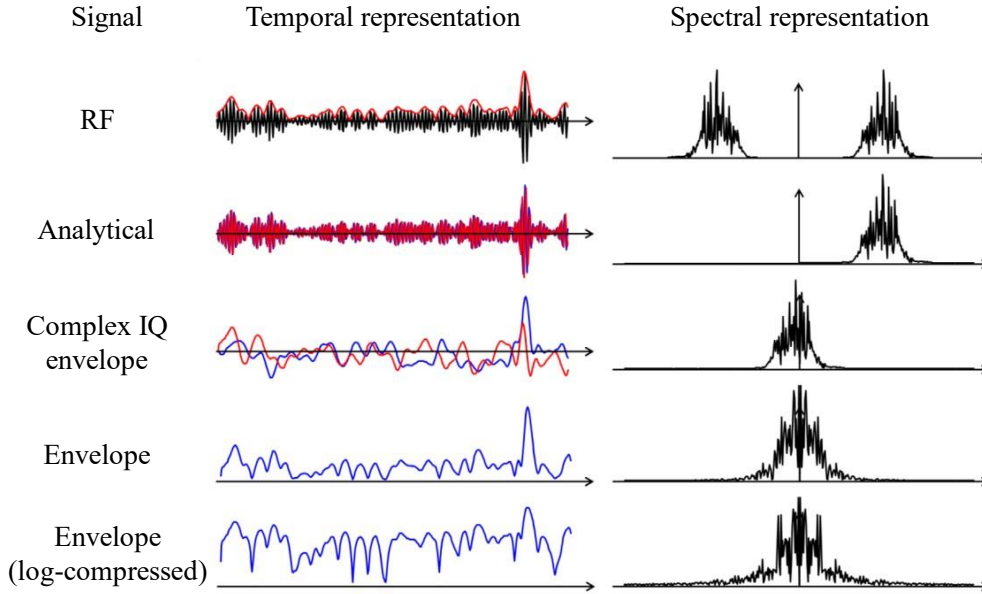


Figure 4: Ultrasound raw signal processing in temporal and frequency domains. Extracted from [67]

The RF signal is the raw output from the ultrasound scanner. Since the RF signal is symmetrical in the frequency domain, the analytical signal  $RF_{an}$  is obtained using the Hilbert transform, which consists of removing negative values. The analytical signal demodulation yields the complex envelope, commonly referred to as IQ signals for “in-phase quadrature”. The demodulation in question is conducted as follows, based on the signal central frequency  $f_c$ .

$$IQ(t) = RF_{an}(t)e^{-j2\pi f_c t} \quad (8)$$

The signal envelope is used for display by taking the absolute value of the analytical signal or the complex envelope. To mitigate the large dynamic range of RF signals, a log compression is usually performed as the last step before display.

### 2.1.1.5 Focused ultrasound imaging

Focused ultrasound is commonly used in hospital settings. To form an image, a focused wavefront is emitted along a line along the z axis using a sub-aperture (see Figure 5), then signal is acquired, reconstructed, and sequentially added together to form a 2D image. The sub-aperture moves from left to right as the medium is scanned.

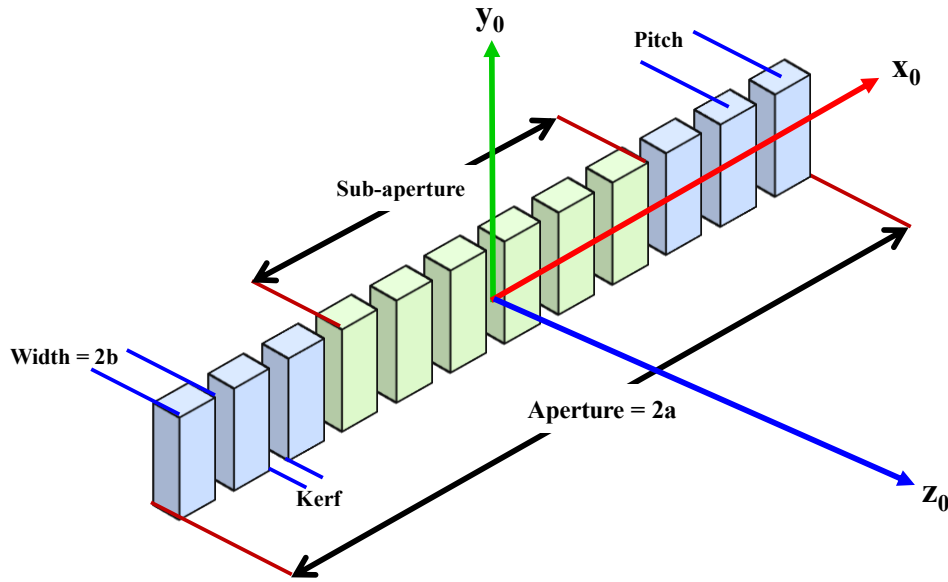


Figure 5: Dimensions and distances in a linear array.

Lateral resolution is limited by the size of the spatial impulse responses in emission and reception. We will consider a linear array for this development. The aperture of a linear array is composed of  $N$  rectangular functions the size of each element.

In focused ultrasound, if we consider a full aperture without any apodization (weighted excitation amplitude for the different elements), this function can be written as



$$p_0(\vec{r}_2, \omega) = \Pi_{2a}(x_0) [\Pi_{2b}(x_0) * III_p(x_0)] \quad (9)$$

Where the rectangle function  $\Pi_{2a}(x_0)$  represents the aperture of the array,  $\Pi_{2b}(x_0)$  represents a rectangular element of width  $2b$ , and  $III_p(x_0)$  is the Dirac comb representing the spatial position of the elements. The inter-element distance is known as the pitch. We can obtain the amplitude of the pressure field at the focal plane by taking the Fourier transform of (10).

$$p(\vec{r}_2, \omega) \approx \text{sinc}\left(\frac{2b}{\lambda} \sin\theta\right) \left[ \text{sinc}\left(\frac{2a}{\lambda} (\sin\theta - \sin\theta_{steer})\right) * III_{1/p}\left(\frac{1}{\lambda} ((\sin\theta - \sin\theta_{steer}))\right) \right] \quad (11)$$

$\theta$  is the angle from the propagation axis and the vector position  $\vec{r}$ , and  $\theta_{steer}$  is the angle of the focused beam. Lateral resolution is deduced from the second term of the equation, which accounts for the principal lobe width  $\theta_{width}$ .

$$\text{sinc}\left(\frac{2a}{\lambda} (\sin\theta_{width})\right) = 0 \quad (12)$$

$$\theta_{width} = \sin^{-1}\left(\frac{\lambda}{2a}\right) = \sin^{-1}\left(\frac{c}{2af}\right) \quad (13)$$

Therefore, the larger the aperture ( $2a$ ) and transmit frequency  $f$ , the better lateral resolution is.

#### 2.1.1.5.1 Axial resolution ( $z$ )

Axial resolution is mostly governed by the temporal characteristics of the emitted ultrasound pulse. Minimum resolvable detail stated by Rayleigh consists of the ability to separate two sources if they are further than the full width at half maximum (FWHM) of the intensity repartition function. As far as the pulse is concerned, this consists of half the length of the pulse, where  $n$  is the number of half cycles.

$$Res_z \sim c \frac{T}{2} = n\lambda = n \frac{c}{f} \quad (14)$$

Increasing frequency or reducing the number of cycles improves the axial resolution, to the detriment of transmitted energy, which reduces contrast.

#### 2.1.1.5.2 Elevation resolution ( $y$ )

The resolution in the elevation direction corresponds to the thickness of the beam in the  $y$  axis. Linear arrays are usually equipped with an acoustic lens that physically focuses the beam in  $y$ . It is usually the largest resolution in 2D imaging and can be found in the manufacturer's transducer specifications.

#### 2.1.1.5.3 Framerate

Framerate is the number of images that can be acquired per second. In focused ultrasound, the maximal framerate  $F_r$  depends on the number of transmits  $N$  that must be made to form a single image and the axial distance of the maximal imaging depth  $z_{max}$  since the imaged medium in each acquisition is a thin strip along  $z$ .

$$F_r = \frac{c}{2Nz_{max}} \quad (15)$$

Typically, 64 to 128 transmits are required to form an image. This limits the framerate to the order of about 100 frames per second (FPS).

### 2.1.1.1 Planewave imaging

Planewave was introduced since the 80s in [68], [69] but reached the “ultrafast” 10000 frames per second in the late 90s in [70]. Thanks to the development of parallel processing hardware with transfer rates in the order of the gigabyte per second, ultrafast imaging bloomed and opened the way to the study of rapid phenomena [71], [72], 3D ultrafast imaging [73] and 4D functional imaging [48], [74].

A planewave is generated when all elements of the probe activate simultaneously, or with a linear delay law (Figure 3) to produce an angled planewave with angle  $\alpha$  (or  $\alpha_x$  and  $\alpha_y$  in matrix array probes). This allows to insonify the whole medium with one acquisition and an increased framerate.

To form an image as we know it, we must solve for the source field  $s(\vec{r}_1, t)$  from the pressure field  $p(\vec{r}_2, t)$  that we measure. Using a conventional linear array, the coordinate system simplifies to  $\vec{r}_1 = (z, x)$  and  $\vec{r}_2 = x_0$  and using a matrix array, the coordinate system is depicted as  $\vec{r}_1 = (z, x, y)$  and  $\vec{r}_2 = (x_0, y_0)$ .

Most approaches today synthetically focus the signal back in space by considering the backscattered pressure field as a decomposition in spherical waves emitted by punctual sources. We will see how we use the Delay and Sum (DAS) algorithm to accomplish that.

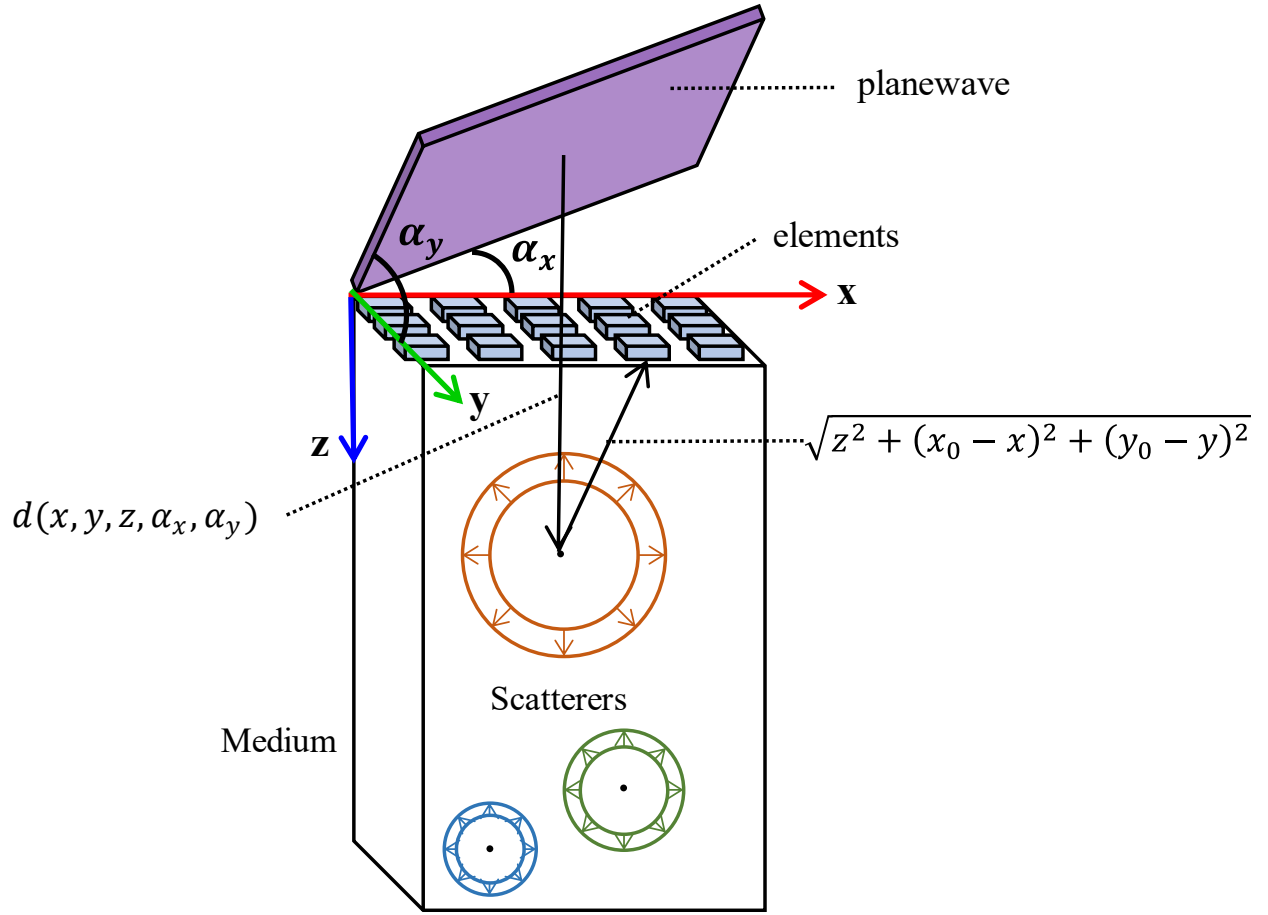


Figure 6: 3D Planewave imaging.

The DAS algorithm is based on the fact that the propagation time of a spherical wave from the source (Figure 6) to the transducer forms a parabolic delay law. The delay  $\tau(x_0, z, x, y)$  is the sum of  $\tau_e$  and  $\tau_r$ , which respectively correspond to the delay from the virtual planewave to the point, and back from the point to the transducer [75], [76].

$$\tau(x_0, z, x, y) = \tau_e + \tau_r = \frac{d(x, y, z, \alpha_x, \alpha_y)}{c} + \frac{\sqrt{z^2 + (x_0 - x)^2 + (y_0 - y)^2}}{c} \quad (16)$$

The image formation  $Im(z, x, y)$  consists of a coherent sum (**Error! Reference source not found.**) of all contributions in the time domain from the source in the medium along the corresponding parabolic delay for the elements  $D$  in  $\vec{r}_2$ , for each of the transmits.

$$Im(x, y, z) = \int_{Dy} \int_{Dx} p(\tau(x_0, y_0, x, y, z), x_0, y_0) dx_0 dy_0 \quad (17)$$

Image formation can also be seen as a focalization in reception, i.e., a retro focusing of the pressure field  $s(x, y, z)$  back in  $(x, y, z)$  thanks to the point spread function (PSF).

$$Im(x, y, z) = s(x, y, z) \otimes^{\vec{r}} PSF \quad (18)$$

The PSF gathers all the effects of spatial and temporal impulse responses of the imaging system. In theory, the PSF could be obtained by imaging a single punctual source with the imaging system. The PSF quantifies the blurring or smoothing effect on any acquired image. Hence, it is an intrinsic metric to assess the ability of an imaging system to distinguish between two close sources. In other words, PSF size (in  $x$ ,  $y$ ,  $z$ , and its volume) offers a downstream measure of spatial resolution of the system.

#### 2.1.1.1.1 Lateral resolution

Lateral resolution is the dimension of the PSF in the  $x$  dimension. In a matrix array, if the disposition and shape of the elements are symmetrical and if transmit angles are also symmetrical, this resolution should also be the same in the  $y$  dimension. The limiting factor for lateral resolution is the beam width. The pressure field  $p_z(x)$  of a focused beam at depth  $z$  is a function of the aperture's width  $2a$ :

$$p_z(x) \sim \text{sinc}\left(\frac{2\pi xa}{\lambda z}\right) \quad (19)$$

Therefore, the beam width is

$$Res_x = \frac{\lambda z}{2a} = \lambda F_{number} \quad (20)$$

The  $F_{number} \left(\frac{z}{2a}\right)$  quantifies the number of active elements in receive, since only the elements that contribute to the signal must be taken. Usually, the  $F_{number}$  values range from 1 to 2, depending

on the directivity of the array and should ideally be kept constant. Therefore, lateral resolution is in the order of the wavelength  $\lambda$ .

#### 2.1.1.1.2 *Image quality and number of angles*

The increased framerate in ultrafast imaging comes at a price of reduced SNR and contrast. However, it is theoretically possible to achieve the same image quality using a number  $n$  of angled transmits calculated using the following equation, where  $L$  is the total length of the array.

$$n = \frac{L}{\lambda F} \quad (21)$$

For example, with an F number of 1, length of array of 10 mm, and wavelength of 100  $\mu\text{m}$ , number of angles is equal to 100. However, in practice, around 10 angles is usually enough depending on the application [75].

#### 2.1.1.1.3 *2D vs 3D ultrafast resolution*

Differences between 2D and 3D ultrafast imaging come mostly from manufacturing/wiring limitations and acquisition parameters, which affect contrast, SNR, resolution, maximal framerate and maximal penetration depth. For deep tissue imaging, penetration depth with low frequency transducers is prioritized, but in this section, we will focus on resolution with relatively high-frequency transducers for relatively shallow imaging (in the order of 1 cm). We'll compare a typical 128-element linear array with a center frequency of 15 MHz [77], [78] with a custom-made 32x32 matrix array (1024 elements) with a center frequency of 15 MHz [79]. Parameters are listed in Table 2.

Table 2: Comparison of a typical 128-element linear array and a custom 32x32 matrix array

Parameters	Linear array	Matrix array
Elements dispositions	128x1	32x32
Frequency (MHz)	15	15
Wavelength <sup>‡</sup>	103	103
Pitch ( $\mu\text{m}$ )	110	300
Element size ( $\mu\text{m}$ )	80x1500	275x275
Element surface ( $\text{mm}^2$ )	0.12	0.0756
Number of angles	15	3
Axial resolution ( $\mu\text{m}$ )	110	175
Lateral resolution ( $\mu\text{m}$ )	110	220
Elevation resolution ( $\mu\text{m}$ )	400	280
PSF volume <sup>§</sup> ( $\text{mm}^3$ )	0.00253	0.00564
Inverse PSF volume ( $\text{mm}^{-3}$ )	395	177

Because of the elements disposition, the linear array is limited to 2D imaging. This means that no information in the elevation direction is retrieved. This means that it can be more difficult to separate the distinct vessels if their projection in the imaging plane appears as if they are merged. However, since the element size is not limited in elevation, the linear array's elements are typically almost an order of magnitude larger than in the matrix array in the elevation plane. This results in more surface area or more piezoelectric material that can transfer energy to the medium. The more energy is transmitted, the greater the image quality. Moreover, in a linear array, there is focusing in elevation that concentrates the energy at the focal point using an acoustic lens. As for transmit angles, even though the number of transmit angles can be high in a matrix array, it is usually kept low because it would generate a substantial amount of data. Moreover, to achieve the same image quality as in 2D imaging using a matrix array, the transmit angles (in x and y) must span the same proportion in terms of surface as the unidimensional equivalent of a linear array: for example, 7 angles using a linear array would translate to 49 angles using a matrix array. In terms of spatial

---

<sup>‡</sup> Calculated using wave propagation velocity  $c = 1540 \text{ m/s}$

<sup>§</sup> Considering the PSF volume ( $V$ ) as an ellipsoid with semi-axes ( $a, b, c$ ) equal to half of the resolutions.

resolution, we can calculate the PSF volume ( $V$ ) by modeling an ellipsoid with semi-axes as half of the resolution in each dimension,

$$V = \frac{4}{3}\pi abc \quad (22)$$

where  $a, b, c$  are the semi-axes of the ellipsoid. The PSF volume is a metric that quantifies the resolution of the system. If we take the inverse of the PSF volume, we obtain a metric that operates in conjunction with frequency, since the higher the frequency, smaller the PSF and higher the inverse PSF volume. However, PSF volume also accounts for acquisition parameters such as probe elements size and disposition and pulse characteristics. We can see that with these specific sets of parameters, the 2D array offers a better power of separation shown by the lower PSF volume. Nonetheless, the matrix array is not far behind and offers the possibility to separate vasculature in all spatial dimensions. This will be crucial for the mapping of vasculature with a degree of confidence that is not hindered by the unknown information in the elevation dimension.

#### 2.1.1.1.4 Resolution in ULM

Resolution in ULM can be derived from the uncertainty of the MB position extracted from the localization process. Even though MB localization in this work is performed on the beamformed image, we can use the derivation of Desailly et al. [80] since the approach performed on 1) the beamformed image and 2) on the radio-frequency (RF) signal are equivalent in a homogeneous medium. The later approach exploits RF signal by fitting a hyperboloid with the time-of-flight equation (23). The error of the MB position can be derived by first determining the error in the arrival time  $\sigma_\tau$ , then computing the spatial errors ( $\sigma_{\hat{x}_0}, \sigma_{\hat{y}_0}, \sigma_{\hat{z}_0}$ ) through the hyperboloid fitting.

Using reference and delayed signals, we can compute the arrival time error (also known as “jitter magnitude”) following Walker and Trahey’s [81] application of the Cramer-Rao formula. Jitter is the difference in time estimate caused mostly by electronic noise and signal decorrelation due to physical processes. The estimate itself is obtained using a cross correlation of reference signal (pulse) and delayed signal (from the MB).

The Cramer-Rao lower bound formula estimates the standard deviation of jitter errors:



$$\sigma_\tau = \sigma(\tau_0 - \hat{\tau}_0) \geq \sqrt{\frac{3}{2f_0^3 \pi^2 T (B^3 + 12B)} \left( \frac{1}{\rho^2} \left( 1 + \frac{1}{SNR^2} \right)^2 - 1 \right)} \quad (24)$$

where  $\hat{\tau}_0$  is the measured arrival time and  $\tau_0$  the true arrival time,  $f_0$  is the pulse center frequency,  $T$  is the time of the window used for the time delay estimation,  $B$  is the fractional bandwidth of the pulse,  $\rho$  is the normalized correlation between reference and delayed signal, and  $SNR$  is the signal-to-noise ratio of the received signal.

Now for the second step, we will obtain the propagated jitter error using the hyperboloid fitting through equation 25. The fitting involves a non-linear regression model where sum of the squared residuals (of jitter error through all probe array elements) must be minimized. This model is converted to the spatial equivalent using the time-of-flight equation (equation 26). Then a covariance matrix of the 3 variables in the regression model ( $x, y, z$ ) is computed. The model was simplified to obtain a simple expression by assuming that the MBs were far from the probe elements. Finally, the standard deviations of the MB localization errors can easily be obtained from the covariance matrix's diagonal:

$$\sigma_{\hat{x}_0} \approx 2\sqrt{3} \frac{c \sigma_\tau z_0}{L_x \sqrt{n}} \quad (27)$$

$$\sigma_{\hat{y}_0} \approx 2\sqrt{3} \frac{c \sigma_\tau z_0}{L_y \sqrt{n}} \quad (28)$$

$$\sigma_{\hat{z}_0} \approx \frac{c \sigma_\tau}{2\sqrt{n}} \quad (29)$$

where  $L_x$  and  $L_y$  are the array's aperture in each dimension,  $c$  is the speed of sound,  $n$  is the number of probe elements, and  $z_0$  is the shortest distance between the MB and the array.

We will compute the lower bound on localization error for the two arrays described earlier and a commonly used matrix array that runs at a lower transmit frequency (7.5 MHz) [82]. We will use the following parameters:

Table 3: Acquisition parameters of a typical 128-element linear array, a custom 32x32 matrix array and a typical 32x32 matrix array

Parameters	Linear array	Matrix array	Matrix array
Number of elements $n$	128x1	32x32	32x32
Transmit frequency $f_0$ (MHz)	<b>15</b>	<b>15</b>	<b>7.5</b>
Aperture in x $L_x$ (mm)	9	12	12
Aperture in y $L_y$ (mm)	1.6	14	14
Bandwidth $B$	50%	50%	50%
Sampling rate $f_s$ (MHz)	240	240	240
Time window size $T$	1/ $f_s$	1/ $f_s$	1/ $f_s$
SNR (dB)	<b>15</b>	<b>10</b>	<b>10</b>
Correlation coefficient $\rho$	0.98	0.98	0.98
$\sigma_z$ ( $\mu\text{m}$ )	<b>1.2</b>	<b>1.4</b>	<b>4.0</b>
$\sigma_x$ ( $\mu\text{m}$ )	<b>0.9</b>	<b>0.8</b>	<b>4.8</b>
$\sigma_y$ ( $\mu\text{m}$ )	NA**	<b>0.7</b>	<b>4.1</b>

As we can see from the lower bounds of the standard deviation on MB position  $\sigma_z$ ,  $\sigma_z$ ,  $\sigma_z$ , the localization error is relatively low compared to the wavelength for single MB localization and for these sets of parameters. However, the lower bound is more sensitive to some parameters. If we vary the SNR for instance, we obtain a sudden rise in localization error at low enough SNR (Figure 7).

---

\*\* Not applicable. Echoes are not reconstructed in this dimension.

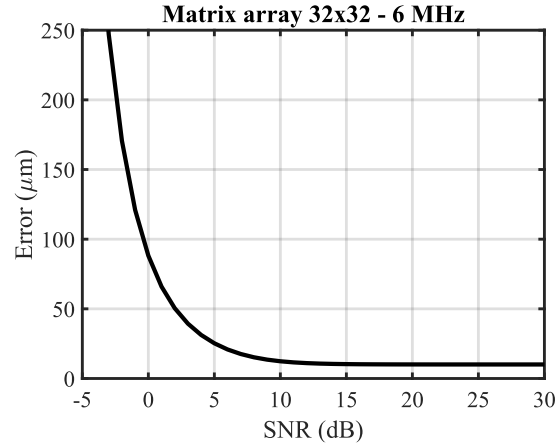


Figure 7: Norm of the lower bound on localization error at different values of SNR for a 32x32 6 MHz matrix array probe.

If we vary the transmit frequency, we obtain a predictable increase in localization error with lower transmit frequencies (Figure 8).

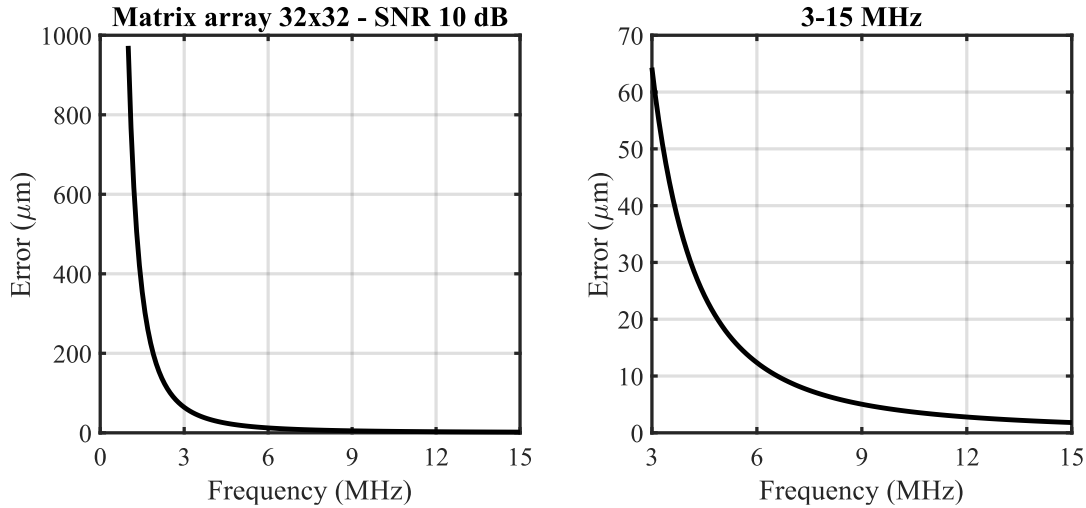


Figure 8: Norm of the lower bound on localization error at different transmit frequencies for a 32x32 matrix array probe. SNR = 10 dB.

One must note that this model is a very simplistic one. As transmit frequency changes, the SNR also should vary, as well as other parameters, such as the correlation coefficient between reference and delayed signals. However, with these results, one should prioritize an SNR that is as high as possible with the specific constraints of an imaging application to avoid a surge in localization error.

## 2.2 Ultrasound localization microscopy

### 2.2.1 Major events in ULM

This section describes selected events from the first use of miniature bubbles as a contrast agent to the current ULM practice.

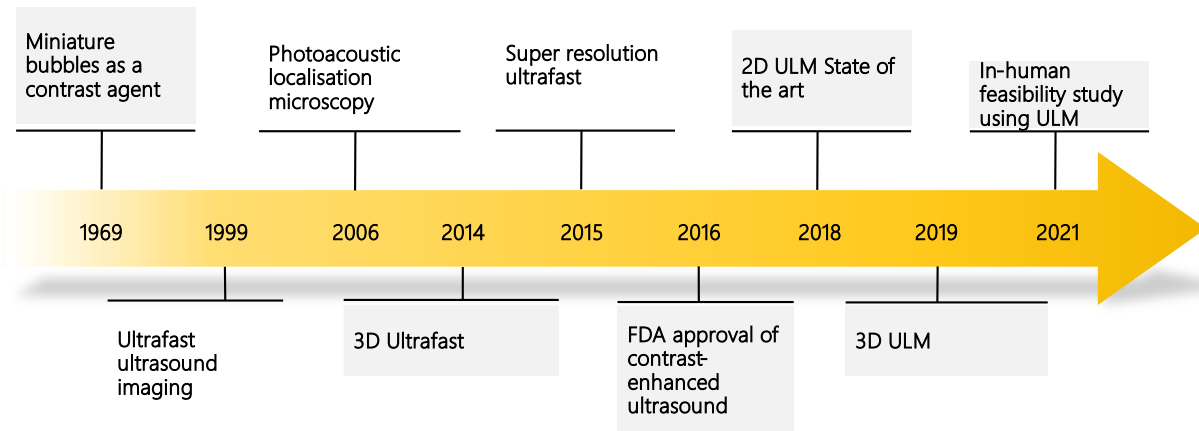


Figure 9: Timeline of major events in ULM

In 1969, Gramiak et al. [83] observed that in the routinely used dye of indocyanine green in cardiac imaging, there was a presence of foam described as miniature bubbles. The echoes from such bubbles were more intense than any other contrast agent used in that study. This discovery will lead to a variety of microbubble designs and functionalization described in section 2.2.2.2. In 1999, Sandrin et al. [70] achieved an acquisition rate of approximately 10000 frames per second that open the way to the study of rapid phenomena. They used a programmable echograph to insonify the whole medium with a single planewave and acquire and save data in 64 channels in parallel. At that time, channel memory was limited to 128 Kbytes which limited a maximum of stored frames of 43.

Thanks to the exponentially increasing development of integrated electronics [84], the development of highly capable graphical processing units (GPU) and large storage solutions was possible. This development was essential for the expansion of ultrafast imaging since acquisition and beamforming needed to be performed in parallel and with a large amount of data, in the order of a “Netflix” movie per second (Gbyte per second). In 2014, Provost et al. [73] demonstrated the

potential of *in-vivo* 3D ultrafast imaging for clinical applications in the heart using a 32x32 matrix array probe with 1024 independent channels.

As for ULM per say, microvasculature mapping below the diffraction limit was demonstrated in 2D by Errico et al. in 2015 [3] using perfluorocarbon-based microbubbles localization and tracking. This technique was inspired by an optical equivalent – photoacoustic localization microscopy (PALM) published in 2006 by Betzig et al. in which target proteins could be separated with a resolution lower than a tenth of the wavelength [85]. In 2016, the use of contrast-enhanced ultrasound for clinical use was approved by the FDA in the United States. It was approved for imaging liver tumors in adults and children, but it opened the way for subsequent studies in other organs. The first review of ULM was published in 2018 by Couture et al. [5], and the second in 2020 by Christensen-Jeffries et al. [86] (Not depicted on timeline). A study published in 2019 by Heiles et al. [87] featured ULM applied in 3D *in-vitro* on a simple phantom comprised of a channel (400  $\mu\text{m}$ ) separating into 2 smaller channels (200  $\mu\text{m}$ ). A study on a more complex phantom or in an *in-vivo* model is yet to come.

More recently in 2021, an in-human ULM feasibility study using a linear array was performed on tissues including liver, kidney, pancreas, and breast tumor by Huang et al. [22]. Patients were asked to hold breath for the duration of the acquisition of only 10 seconds, and vessels that were inseparable using Doppler could be distinguished using the ULM framework thanks to an enhanced spatial resolution. This work is an exciting proof of concept for future clinical application of ULM.

The following figure shows major groups currently working on ULM and will continue to grow in the upcoming years (Figure 10).

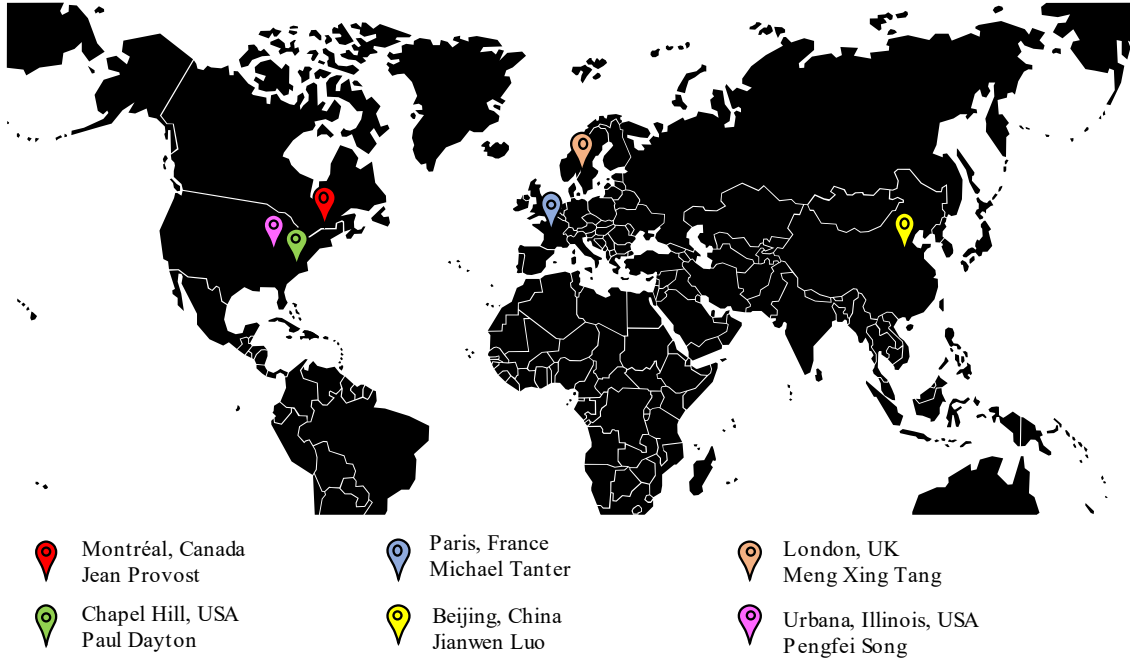


Figure 10: Selected research groups in ULM on a world map <sup>††</sup>.

## 2.2.2 Ultrasound localization microscopy characteristics

### 2.2.2.1 Requirements

Localization imaging can achieve a resolution far below the wavelength. To carry off this imaging prowess, a few conditions must be met [5], [85].

1. *Labelling*: Labels that are much smaller than the wavelength, which can act as isolated sources from surroundings, and are specific to the imaging region of interest.
2. *Localization*: The spatial position of these labels must be obtained with an accuracy better than the diffraction limit.
3. *High framerate acquisition*: Even the most minute displacements have a large impact in the scale that we are operating. Therefore, a high framerate is required to correct for tissue motion.

---

<sup>††</sup> Only one name per group is depicted for simplicity purposes.

4. *Isolated sources in a spatiotemporal referential*: Localization requires labels to be far apart. Any interaction between sources will cause an error in the sources position. Again, at a scale well beyond the diffraction limit, the smallest error can become significant compared to the targeted resolution.

#### 2.2.2.2 Microbubbles

Blood is a relatively poor scatterer. Therefore, ultrasound contrast agents are usually used to increase the acoustic scattering of the blood, relative to the surrounding tissue, which creates improves contrast between vessels and interstitial tissue [88], [89]. In ULM, even though vascular contrast can be ultimately achieved, we are interested in using MBs as isolated sources. The currently FDA-approved MBs exhibit characteristics that make them perfect for their applications in ULM, namely being:

1. Safe for intravenous injection
2. Stable
3. Echogenic

The safety related to an intravenous injection requires the MBs to be small enough to prevent any flow occlusion in capillaries, which means that they must remain below 10  $\mu\text{m}$ . Moreover, they need to be biocompatible and easily metabolized and excreted from the body. Current MBs are made of a lipidic, polymeric or a combination of both. Typical polymers consist of biological proteins such as the human serum albumin or synthetic compounds such as methyl-polyethylene glycol (mPEG) [90]. Their role is to help stabilize the gas core from the immune system, coalescence (merging) and rapid dissolution. These shells counteract the van der Waals attraction by adding repulsive forces, such as electrostatic, hydration, protrusion and polymeric-static.

Table 4 shows the characteristics of the three most used FDA-approved MBs in the market.

Table 4: FDA-approved and commercially available MBs. Adapted from [90].

MB	Gas core	Shell type	Diameter	Concentration
Optison™	C <sub>3</sub> F <sub>8</sub>	Protein	3.0-4.5 $\mu\text{m}$ (max. 32 $\mu\text{m}$ )	5.0-8.0 x 10 <sup>8</sup> /mL

---

			95% < 10 $\mu\text{m}$	
			1.1-3.3 $\mu\text{m}$	
Definity®	C <sub>3</sub> F <sub>8</sub>	Phospholipid	(max. 20 $\mu\text{m}$ )	1.2 x 10 <sup>10</sup> /mL
			98% < 10 $\mu\text{m}$	
			1.5-2.5 $\mu\text{m}$	
Sonovue®	SF <sub>6</sub>	Phospholipid	(max. 20 $\mu\text{m}$ )	1.5-5.6 x 10 <sup>8</sup> /mL
			99% < 10 $\mu\text{m}$	

---

Their echogenicity comes mainly from an impedance mismatch (causing high scattering) and resonance. We can quantify scattering using the following equation derived from [91].:

$$\sigma_s = 4 \pi R^2 (kR)^4 \left[ \left( \frac{K - K_0}{K} \right) + \frac{1}{3} \left( \frac{\rho - \rho_0}{2\rho + \rho_0} \right) \right] \quad (30)$$

where  $R$  is the radius,  $k$  is the acoustic wavenumber ( $k = \frac{2\pi f}{c}$ ),  $f$  is the frequency,  $c$  the speed of sound,  $\rho$  and  $\rho_0$  are the mass densities of the MB and the medium respectively, and  $K$  and  $K_0$  are the compression bulk moduli of the MB and the medium. We can see that the scattering scales with the radius as  $R^6$  and is larger with a low  $K$  (high compressibility), hence the choices of a larger MB that fits into capillaries and a core made of gas ( $\sim 10^9$  more scattering in a gas than in a liquid as glycerin). As for resonance, the linearized resonance frequency for a microbubble for small-scale oscillations is given by:

$$f_0 = \frac{1}{2\pi} \sqrt{\frac{1}{\rho_0 R^2} \left[ 3\kappa P_0 + \frac{2\gamma(3\kappa - 1)}{R} \right]} \quad (31)$$

where  $\gamma$  is the gas/water interfacial tension,  $\kappa$  is the polytropic gas constant and  $P_0$  is the hydrostatic pressure ( $\rho_0 g z$ ).  $\rho_0$  is the medium density,  $g$  is the gravitation acceleration constant, and  $z$  the depth of the MB in the medium. For an unshelled MB, transmit frequencies of 1 MHz and 10 MHz result in a resonant MB diameter of approximately 8  $\mu\text{m}$  and 1.2  $\mu\text{m}$  respectively, with  $\gamma = 0.072$  N/m, which makes them ideal for ultrasound imaging. At frequencies approaching 15 MHz, we are outside of current MBs resonant frequencies (also little harmonics). However, this is not an issue since MBs are still highly echogenic and can be separated using techniques that we will see in section 2.2.2.4.



One should note that MB circulation in the body can be made using a single injection (bolus) or using a continuous injection (infusion) through time using an electronic pump that regulates flow. Both practices are FDA approved and dosage is described in [92] for Definity® MBs. As for the mechanical index, it should be kept below 0.4 according to literature to prevent MB cavitation and capillary leakage and extravasations [93], even though are approved for higher mechanical indexes.

### 2.2.2.3 Acquisition

After injection of a bolus or infusion of MBs, ultrasound acquisition can be undertaken. This involves the insonification of the medium and reception of backscattered echoes. This can be achieved using conventional or ultrafast ultrasound. Conventional ultrasound imaging can already achieve framerates of about 50 frames per second but ultrafast allows to increase this value. Even though a theoretical 20 000 frames/s is possible for shallow tissue [5], current ultrafast sequences are designed for lower framerates to allow for deeper imaging, for 3D imaging, for image compounding to increase image quality, and to allow for channel multiplexing [73], [75]. After reception of the radiofrequency signals, an image is reconstructed using an image-formation algorithm, such as the commonly used delay-and-sum algorithm [94]. A portion of the reconstructed image is shown in Figure 11 as well as the subsequent steps in the ULM framework.

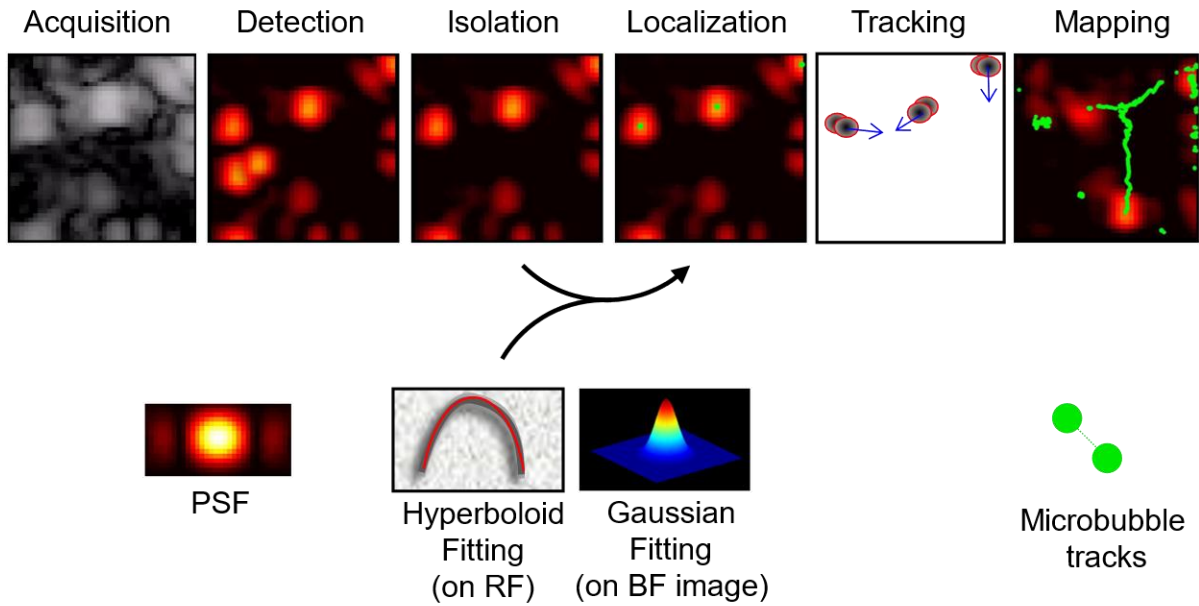


Figure 11: Ultrasound localization microscopy framework. Adapted from [86]

#### 2.2.2.4 Detection

After the acquisition and reconstruction of ultrasound signals, we obtain 2D or 3D images through time that contain information about tissue signature, blood, microbubbles, possibly artifacts, and inevitably noise. All this information is mixed in pixels and voxels present in the data. A popular approach intended for the separation of signal is the Singular Value Decomposition (SVD). We will see how this approach takes a large Matrix  $S$  with a high dimensionality, that is sparse (most elements are 0), and transforms it into a low-rank subspace (smaller dimensionality) where components of the signal are sorted according to their coherence throughout a certain dimension (in our case: time).

We model the general problem as follows: We have a matrix of data  $M$ , which is composed of the added contributions of: 1) A highly coherent agent ( $A_0$ ), 2) A somewhat variable agent ( $B_0$ ), and lastly 3) a random agent ( $C_0$ ) [95].

$$M = A_0 + B_0 + C_0 \quad (32)$$

Specifically, we have a complex signal  $M$  from radio-frequency data that is function of space and time, which contains the contributions of 1) Tissue ( $\mathbf{a}$ ), 2) Moving blood and microbubbles ( $\mathbf{b}$ ), and 3) Noise ( $\mathbf{c}$ ) [3], [5], [96]. This signal is either 3D (2D + t) or 4D (3D + t), where the dimension of data  $M$  is  $n_x, n_y, n_z, n_t$ , which are respectively the number of pixels in x, y, and z, and the number of frames through time.

$$M = m(x, y, z, t) = \mathbf{a}(x, y, z, t) + \mathbf{b}(x, y, z, t) + \mathbf{c}(x, y, z, t) \quad (33)$$

We will transform the data from matrix  $M$  into a Casorati matrix  $S$  (size  $n \times m$ ), where data is arranged in columns. In our case, columns  $f_i$  in  $S$  are frames, which are either 2D images or 3D volumes at specific time points, reshaped into  $1 \times n$  vectors. In general,  $n = n_x * n_y * n_z$ , which is the number of elements in each frame and  $m = n_t$  is the number of frames in the data.

$$S = \begin{bmatrix} \vdots & \vdots & \vdots & \vdots \\ f_1 & f_2 & f_3 & \dots f_m \\ \vdots & \vdots & \vdots & \vdots \end{bmatrix}_{n \times m} \quad (34)$$

Using this Casorati matrix  $S$ , we will compute its decomposition by SVD:

$$\mathbf{S} = \mathbf{U}\mathbf{\Delta}\mathbf{V}^* \quad (35)$$

Where,  $\mathbf{\Delta}$  is a non-square ( $n \times m$ ) diagonal matrix with coefficients corresponding to singular values  $\lambda_k$  sorted in decreasing value, where the number of singular values is equal to the number of columns of  $\mathbf{S}$ .  $\mathbf{U}$  and  $\mathbf{V}$  are orthonormal matrices that have a rank  $m$ , with respective dimensions ( $n \times n$ ) and ( $m \times m$ ), and  $^*$  represents the conjugate transpose since we are working with complex signals. Columns of  $\mathbf{U}$  and  $\mathbf{V}$  represent respectively the spatial and temporal singular vectors of  $\mathbf{S}$ . Since we sorted data to obtain decreasing singular values, the first singular vectors correspond to higher spatial coherence, in our case: tissue. For example, to obtain a signal without the contribution tissue ( $\mathbf{S}^f$ ), we can use a simple mask  $\mathbf{I}_t$  to remove the contribution of tissue, where  $\mathbf{I}_t$  is a diagonal matrix with first few elements being zero and others being ones.

$$\mathbf{S}^f = \mathbf{U}\mathbf{\Delta}\mathbf{I}_t\mathbf{V}^* \quad (36)$$

We can use the same formalism for noise removal and only keep contribution of flowing MBs ( $\mathbf{S}^{MB}$ ) by using another mask  $\mathbf{I}_n$ , where  $\mathbf{I}_n$  is a diagonal matrix with last few elements being zero and others being ones.

$$\mathbf{S}^{MB} = \mathbf{U}\mathbf{\Delta}\mathbf{I}_t\mathbf{I}_n\mathbf{V}^* \quad (37)$$

The number of zeros in  $\mathbf{I}_t$  and  $\mathbf{I}_n$  depends on the data itself and usually requires manual tuning, however adaptive thresholding was proposed in [96].

In this work, no tissue filtering was needed since no tissue was modelled but would be interesting to add in future work. As we saw earlier, lower bounds on localization error are highly dependent on SNR. Therefore, white gaussian noise was added to RF data to achieve realistic SNR and improve realism.

### 2.2.2.5 Isolation

Once images only contain MB signals, there is a critical step before trying to compute the exact positions of MBs. In ULM, we hypothesize that MBs are isolated sources in a spatiotemporal referential. In the isolation step, we must discard echoes that are closer than a few wavelengths [86]. In Christensen-Jeffries et al. 2015 [7], filtered MB signals were binarized and size of

connected regions was computed. By doing so, regions larger than the expected PSF size were discarded. In this work, IQ volumes were convolved with the PSF of the system to create correlation maps. This hypothesis is generally true since MBs (1-3  $\mu\text{m}$ ) are orders of magnitudes smaller than the wavelength (100-500  $\mu\text{m}$ ). These correlation maps are most intense when there is an overlap between an isolated MB and the PSF and a correlation threshold can be established to reject MBs that are not behaving like single sources.

#### **2.2.2.6 Localization**

Any imaging system is characterized and limited by its PSF. This limit is due to wave interference, investigated by Airy and Rayleigh [2], which is defined as diffraction when this wave interference occurs on an obstacle or opening that is always present in an imaging system. We saw earlier that this effect can be seen as blurring of the observed target and establishes a limit on our ability to separate neighbouring sources in the order of the wavelength of the wave in question. In this step of the framework, we leverage the fact that sources are isolated in a spatiotemporal referential and the known PSF to compute the position of the MBs either in the temporal domain in radiofrequency (RF) data, or in the spatial domain, in reconstructed ultrasound images (IQ). This is achieved through a fitting of either hyperboloid on echoes found of RF data [5], [42], [43], [86] or a gaussian fitting on spatial data [3], [7], [40], [41], [97]. The exact position of the MB is then simply the local maximum on that fitting. The error on the position of the MB is no longer bound to the diffraction limit but rather bound to our precision in estimating the echo delay [4].

#### **2.2.2.7 Display**

Most simple way of displaying MB positions consists of plotting dots on an image or a volume. However, to display a vascular network, we are interested in segmenting, or linking those MB positions to map vessels and their connections to one another. We will see in the next section how we can link MBs to ultimately help us differentiate vessels in which they are flowing in. The most straightforward approach of displaying a vascular network from MB positions consists of generating density maps. To generate a density map, a volume is created with dimensions of the range of the MB positions. Each voxel's intensity represents the number of present MBs in that specific voxel. With this method, there is a compromise between sensitivity, and resolution when choosing a certain voxel size [6]. We saw in section 1.1 the different metrics that can be extracted

from microbubble positions which in term can be leveraged to develop biomarkers. The biomarker's accuracy, specificity, sensitivity, repeatability [98] and even the ease of use of the display related to that biomarker [99] will determine possible challenges in clinical trials [100], hence the importance of MB detection, tracking, and display.

#### **2.2.2.8 Tracking**

In Kirsten 2015 [7], cross correlation was computed between a small region of interest (on IQ data) containing a MB signal in frame  $n$  and the same ROI in frame  $n-1$  within 400 micrometers. A track of two neighboring MBs was set if cross correlation exceeded the empirical threshold of 0.8. In Ackermann and Schmitz 2016 [97], MB tracks were formed using a Markov Chain Monte Carlo algorithm on detected MB position based on prior probability. That probability was computed using the number of detected targets, number of terminated tracks, a false alarm rate, and a birth rate. The principal advantage is that associations between MBs that are associated with a higher probability under the given data are also drawn and tested with a higher probability. This means that a brute force approach testing all possibilities is avoided. This is especially important for large datasets, as in in-vivo applications. Also, the algorithm is applied using a sliding window to limit computational cost. In Solomon et al. 2018 [101], they were constrained to data from intensity images from clinical scanners where only MB responses are displayed. The proposed framework contains various building blocks that are updated after each frame computation. The tracking algorithm is based on an accumulated MB probability from the previous frame. This probability was computed using velocity estimates of the flowing MBs. Super-resolution mapping was performed by minimizing a problem based on the PSF of the system weighted by flow dynamics of MBs mentioned earlier. However, this approach seems to generate additional vessels compared to the reference image, which could be problematic. In the aforementioned tracking algorithms, some useful information is discarded when particles are prematurely rejected based on close proximity or based on a velocity measurement from a narrow time window. Furthermore, a high computational cost is usually associated with most of the algorithms. In Alberti et al. 2018 [102], the localization framework as we know it is bypassed by a model where data is lifted to the phase domain, where signals are separated according to both position and velocity. However, this approach was only tested in simulation, therefore we cannot yet conclude on practical performance.

### 2.2.2.9 Motion correction

Brain imaging usually involves less motion than cardiac imaging or internal organs imaging and is less prone to breathing motion. However, motion correction becomes essential if brain movement caused by the heart pulsatility within the cerebrospinal fluid or flexion of transducer setup are orders of magnitude higher than the desired resolution. Accumulated motion over an acquisition time in the order of seconds and even minutes depending on the desired network filling [6] can cause unacceptable blurring of the image [103].

Work on speckle tracking and transient elastography [70] demonstrated micrometric motion correction from IQ data. This is possible since IQ data is highly sensitive to phase. Phase aberrations do not vary greatly among array elements that are in close proximity and for phase discontinuities, they can easily be detected and removed [81]. This creates a tissue signature that can be leveraged to track tissue motion.

Motion correction in an ULM context was applied in Foiret et al. 2017 [10], where normalized cross correlation was applied to a region of interest where few of MBs were present to limit decorrelation. Frame-to-frame correlation allowed to monitor timing of the cardiac cycle and respiratory cycle. Frames in a respiratory cycle were characterized by a decorrelation of more than 10% and were then discarded. Remaining frames were grouped according of their timing along the cardiac cycle. Rigid motion was correction (translation (x, z) and rotation) was applied to account for motion due to cardiac pulsatility. Using this framework, mapped vessels were more defined than the uncorrected ones. More advanced non-rigid motion correction was implemented in [24], but it was in Hingot et al. [103] where motion correction could be applied on isolated tissue. Using SVD on B-mode images, tissue was isolated by taking only the first 2 singular values as we saw earlier, and cross-correlation was computed between images  $I_1(x, y, z)$  and  $I_1(x + \Delta x, y + \Delta y, z + \Delta z)$  contain movement  $(\Delta x, \Delta y, \Delta z)$ .

$$\frac{f(I_1)f \circ (I_2)^*}{|f(I_1) \circ f(I_2)|} = e^{j\phi(\Delta x, \Delta y, \Delta z)} \quad (38)$$

The inverse Fourier transform of the cross-correlation was computed and yielded a Dirac peak in the spatial dimensions, corresponding to the displacement between images. This is the case since

cross-correlation is maximal when images are perfectly superimposed. MB positions could then be corrected using this displacement.

More recently, ULM was performed on a rat's beating heart by correcting for large myocardial motion and deformation [104]. The imaging setup consisted of a 15.625 MHz linear array firing planewaves at a pulse repetition frequency of 9000 Hz and 3 angles compounding ( $-3^\circ$ ,  $0^\circ$ ,  $3^\circ$ ), yielding 3000 frames per second. Imaging was triggered using signal from an electrocardiogram (ECG) to form groups of images of 400 ms referred to as cine-loops. In total, 800 groups of 1200 images were acquired for a duration of 12 minutes. Instead of using pixels coordinates (Eulerian coordinates), images were reconstructed in coordinates of the tissue (Lagrangian coordinates). As for displacement, it is estimated iteratively by leveraging velocity from Doppler measurements [105]. Lagrangian coordinates are first initialized as follows:

$$\vec{x}_{Lag}^0 = \vec{x}_{Euler} \quad (39)$$

Then, iteratively updated as:

$$\vec{x}_{Lag}^i = \underset{\vec{x}}{\operatorname{argmin}} \left\{ \left\| \vec{x} - \vec{x}_{Euler} + \int_{t_{ref}}^{t_f} \vec{v}_T(\vec{x}_{Lag}^{i-1}, t) dt \right\|^2 \right\} \quad (40)$$

Where  $\vec{x}_{Euler}$  represents the Eulerian coordinates,  $\vec{x}_{Lag}$  the Lagrangian coordinates,  $\vec{x}$  an intermediate set of Lagrangian coordinates,  $\vec{v}_T$  the evaluation of tissue velocity,  $t_{ref}$  the time at peak systole,  $t_f$  the duration of a cine-loop,  $i$  the iteration and  $t$  the time.

In practice, the algorithm was implemented in 6 steps and 3 iterations were sufficient to obtain a stable set of coordinates.

#### 2.2.2.10 Machine learning

Machine learning is leveraged when the rationale behind a process is difficult to compute analytically. This could be applied to any of the previous steps in the ULM framework. Studies have shown that deep learning-based localization for ULM could improve vascular reconstruction

under challenging conditions such as a high MB concentration and short acquisition time [13], [106], [107].

#### **2.2.2.11 The compromise between precision and acquisition time**

In *in-vivo* imaging, we are trying to shed light on a very complex yet unknown vascular network. Practical limitations include desirable features such as free-hand imaging and real-time processing and display. In ULM, we leverage the time domain (long acquisition time) to improve our spatial separation power, but we are bound to a short acquisition time for practical use. Therefore, we aim to maximize the amount of information that we can retrieve in the shortest amount of time. The simplest approach consists of increasing the MB concentration, since in theory, the more MB events are detected, the less time is required to map a certain amount of the vascular network [6]. However, we are limited by one of the ULM requirements, which needs sources to be separate in a spatiotemporal domain [5]. If the MB concentration is too high, MB's PSFs merge and an added localization error is generated. This reduces localization precision, which is depicted by blurring of the mapped vessels on a density map. Therefore, there must be an optimal MB concentration where a maximal portion of the vascular network is mapped, while being true to some extent to the real vascular mapping of the patient.

### **2.3 Flow simulation**

Flow simulations include mesh-based methods, particle-based methods, and hybrid mesh-particle methods [108]. Mesh-based methods (Figure 12 (Left)) consider the macroscopic nature of fluidics, where the fluid and particle phases are merged, as opposed to particle-based methods (Figure 12 (Right)), where the fluid phase is discretized [109]. There is a compromise between spatiotemporal discretization of the simulation, scale of the flow network, and computation requirements.



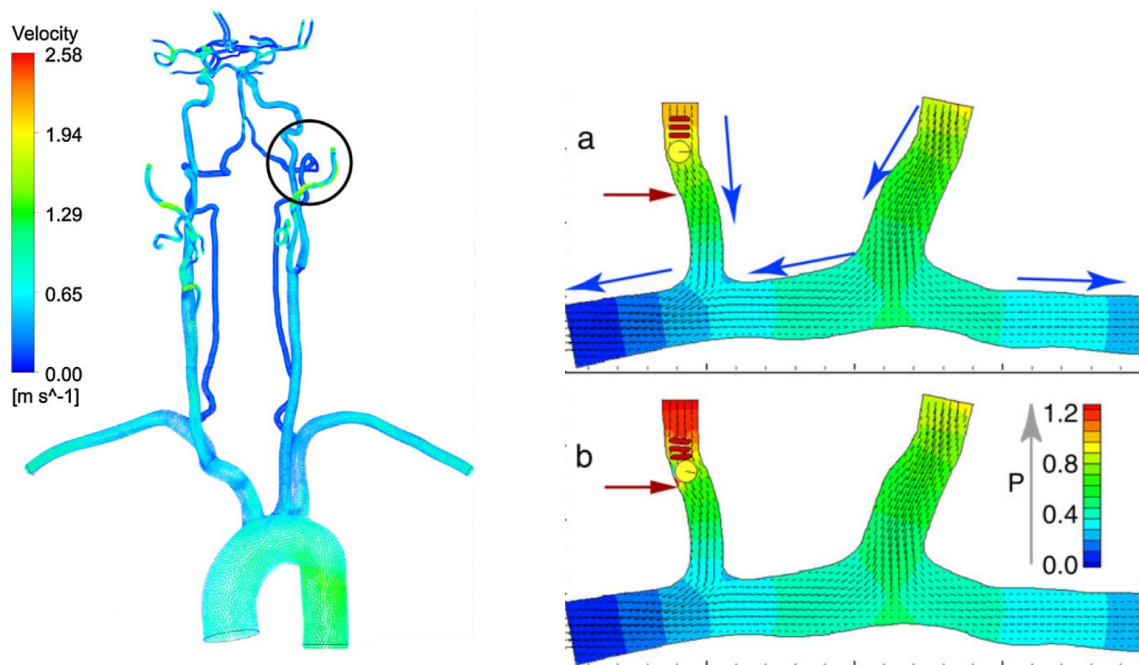


Figure 12: Examples of mesh-based and particle-based flow simulations. (Left) Blood velocity distribution from the aorta to the second branch arteries using a mesh-based simulation. Adapted from [110] . (Right) Adapted from [111]

Since we aim at modelling flow of MBs, particle-based methods are most appropriate, however it would be computationally extensive when scaling to a full organ microvascular network [108]. Therefore, a light-weight graph-based method would allow to simulate a large number of particles (millions) in a large (centimeters) and complex vascular network (high vascular density). Details of the particle flow simulation are provided in sections 0, 4.3.3, and 4.3.4.

## Chapter 3 METHODOLOGY

The project can be subdivided into three sets of tasks:

1. Develop a simulation pipeline where two-photon microscopy (2PM) data is used to generate a virtual flow phantom of reference MB positions that can be used as punctual scatterers in the ultrasound simulation. Then generate ultrasound signals, reconstruct them into time-dependent volumes, and on which we can apply our localization algorithm to generate localized MB positions.
2. Quantify the performance of our imaging framework by measuring localization error, MB count, network filling and by comparing MB mappings to the reference mapping.

### 3.1 Simulation pipeline

The simulation pipeline consists of using two-photon microscopy (2PM) data to generate a virtual flow phantom of reference MB positions that can be used as punctual scatterers in the ultrasound simulation. In the latter, ultrasound signals are generated, reconstructed, and on which our localization algorithm is applied to generate localized MB positions.

#### 3.1.1 Serial 2-photon data processing

The datasets acquired using 2PM were previously used in [112], [113] to study blood oxygenation in mice brain cortex. Data acquisition is described in section 4.3.1. They were chosen since they were also used in a study where the 2PM data was segmented and transformed to a graph model by Rafat Damseh, a former PhD student directed by Professor Frederic Lesage. The graph model is a vectorized version of the vessels in space described by nodes, their radius, 3D position and their connections to one another [32]. The automatic graph modelling process is described in section 4.3.2. This platform allows for the generation of a path for a flowing particle. This path is represented by nodes that are arbitrarily spaced, therefore it requires subsequent steps to achieve a MB path with a discretization dependent on MB velocity and framerate.

### 3.1.2 Microbubble flow simulation

From this graph model of vasculature, we want to generate flowing MBs with known positions in time. From these reference MB positions, a steady-state simulation of MBs can be computed, to be used as scattered positions in the ultrasound simulation. Ultrasound signals are generated, reconstructed, and then MBs from the simulated images are localized with a certain accuracy. This accuracy can be then computed since we have the reference MBs. Nonetheless, the MBs' concentration and their distribution in the vessels have a profound impact on the metrics and performance analysis down the road. Therefore, the MB simulation must be as true as possible to real-life MB behavior. We could leverage results from Hingot et al. 2019 [6], where a study was conducted on a sample of 150 vessels in a rat brain model and where MBs metrics were computed. In that work, a link between vessel diameter and MB velocity was found, as well as a link between vessel diameter and the MB count (the number of MB flowing in a vessel in time). These metrics were essential since we prioritized a MB behavior that would allow to mimic real-life interactions where we could test the limits of the hypothesis requiring separate MBs in a spatiotemporal referential. In simple terms, we needed the MBs to be close to each other in a realistic manner, for example having more and faster flowing MBs in large vessels and very few and slower MBs flowing in smaller vessels.

Before generating a steady state simulation flow, particle trajectories were computed using the graph model source nodes, target nodes and vessel radii. For each trajectory, the shortest path between the source node and a random extremity node was calculated. In Figure 13, general nodes are shown in blue, bifurcation nodes are depicted in green circles, and end nodes are depicted as black circles black. The shortest path from the start node and a random node is depicted in red.

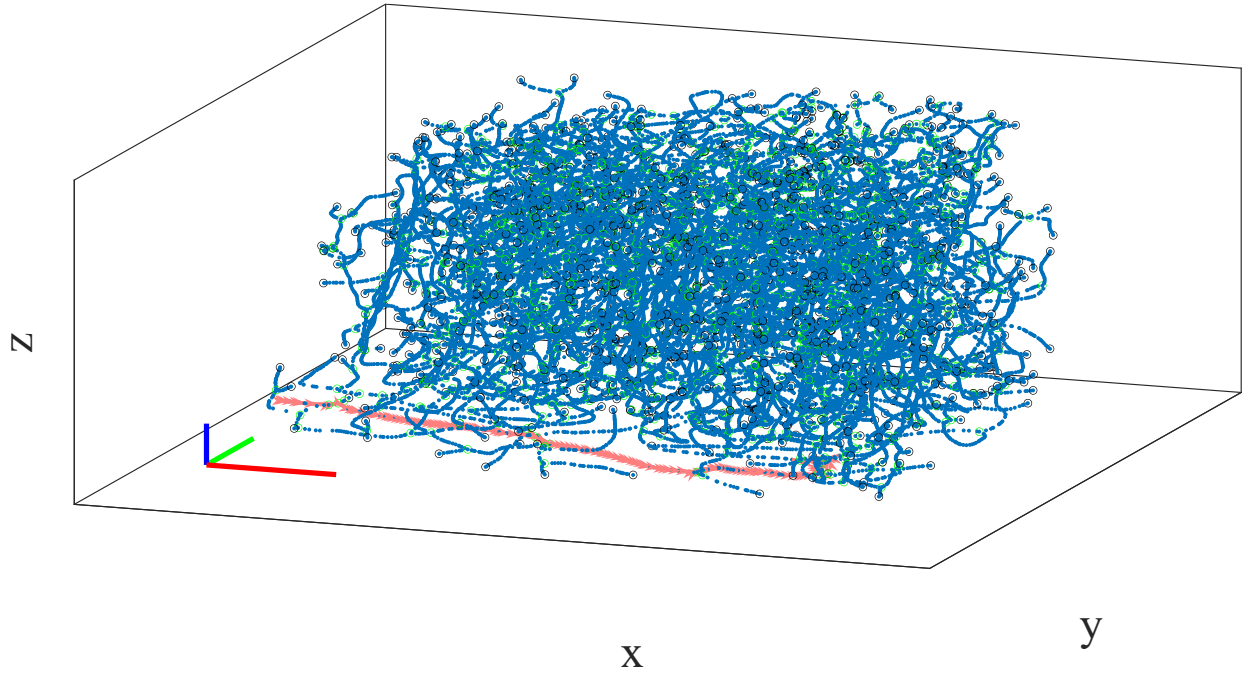


Figure 13: Graph model. General nodes are in blue, bifurcation nodes are depicted in green circles, and end nodes are depicted as black circles. In red is a random trajectory from the start node to a random node. Red, green, and blue scale bars are 100  $\mu\text{m}$  long in each dimension ( $x$ ,  $y$ ,  $z$ ).

A cubic spline fitting is then applied (Figure 14). All node-node distances ( $d_i$ ) are computed, where  $v_{Hingot}$  is the velocity from velocity-diameter relationship of in-vivo data,  $dt$  is the timestamp and  $P$  a given normalized Poiseuille factor.

$$d_i = v_{Hingot_i} * dt * P \quad (41)$$

New centerline node spatial positions ( $X_i, Y_i, Z_i$ ) are then computed using the spline fitting, where  $a_j, b_j, c_j$  and  $d_j$  are the cubic spline coefficients.

$$\begin{aligned} X_i &= a_j \Delta^3 + b_j \Delta^2 + c_j \Delta + d_j \\ Y_i &= a_{j+1} \Delta^3 + b_{j+1} \Delta^2 + c_{j+1} \Delta + d_{j+1} \\ Z_i &= a_{j+2} \Delta^3 + b_{j+2} \Delta^2 + c_{j+2} \Delta + d_{j+2} \end{aligned} \quad (42)$$

$\Delta$  is defined as

$$\Delta = \frac{r}{R} * \sqrt{R} = \frac{r}{\sqrt{R}} \quad (43)$$

where  $r$  is the new node distance from closest original node and  $R$  is the original inter-node distance. Using parallel vectors of the centerline trajectories, two orthogonal perpendicular vectors were calculated. Using a normalized linear combination of the latter, perpendicular vectors with random orientation were created. The laminar trajectory (Figure 14) was generated using the centerline trajectory and the perpendicular vectors normalized with the radius of the neighboring vessels.

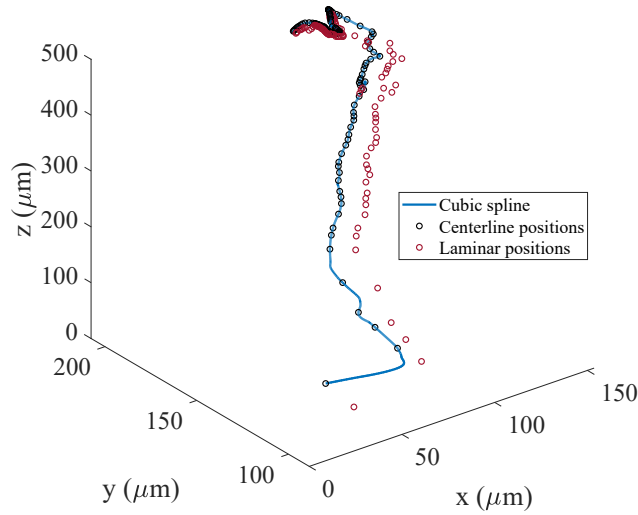


Figure 14: Trajectory calculation. In blue is the cubic spline curve, in black are the centerline MB positions and in red are the laminar MB positions calculated from the centerline positions and perpendicular vectors.

An example of a MB simulation at three consecutive timeframes showcasing a very high MB concentration is shown in Figure 15, where color represents MB velocity.

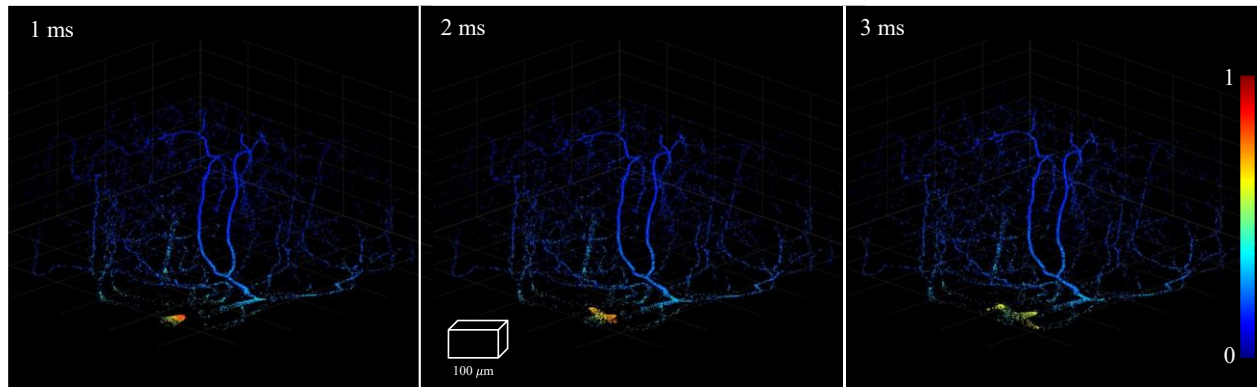


Figure 15: MB steady-state flow simulation at three consecutive timeframes.

MBs close to the vessel wall also needed to travel slower than those travelling along the centerline of the vessel. This behavior follows the parabolic law (shown more clearly on Figure 16) of a Poiseuille velocity distribution and was implemented in the simulator.

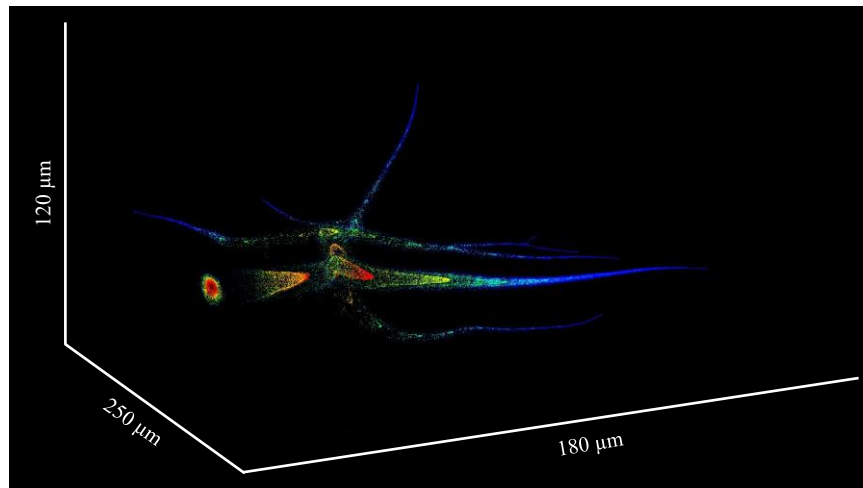


Figure 16: Raw MB positions of multiple timeframes accumulated in space to better visualize the Poiseuille parabolic velocity distribution.

We know that because of the pulsatile nature of the heart, the blood flow in efferent arteries isn't constant in time. The change in MB velocity in time can affect MB isolation in comparison with tissue. We implemented a simple pulsatility model for future studies. To emulate the effect of the pulsatility of the heart, MB velocity was modulated using a function that mimics flow variation (Figure 17). Pulsatility amplitude modulation was modelled as a heartrate of 300 beats per minute (5 Hz) to match a beating mouse heart with an amplitude of [0.5-1.5] to achieve an average normalized velocity of 1.

To be more realistic, this amplitude modulation had to be propagated from large vessels to smaller ones as a wave. This required a synchronization of MB positions in the steady state flow simulation that guaranteed a continuous pulsatile wave propagation. In practice, this was achieved by delaying newly added MBs according to the propagation of the pulsatile wave. Visually, amplitude modulation translates to an increase and decrease in MB velocity (Figure 14), while wave propagation translates to a propagation of a local velocity pattern from the larger vessels to the smaller capillaries (Figure 18 and 16).

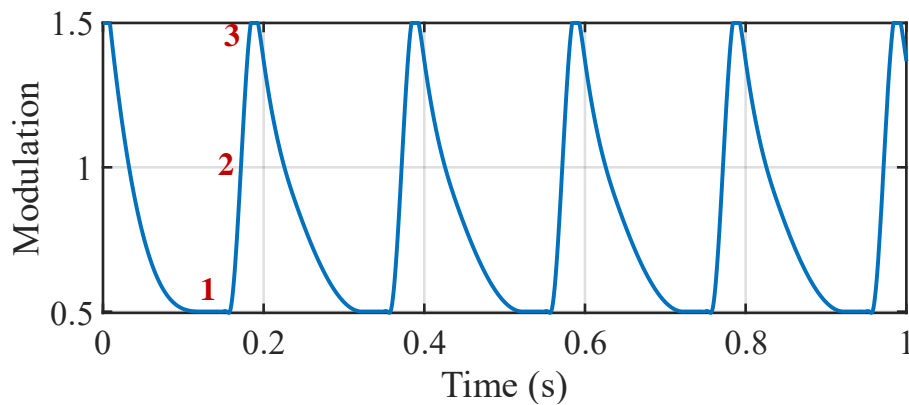


Figure 17: Pulsatile flow modulation for a mouse heart beating at 300 BPM.

In this work, pulsatility wave propagation (Figure 15 and 16) was modelled with a constant velocity of 25 mm/s extracted from [114].

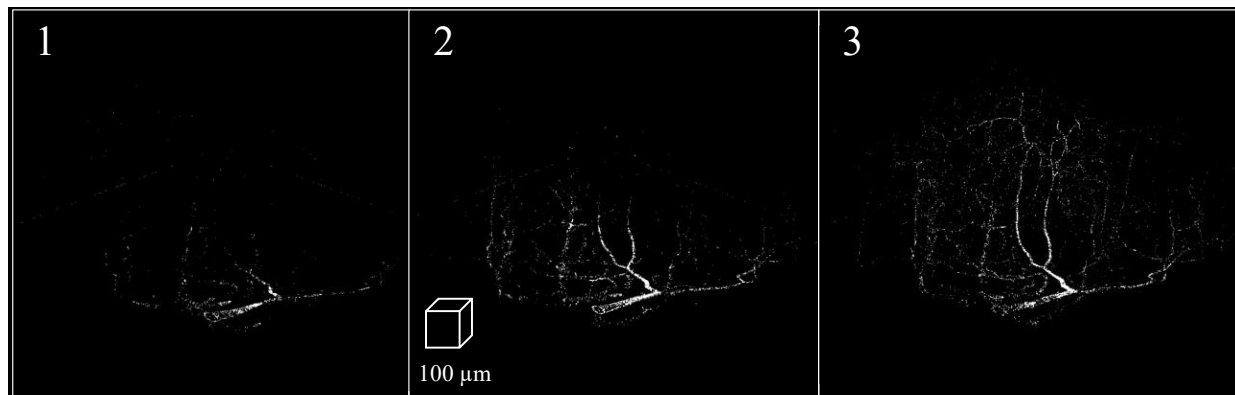


Figure 18: MB steady-state flow simulation. White dots represent individual MBs' velocities. They are only visible at a certain velocity threshold to visualize the propagation of the pulsatile flow. Snapshots from 1 to 3 correspond to three timestamps in a cardiac cycle (Figure 17).

In figure 16, we calculated the mean MB velocity in two regions of interest (ROI) of the same blood vessel to illustrate pulsatility wave propagation as a shift in MB velocity in space and time through a blood vessel. A black and a red box represent the aforementioned ROIs.

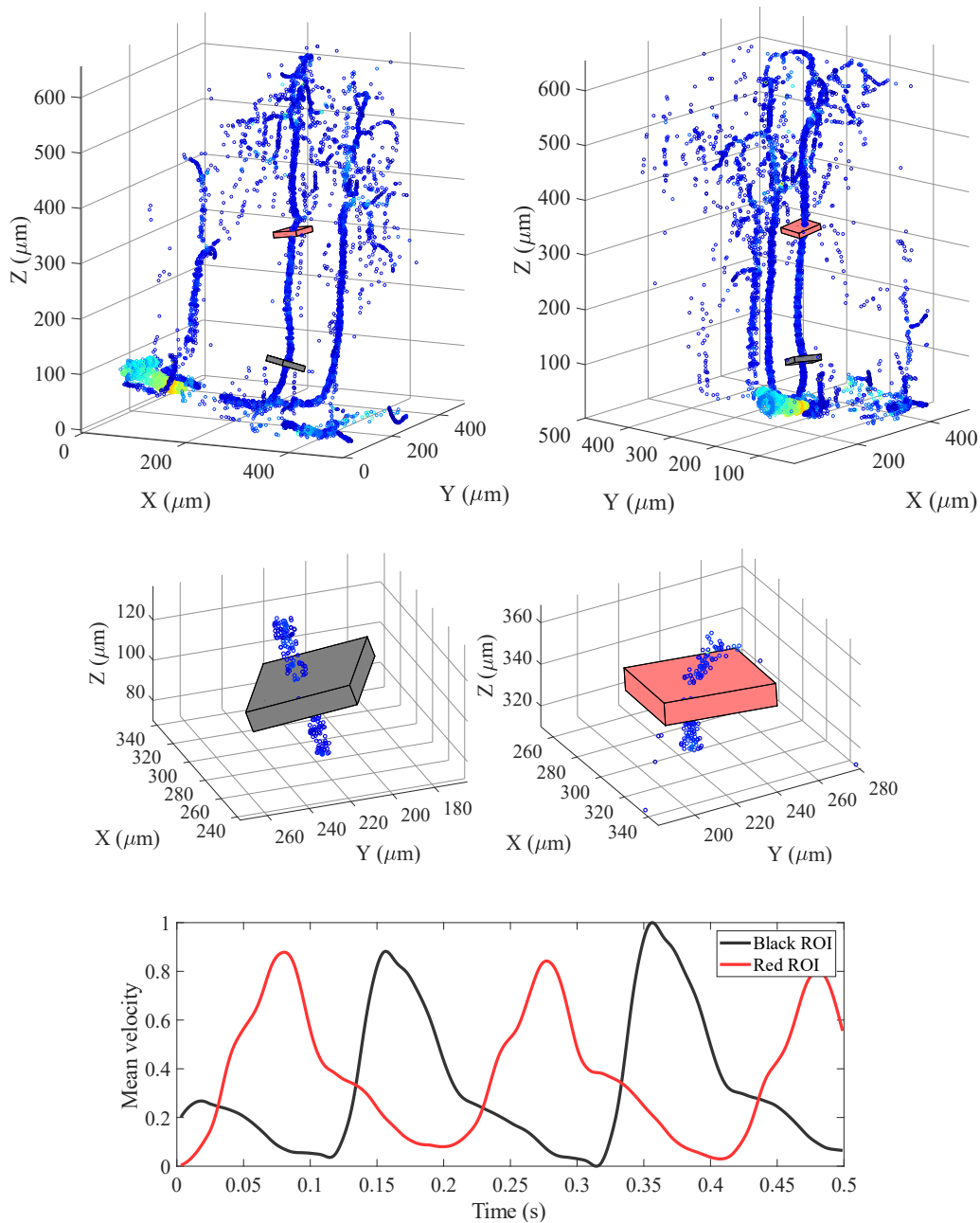


Figure 19: Wave propagation illustration. (Top) Two views of a MB steady-state flow simulation with two regions of interest (ROI) used to calculate MB mean velocity at two locations along a vessel. (Middle) Zoomed views on the ROIs. (Bottom) Mean MB velocity in each ROI.



These results are in good agreement with the wave propagation velocity and the applied velocity modulation. This pulsatility feature of the simulator could be used in subsequent studies to validate a biomarker based on pulsatile flow assessing dysfunctional brain regions where a pulsatility measurement could differentiate between a healthy and a non-healthy individual [37]. An improvement can be made by modelling pulsatility propagation as a function of vessel rigidity based on a dependency of vessel diameter.

### 3.1.3 Ultrasound localization microscopy

Before simulating ultrasound signals, since the vascular network ( $\sim 600\ \mu\text{m}$ ) is very small compared to the field of view of the transducer ( $\sim 10\ \text{mm}$ ), MBs from unique trajectories that are redistributed in a  $10 \times 10 \times 10$  pattern to cover a larger field of view (Figure 20). This was essential since the PSF of the system is not uniform, therefore MB signals should come from the whole field of view to correctly assess the performance of the imaging system. Most of the simulation of ultrasound generation, reconstruction and MB localization was performed using algorithms developed by members of the Provost Ultrasound Lab, which were programmed using MATLAB and CUDA kernels to allow for parallelization and be run on dedicated GPU. Details on the localization framework are found in sections 0 and 4.3.7. By developing simulations at various transmit frequencies, adding the contribution to noise and quantifying localization performance, I could help optimizing parameters and develop an ULM simulation framework to test for new hypotheses.

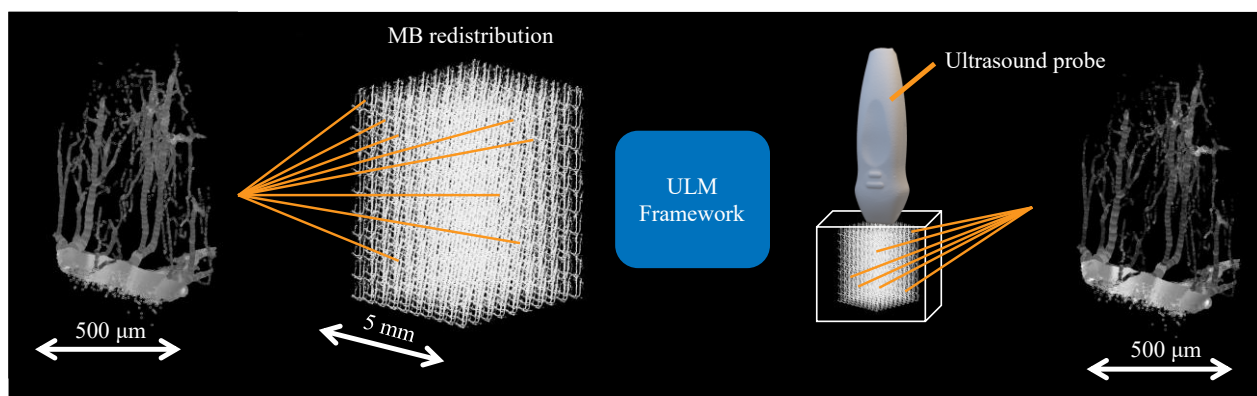


Figure 20: MB redistribution. Here are shown 1 million unique MBs from unique trajectories that are redistributed in a  $10 \times 10 \times 10$  pattern to cover a larger field of view. Since the PSF of the system is not uniform, simulation must be performed throughout most of the field of view to correctly assess the imaging system.

After ultrasound generation, reconstruction and MB localization, metrics are computed. Only then that localized MB positions are brought back together for visualization purposes where all MBs lie in the original subspace as seen in the last step of Figure 20.

## 3.2 Parametric studies

### 3.2.1 Metrics

Various parameters can be studied, and various metrics can be computed to assess a system's performance. We studied the effect of MB concentration and transmit frequency, since they directly change our ability to fulfill the requirement of isolated sources in a spatiotemporal referential [5], [80], [103]. As for metrics, we focused on quantifying acquisition time and MB localization accuracy. To quantify the accuracy of MB localization, we used the localization error metric as described in section 4.3.9. After quantifying localization error for different MB positions, we noticed differences in localization error depending on the location of the MB relative to the transducer. Figure 21 shows results of localization error as a function of MB position.

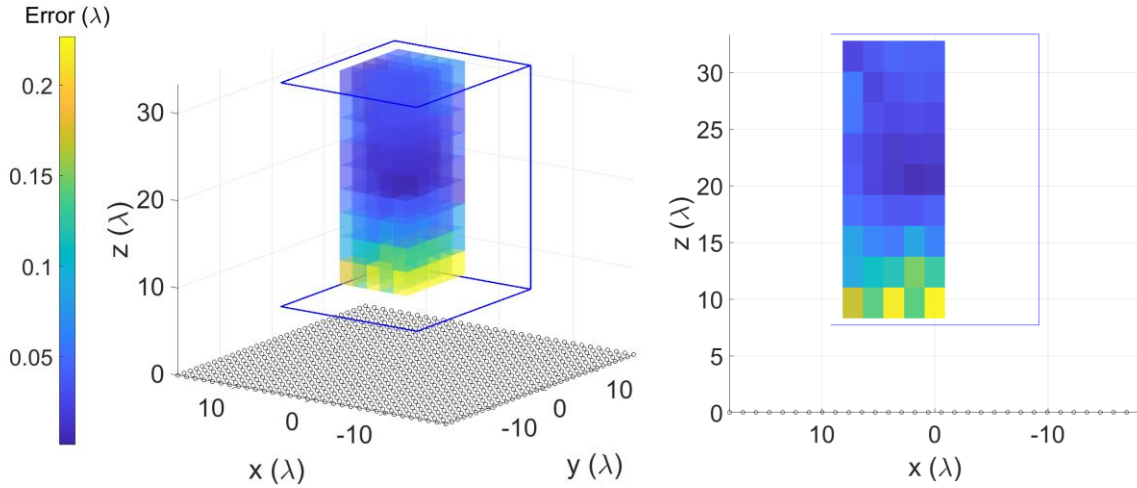


Figure 21: Localization error vs 3D position for a single MB using a 32x32 matrix array with a transmit frequency of 6 MHz. Scale was normalized as a function of the transmit wavelength ( $\lambda \sim 257 \mu\text{m}$ ). Small black circle at the bottom represent the position of the elements of the transducer facing up towards the medium. Only one quadrant was computed because of x and y symmetry.

Each data point corresponds to a simulation where a single MB was placed in the medium at a different position and was imaged and localized using the ULM framework. These results indicate that MBs should be imaged at beyond 15 wavelengths to achieve a minimum localization error under  $\frac{1}{10}$  of the wavelength.

We also tested the effect of SNR on localization error. SNR was varied by adding white gaussian noise on RF data. Only one MB bubble in the medium was imaged, localized, and localization error was computed.

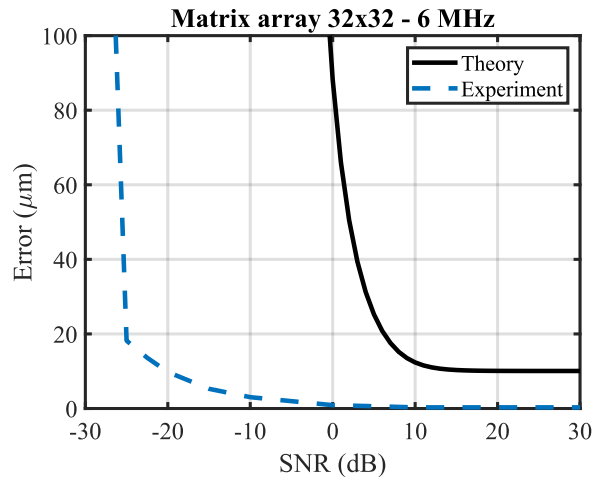


Figure 22: Norm of the lower bound on localization error at different values of SNR for a 32x32 6 MHz matrix array probe. The blue dashed line represents results from the ULM framework and the solid black represents the theoretical values extracted from equations (44)-(45).

We can see on Figure 22 that at a low SNR, localization error drastically increases. However, we can see that this effect occurs at lower SNR than theory predicts. This means that our ULM framework is less sensitive to a low SNR as currently modeled. Future work could include a similar analysis for more advanced phantom modelling as in [115].

## Chapter 4    **ARTICLE 1: AN ANATOMICALLY AND HEMODYNAMICALLY REALISTIC SIMULATION FRAMEWORK FOR 3D ULTRASOUND LOCALIZATION MICROSCOPY**

This study has been submitted at IEEE Transactions on Medical Imaging

### **Authors**

Hatim Belgharbi<sup>a</sup> hatimbelg@gmail.com

Jonathan Porée<sup>a,b</sup> jonathan.poree@polymtl.ca

Rafat Damseh<sup>a</sup> rdamseh@uaeu.ac.ae

Vincent Perrot<sup>a</sup> vincent.perrot@polymtl.ca

Léo Milecki<sup>a,c</sup> leo.milecki@centralesupelec.fr

Patrick Delafontaine-Martel<sup>a</sup> patrick.delafontaine-martel@polymtl.ca

Frédéric Lesage<sup>a,d</sup> jean.provost@polymtl.ca

Jean Provost<sup>d,e</sup> frederic.lesage@polymtl.ca

### **Affiliations**

a Institute of Biomedical Engineering, Polytechnique Montreal, Montreal, QC, Canada

b College of Information Technology, United Arab Emirates University, Abu Dhabi, United Arab Emirates

c Department of Mathematics and Software for Systems Complexity, CentraleSupélec, Gif-sur-Yvette, France

d Montreal Heart Institute, Montreal, QC, Canada

e Department of Engineering Physics, Polytechnique Montreal, Montreal, QC, Canada [116]

### **4.1 Abstract**

The resolution of 3D Ultrasound Localization Microscopy (ULM) is determined by acquisition parameters such as frequency and transducer geometry but also by microbubble (MB) concentration, which is also linked to the total acquisition time needed to sample the vascular tree at different scales. In this study, we introduce a novel 3D anatomically- and physiologically-realistic ULM simulation framework based on two-photon microscopy (2PM) and in-vivo MB perfusion dynamics. As a proof of concept, using metrics such as MB localization error, MB count and network filling, we could quantify the effect of MB concentration and PSF volume by varying probe transmit frequency (3-15 MHz). We find that while low frequencies can achieve sub-wavelength resolution as predicted by theory, they are also associated with prolonged acquisition

times to map smaller vessels, thus limiting effective resolution. A linear relationship was found between maximal MB concentration and inverse point spread function (PSF) volume. Since inverse PSF volume roughly scales cubically with frequency, the reconstruction of the equivalent of 10 minutes at 15 MHz would require hours at 3 MHz. We expect that these findings can be leveraged to achieve effective reconstruction and serve as a guide for choosing optimal MB concentrations in ULM.

## 4.2 Introduction

For long, we were bound by the limit of diffraction stated by Rayleigh's criterion [1] in conventional ultrasound imaging. Diffraction causes the point-spread function (PSF) to have a specific size in the order of the wavelength, which increases with the penetration depth: larger depths can be achieved at the cost of larger wavelength and thus degraded resolution. Wavelength thus dictates the compromise between limiting factors of resolution and penetration depth in conventional ultrasound [2]. The concept of isolated source localization from optical imaging [3], used in ultrasound localization microscopy (ULM) [2], [4], [5] challenges this compromise.

Microbubbles (MB) injected into the bloodstream are used as small, highly echogenic unique scatterers that can be tracked through vascular networks in large vessels down to, in principle, the smallest capillaries. It is by finding the exact centroid of each MB in reconstructed images or by fitting a paraboloid in RF data that we can obtain micrometer-scale resolution. This resolution is no longer dependent on wavelength, but rather on arrival time variance, number of elements, array apertures, distance between the array and MB, and sound speed [6].

The gain in spatial resolution comes at the cost of temporal resolution (in the order of a few minutes depending on the vascular network density) since sampling the vascular network requires localization and tracking of millions of MBs in tens of thousands of images [7].

In [2], Couture et al. defined four conditions that are required to perform ULM, namely 1) being sensitive to the contrast agent, 2) being able to localize that contrast agent, 3) record at a high framerate and 4) maintain isolated sources in a spatiotemporal referential. Our ability to respect the latter condition depends mainly on two factors: 1) acquisition parameters such as frequency and transducer geometry [6], and 2) microbubble concentration [7].

To quantify ULM limitations, studies have been performed in in-vitro phantoms with various materials, configurations, and scale. Viessmann et al. [8] conducted four experiments at 2-2.5 MHz with the last one using two touching cellulose tubes with inner diameters (ID) of 200  $\mu\text{m}$ . Two sets of MB could be distinguished with a sub-diffraction limit with a measured center-to-center distance of 197  $\mu\text{m}$  (wavelength of 616-770  $\mu\text{m}$ ), but this setup was limited to relatively large mono-diameter tubes. Similarly, in [9], O'Reilly and Hynynen conducted an experiment at 612 kHz using a PTFE tube with 255  $\mu\text{m}$  of ID spiraled around a 2.5 mm rod. The estimated localization uncertainty was again sub-diffraction limit with approximately 1/120 and 1/60 of the wavelength, but the limiting factor was the size of the phantom. In [10], Couture et al. succeeded in localizing MB in 100  $\mu\text{m}$  sized microfluidic systems at 5 MHz. Similarly, in [11], Desailly et al. succeeded in localizing MB in rectangular 40-100  $\mu\text{m}$  by 80  $\mu\text{m}$  PDMS channels out of printed SLA molds separated by 50 to 200  $\mu\text{m}$  at 1.75 MHz. However, none of the above setups' scale, complexity and realism reflects in-vivo challenges. In mice, brain vascular networks typically exhibit large vessels with diameters in the 50-200  $\mu\text{m}$  range [12] down to very small vessels in the <10-micrometer range [13]. As for how close vessels are to each other, vascular density varies from 161-391 sections per  $\text{mm}^2$ , or 51-79 micrometers between them [14]. Furthermore, the size of the vessel intrinsically dictates the number of flowing MB and their velocities, which affects effective resolution [7]. To our knowledge, there is no validation framework for ULM image formation algorithms based on anatomically-realistic MB flow to assess ULM limitations.

To overcome this problem, a highly resolved ground truth of brain vasculature is needed. Pulsed laser systems [15], [16], e.g., two-photon microscopy (2PM), can image in-vivo and ex-vivo brain tissue at micrometer scale. This approach can also be scaled by stacking ex-vivo slices to reconstruct whole brain anatomy with micrometer scale resolution [17], [18]. Cerebral vascular networks that can therefore be leveraged as virtual phantoms [19]. We developed a three-dimensional particle flow simulator based on highly resolved 2PM data from mice brain vasculature to conduct anatomically-realistic simulations. It was first implemented in 2D as part of a deep learning framework [20] and as part of a sparse channel sampling study for ULM [21].

In this work, we introduce a novel 3D simulation framework for the validation of ULM image formation algorithms. From a vascular model obtained using 2PM, we generate a MB flow with

known MB positions in time and where dynamics mimic MB behavior from in-vivo data [7]. These MB positions at controlled concentrations are then used to position scatterers in a medium that are used to simulate ultrasound raw data, which can then be input in a ULM image formation algorithm. This setup allows to evaluate the performance of MB localization frameworks with various imaging parameters, by comparing the output MB positions with the provided reference MBs. As an example application, we studied the effect of MB concentration and transmit frequency by computing metrics such as localization error and network filling. We provide new investigations that link maximal MB concentration with the inverse of the PSF volume. Such investigations are essential in optimizing MB concentration to obtain a more complete and precise vascular reconstruction.

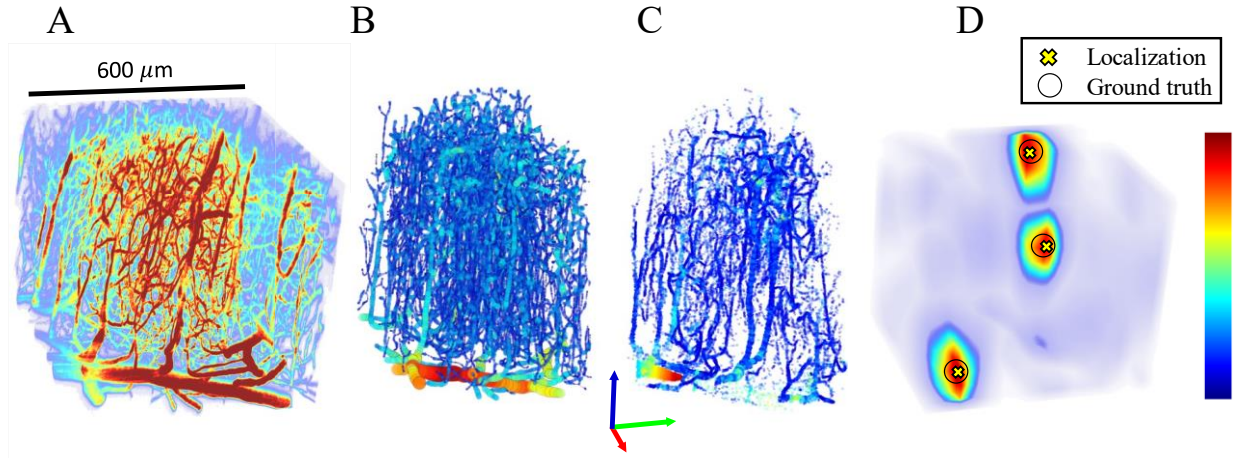


Figure 1: Simulation framework. All sub-figures are scaled to match the same scalebar. A) Two-photon microscopy (2PM) of in-vivo mouse brain is acquired. Colormap represents fluorescence intensity. B) From the 2PM data, a graph model is generated in 3 stages described in [22]. Colormap represents nodes' corresponding vessel size. C) Particle trajectories are generated using the graph model and in-vivo diameter-velocity dependency. Colormap represents MB velocity. D) Using a GPU-based US simulator, RF signals are generated and reconstructed to obtain 3D+t US data, on which a correlation-based localization algorithm is applied. Colormap represents the correlation obtained using a spatial convolution of the beamformed PSF and reconstructed IQ data.

## 4.3 Methods

### 4.3.1 In-vitro two-photon microscopy

The framework starts with a highly resolved mouse brain vasculature acquired using 2PM from [23] (Figure 1 A.). Prior imaging, C57BL/6 mice (25–30 g males,  $n = 6$ ) were anesthetized by isoflurane (1–2% in a mixture of  $O_2$  and air) at a temperature of  $37^\circ\text{C}$ . The imaging apparatus consisted of a custom-built two-photon microscope with components listed in [24]. Imaging was performed through a cranial window with removed dura and a  $150\text{ }\mu\text{m}$ -thick microscope coverslip for sealing purposes. Anesthesia was reduced to 0.7-1.2% isoflurane during the acquisition. Structural images of cortical vasculature were obtained by labelling blood plasma with dextran-conjugated fluorescein at  $500\text{ nM}$ . Using angiograms acquired with a 20X Olympus objective (Numerical Aperture = 0.95), 6 stacks of vasculature (Figure 5) were prepared with voxel sizes of  $1.2\times 1.2\times 2.0\text{ }\mu\text{m}$  and total volume of  $600\times 600\times 662\text{ }\mu\text{m}$ .

### 4.3.2 Graph model

Using a modeling framework from [22], [25], a graph model of 2PM data was generated (Figure 1B). In this framework, vascular segmentation was performed using fully-convolutional neural network based on densely connected layers [22]. The graphing/skeletonization step was achieved by generating a 3D grid-graph model followed by a geometric graph contraction and refinement algorithms. Training the segmentation model was done using the Theano framework [26]. As for 3D modeling and geometric contraction processes [25], they are based on the VascGraph Python package [25]. Using this framework, a file containing vessel network geometry and topology (nodes and edges), with their corresponding inlet and outlet vessels is generated. The corresponding vessel radii are assigned as features to the nodes of the vascular network. Vessels ranged from 2 to  $57.2\text{ }\mu\text{m}$  in diameter, their spatial position span was  $500\times 500\times 650\text{ }\mu\text{m}$  and vessel volumetric density (VD) was calculated at 4%, using the ratio of vessels-containing voxels and total voxels in segmented volumes.

### 4.3.3 Particle trajectory generation

Before generating a steady state flow simulation where MB concentration is always kept constant, MB trajectories were computed using the graph model source nodes, target nodes and vessels radii.



For each trajectory, the shortest path between a source node and a random extremity node was calculated using vessels radii squared as weights. Since original nodes are arbitrarily spaced, a cubic spline fitting was then applied to allow for the generation MB positions with a controlled time-dependent spacing. In Hingot et al. [7], MBs were followed for 5 minutes in a rat model with a continuous injection of the equivalent of 0.8 mL/kg of Sonovue MBs. MB velocities were calculated, and a log-log fit of velocity ( $y$ ) as a function of vessel diameter ( $x$ ) was performed on a 150 vessels sample with  $\ln(y) = p_1 \ln(x) + p_2$  with parameters  $p_1 = 1.9 \text{ mm } \mu\text{m}^{-1} \text{s}^{-1}$ ,  $p_2 = -6 \text{ mm.s}^{-1}$ . Another log-log fit was computed on MB count ( $y$ ) as a function of diameter ( $x$ ) with parameters  $p_1 = 3.7 \text{ MB } \mu\text{m}^{-1}$ ,  $p_2 = -8.2 \text{ MB}$ , which is used in the following section (*steady-state flow*) for trajectory selection. All node-node distances ( $d_i$ ) were computed according to (1), where  $v_i$  is the velocity from the velocity-diameter relationship of in-vivo data,  $dt$  is the timestamp and  $P$  a random normalized Poiseuille coefficient. The Poiseuille coefficient dictates the distance from the center of the vessel. The higher the coefficient, the faster is the MB and closer it is to the center of the vessel.

$$d_i = v_i \cdot dt \cdot P \quad (1)$$

$v_i$  was calculated using the relationship with the diameter from [7]. Vessels in our network ranged from 2 to 57.2 micrometers in diameter, therefore velocities ranged from 0.01 mm/s to 5.4 mm/s. A MB trajectory is terminated if the trajectory reaches an end node or if the MB can no longer flow in the vessel due to a size constraint. In our simulations, we modelled the MBs to be of 2 micrometers in diameter, therefore all trajectories reached their maximum length. After the computation of all node-node distances ( $d_i$ ), the trajectory at the center of vessels (i.e., a centerline trajectory) was then used to generate other parallel trajectories to span the entire vessel. To do so, two orthogonal perpendicular vectors were calculated for each trajectory. Using a linear combination of those vectors, all orientations were created to span all possible trajectories. This step allowed for the generation of multiple trajectories at different radial positions in a specific

vessel, according to their Poiseuille coefficient. Trajectories were modelled parallel to the vessel wall, i.e., being laminar as an approximation of the normal physiological state [27].

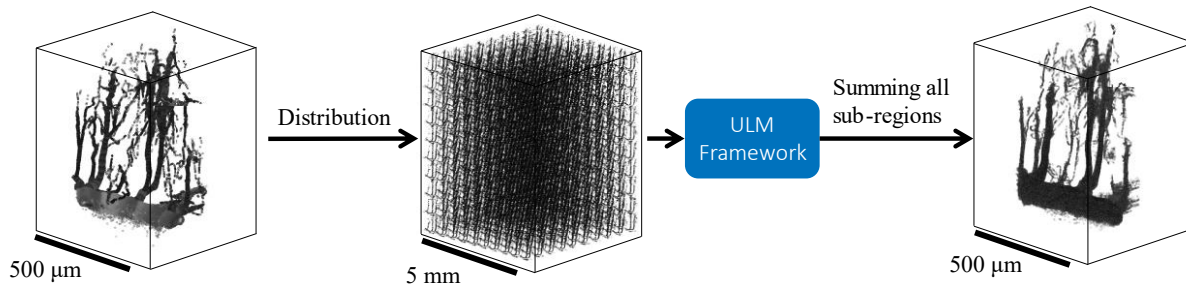


Figure 223: Unique microbubbles positions were randomly distributed in a  $10 \times 10 \times 10$  pattern to span over  $5 \times 5 \times 6.5$  mm. This example shows 1 million MB distributed in 1000 sub-regions, which results in 1000 MB in each sub-region. Even though fewer small vessels are present in each sub-region, this step is essential since the PSF is not uniform in the field of view and it also allows to span a usable MB concentration range. After the ULM framework and metrics computation, MB positions in sub-regions can be added back together in the original size volume to emulate a longer acquisition time for visualization purposes.

#### 4.3.4 Steady-state flow

Using computed microbubbles trajectories, a steady-state flow was generated using a constant concentration of MBs (Figure 1 C). The selection of MB trajectories was made according to their mean diameter to match in-vivo data from [7]. To match this model, MB trajectories were sorted according to their mean diameter and a probability density function generated according to the model was applied for trajectories selection. To populate the steady-state flow volume, a first population of particles was generated at random positions in their respective trajectory to match a desired concentration, then, a new microbubble was added each time a microbubble reached the end of its trajectory. After this process, we were left with sets of constant number of microbubbles positions  $(X_i, Y_i, Z_i)$  at each time frame.

#### 4.3.5 Scatterers' arrangement

Unique microbubbles positions from a vascular network were randomly distributed in a  $10 \times 10 \times 10$  pattern to span over  $5 \times 5 \times 6.5$  mm (Figure 2). Since the volume of the original vascular network was minute, this setup allowed to increase the usage of the field of view and to better assess the performance of the imaging system, since the PSF is not uniform throughout the field of view. Moreover, this arrangement allowed to span a usable range of MB concentrations. For example, in the original configuration, only one MB flowing in the network corresponded to more than 5 MB/mm<sup>3</sup>, which is considerably high. Therefore, in this configuration, we have a 1000-fold discretization on the original MB concentration range. After ultrasound simulation, reconstruction, localization, and metrics computation, MB positions from the 1000 sub-regions were added into one original small volume to emulate a longer acquisition time only for visualization purposes (Figure 2). This step facilitated the qualitative comparison between density maps shown in Figure 7.

Table 5: Acquisition parameters

PROBE ARRAY	TRANSMIT FREQUENCY (MHz)	CENTER FREQUENCY ( $C_f$ ) (MHz)	BANDWIDTH (MHz)
128x1	15.625	15.625	14-22
32x32	3	3.47	$C_f \cdot [0.7, 1.3]$
32x32	3.5	3.47	$C_f \cdot [0.7, 1.3]$
32x32	6	7.81	$C_f \cdot [0.7, 1.3]$
32x32	7	7.81	$C_f \cdot [0.7, 1.3]$
32x32	9	7.81	$C_f \cdot [0.7, 1.3]$
32x32	12	12	$C_f \cdot [0.7, 1.3]$
32x32	15	15	8-22

#### 4.3.6 Ultrasound Simulation

For 2D imaging, probe parameters matched a L22-14 linear array of 128 elements, central frequency of 15.6 MHz, pitch of 0.1 mm and element width of 0.08 mm (Vermon, France). For 3D imaging, probe parameters were set to match 32x32 matrix arrays 1024 EL 3 MHz [28], 1024 EL 8 MHz [29], [30] and the custom 1024-element 15 MHz as used by Brunner et al. [31]. The theoretical 12 MHz probe parameters were set to match the 3- and 8-MHz probes' specifications. Bandwidths and transmit frequencies are depicted in TABLE I. Pitch and element width were set to 0.3 and 0.275 mm, respectively, the transmit pulse was a 0-degree plane wave of 4 cycles, and the effective framerate was equal to the PRF of 1 kHz.

To simulate the acoustic response of the microbubbles, an in-house GPU implementation of the SIMUS simulation software was performed as described in [32], [33]. Gaussian white noise was added to the acoustic response to obtain a signal to noise ratio (SNR) of 15 dB in 2D and 10 dB in 3D.

#### 4.3.7 ULM image formation algorithm

IQ volumes were generated from the RF data using a fast GPU-based delay-and-sum beamformer [34]. Individual MB were then identified as local maxima on correlation maps, resulting from the correlation of the reconstructed IQ volumes with the IQ PSF of the imaging system. MB were precisely located using a 3D subpixel gaussian fitting on IQ local maxima. Localized MB were sorted as a function of their correlation from the correlation map. Only MB exceeding a certain correlation threshold were kept. Thresholding using correlation allows to screen interacting MBs. This is essential to meet the condition stated by [2], which requires isolated sources. To establish the optimal threshold, tests were conducted on various concentrations at specific transmit frequencies. After finding concentration that yielded most localized MBs, localization error was plotted against correlation threshold (Figure 3). Threshold was selected to maximize MB count while preventing excessive localization error.

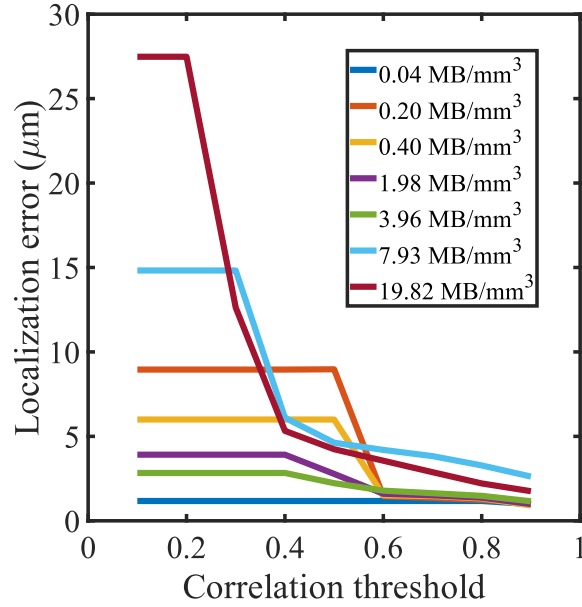


Figure 3: Example of a simulation conducted with the linear array at 15.625 MHz at different MB concentrations. Localization error was calculated as a function of correlation threshold. Only MB with correlation higher than the threshold were selected. In this specific case, final threshold for further simulations would be 0.6 to prevent a surge in localization error from interacting MBs.

For visualization purposes and for reconstruction times calculations, density maps were generated. MB subpixel positions were accumulated over time on a 3D sampled volume, where each voxel is approximately  $\frac{\lambda}{50}$ , to generate a micro vasculature density map, where  $\lambda$  represents the wavelength. On a density map, each voxel intensity represents the number of microbubbles in that specific voxel.

#### 4.3.8 MB simulator metrics

To validate MB behavior, 5000 MB trajectories were simulated to replicate similar MB count as in [7]. The two dependencies from in-vivo data are 1) the MB count as a function of vessel diameter and 2) MB velocity as a function of vessel diameter. To assess the first dependency, a histogram was computed based on the occurrences of the different diameters of all MBs at all positions. The number of histogram bins was selected as the number of integer values of the MBs radii. Natural

logarithm ( $\ln$ ) was applied on both dependencies to generate a linear fit as in [7]. As for the second dependency, MB velocity was simply plotted against its corresponding vessel diameter.

#### **4.3.9 ULM metrics**

To quantify the effect of concentration on the localization itself, localization error was computed using highly correlated MB positions. First, each localized MB was paired with the closest reference MB using Euclidian distance. In 2D, only in-plane distances were considered. For a specific concentration, localization error was calculated as the average distance between localized MBs and their corresponding closest reference MB. Concentration was calculated as the number of MBs in a cartesian volume. This process was performed in 2D at 15.625 MHz and in 3D for different transmit frequencies spanning current usable range: 3, 3.5, 6, 7, 9 12 and 15 MHz.

Since the MB count is directly linked to reconstruction time [7], it was used as a metric to quantify the latter. After correlation thresholding, the MB count was measured at the mentioned transmit frequencies and at various concentrations. Concentrations were chosen iteratively to span a range where the MB count naturally increases with an increase in concentration and decreases when concentration is high enough that MB interactions become more important, and less MBs are selected due to a lower correlation with the PSF. This allowed to find a maximum in the MB count, which was later linked to the PSF volume.

To assess effective reconstruction, density maps were generated using accumulated MB positions over different acquisition times. Selected MB concentrations corresponded to 10% of the concentrations where MB count was maximal for each transmit frequency. A reference density map with a fully populated network was generated by simulating all possible MB trajectories without a constraint on MB count ( $N$ ) vs diameter. A quantitative comparison with the reference density map was made at different acquisition times using the Sørensen–Dice coefficient [35], [36]: a similarity index quantifying the network filling.

To establish the link between PSF size and MB concentration, the PSF volume was calculated for each of the different transmit frequencies and concentration at which MB count is maximal was considered as optimal. PSF was modelled as an ellipsoid with semi-axes calculated using half of the full width at half maximum (FWHM) in each dimension. For 2D imaging, ellipsoid semi-axis in the elevation plane was calculated as half of the elevation focus.

## 4.4 Results

### 4.4.1 Simulated MB trajectories statistics match in-vivo data

Figure 4 displays the two dependencies that were originally extracted from in-vivo data [7]. The black lines represent the reference dependencies, colored dots represent the statistics of simulated MBs, and the blue dashed lines represent the linear fits on the simulated data. Each dot color corresponds to one of six vascular networks. Results show that the MB count increases with vessel diameter with a slope of 4.15 compared to 3.7 in reference. MB velocity also increases with vessel diameter with a slope of 1.77 compared to 1.9 in reference. Figure 5 shows the different MB flow simulations from 6 vascular networks. Each of the simulations contains an accumulated 1 million MB positions. In Figure 5, the top section depicts simulations where MB flow was constrained to follow the dependencies mentioned above. The bottom section in Figure 5 shows MB flow simulations without the constraint on MB count vs the vessel diameter. The latter simulates a random MB distribution.

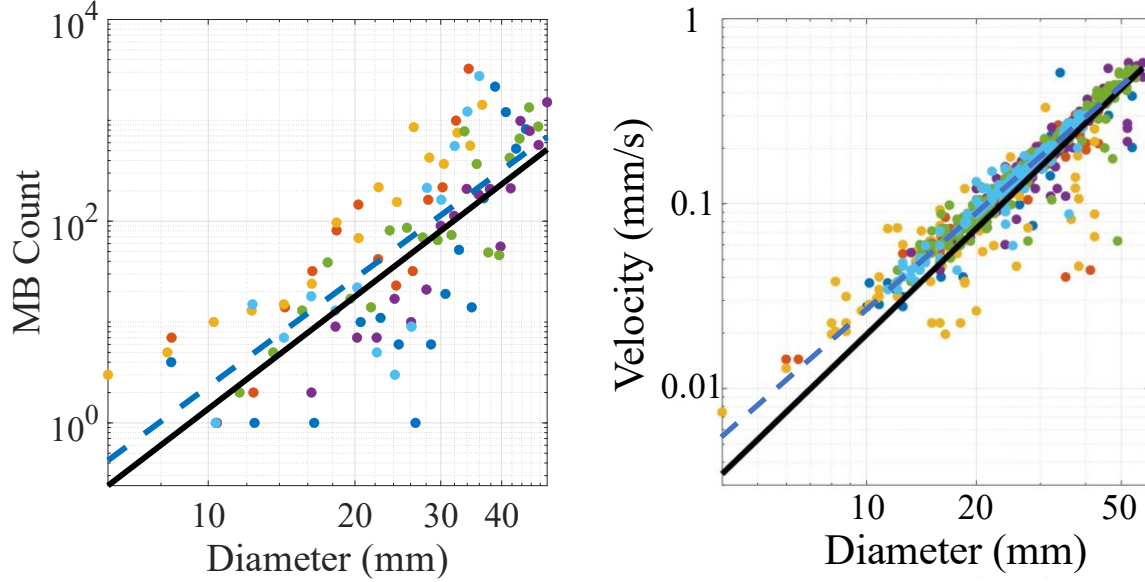


Figure 4: The MB flow simulator is based on two dependencies from [7], namely MB count vs vessel diameter and MB velocity vs vessel diameter. Both dependencies are in a logarithmic scale as in [7]. A number of 5000 MB trajectories were generated to match the sample statistics from [7]. (Left) A histogram of the occurrences of MB mean diameters was computed. Dots corresponds to the MB count in each histogram bin vs corresponding vessel diameter. Each dot color corresponds to one of six vascular networks. The dashed blue line represents a log-log fit as  $\ln(y) = p_1 \ln(x) + p_2$  with  $p_1 = 3.56$  and  $p_2 = -7.4$ ,  $R^2 = 0.59$ . Diameter  $x$  is in mm and MB count  $y$  is unitless. Black line represents reference relationship with  $p_1 = 3.7$  and  $p_2 = -8.2$ . (Right) Dots corresponds to MB velocities vs their corresponding vessel diameter. Each dot color corresponds to one of six vascular networks. The dashed blue line represents a log-log fit as  $\ln(y) = p_1 \ln(x)$  with  $p_1 = 1.75$  and  $p_2 = -5.4$ ,  $R^2 = 0.98$ . Diameter  $x$  is in mm and velocity  $y$  is in mm/s. Black line represents reference relationship with  $p_1 = 1.9$  and  $p_2 = -6$ .



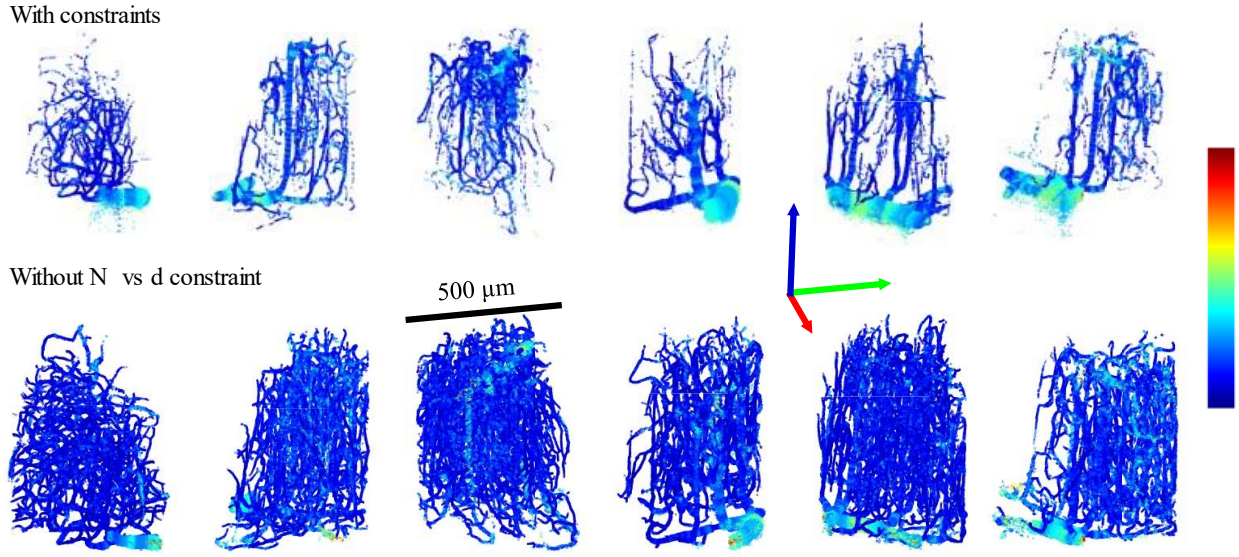


Figure 5: MB positions in 6 vascular networks of mice brains. (Top) MB flow was simulated with constraints to follow in-vivo dependencies: MB count and velocity with respect to the vessel diameter. (Bottom) MB flow was simulated without the MB count (N) vs vessel diameter (d) constraint.

#### 4.4.2 Localization error is more sensitive to concentration at lower transmit frequency

In Figure 6, localization error is depicted as a function of microbubble concentration for the different transmit frequencies. For a given transmit frequency, the bold line represents the average ( $\mu$ ) localization error of all localized microbubbles, and the shaded area covers the average  $\pm$  the standard deviation ( $\sigma$ ) of those localization errors. Only the in-plane distances were considered when computing 2D localization error of the linear array, i.e., the error in the elevation direction was ignored.

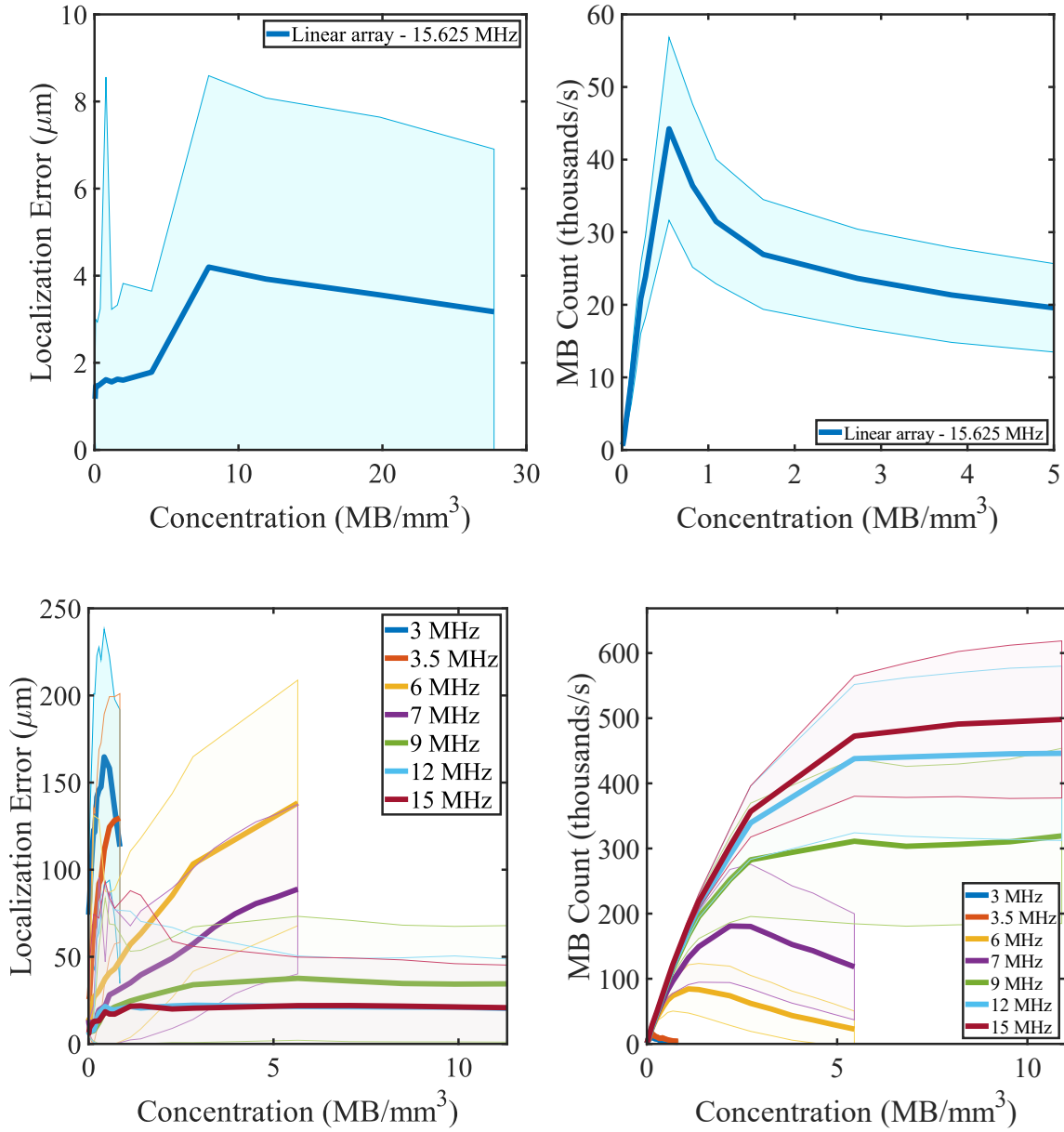


Figure 6: (Top left) 2D localization error is depicted as a function of microbubble concentration for the 15.625 MHz linear array. (Bottom left) 3D localization error is depicted as a function of microbubble concentration for matrix arrays at various transmit frequencies. The bold curve represents the average localization error between a localized MB and the closest reference MB. The shaded area covers the average  $\pm$  standard deviation. (Top right). MB count resulting from localization as a function of concentration is depicted for the 15.625 MHz linear array. The

shaded area covers the average  $\pm$  standard deviation of the 6 vascular networks. (Bottom right) MB count resulting from localization as a function of concentration is depicted for different transmit frequencies using matrix arrays. Again, the shaded area covers the average  $\pm$  standard deviation of the 6 vascular networks.

#### **4.4.3 Acquisition time is drastically reduced at higher transmit frequency**

Figure also shows the count of localized MB as a function of concentration. At lower frequencies, MB count increases until reaching a maximum and decreases at higher concentrations. However, from 9 MHz, MB count reaches a plateau at higher concentrations. We see that at 3-3.5 MHz, the number of detected MB is approximately 10 000 MB/s or 10 MB per frame. If we double the transmit frequency (6-7 MHz), the MB count increases with an order magnitude with approximately 100 000 to 200 000 MB/s. The rate at which the number of MB events increases seems to decrease with higher frequencies.

#### **4.4.4 Higher concentrations reduce reconstruction fidelity**

Figure 7 shows the effect of concentration on vascular reconstruction. We applied the simulation framework in 3D using a transmit frequency of 6 MHz at four different concentrations: 0.16, 0.4, 0.8 and 1.6 MB/mm<sup>3</sup>. They correspond to 20, 50, 100 and 200 MB in the field of view and to 10%, 25%, 50% and 100% of the maximal MB concentration derived from Figure 6. The four concentrations were chosen iteratively, using localization error and number of localized MBs as guidelines to span a usable concentration range and to depict differences in resulting vasculature reconstruction. Top of Figure 7 shows the density maps of sub-regions of reference and localized microbubbles at increasing concentrations from left to right. Bottom of Figure 7 shows density maps acquired at different transmit frequencies, increasing from left to right. MB concentration was selected as 50% of maximal concentration (0.12 MB/mm<sup>3</sup>) for a 3 MHz transmit frequency.

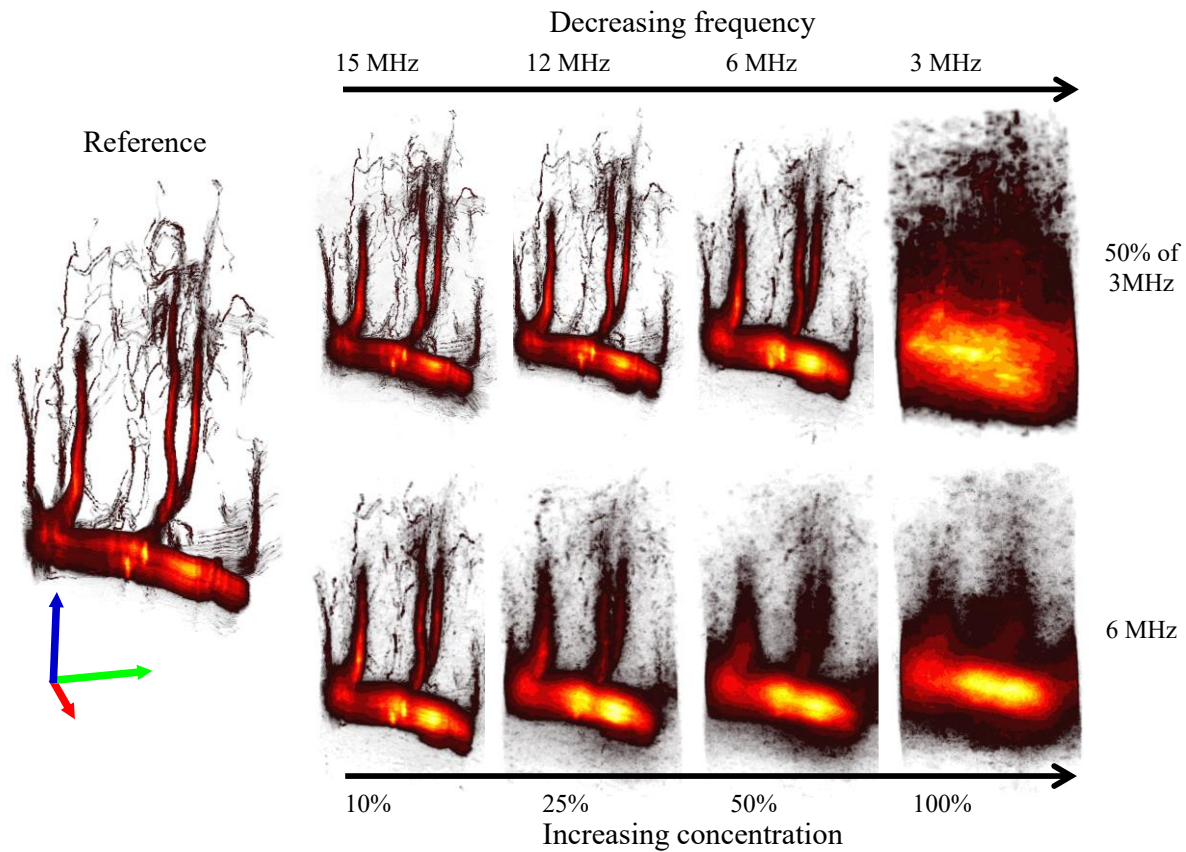


Figure 7: Sub-volumes of density maps of vascular network #5 corresponding to localized MB at different concentrations compared to known MB positions (ref) using a 32x32 matrix array at 6 MHz. (Top) Concentrations from low to high: 0.16, 0.4, 0.8 and 1.6 MB/mm<sup>3</sup>, which correspond to 20, 50, 100 and 200 MB in the field of view and to 10%, 25%, 50% and 100% of the maximal MB concentration derived from Figure 7 for a 6 MHz transmit frequency. (Bottom) For a concentration of the equivalent of 50% of the MB concentration associated with the largest number of detected MB above threshold for a 3-MHz probe (0.12 MB/mm<sup>3</sup>), density maps of sub-regions of simulations with transmit frequencies of 3, 6, 12 and 15 MHz respectively are shown.

#### 4.4.5 Maximal MB concentration is PSF size dependent

Figure 8 shows the link between maximal MB concentration and PSF volume, where maximal MB concentration is proportional to the inverse of PSF volume. The uncertainty bars span the mean  $\pm$  the standard deviation of the maximal MB concentration from the 6 available vascular networks.

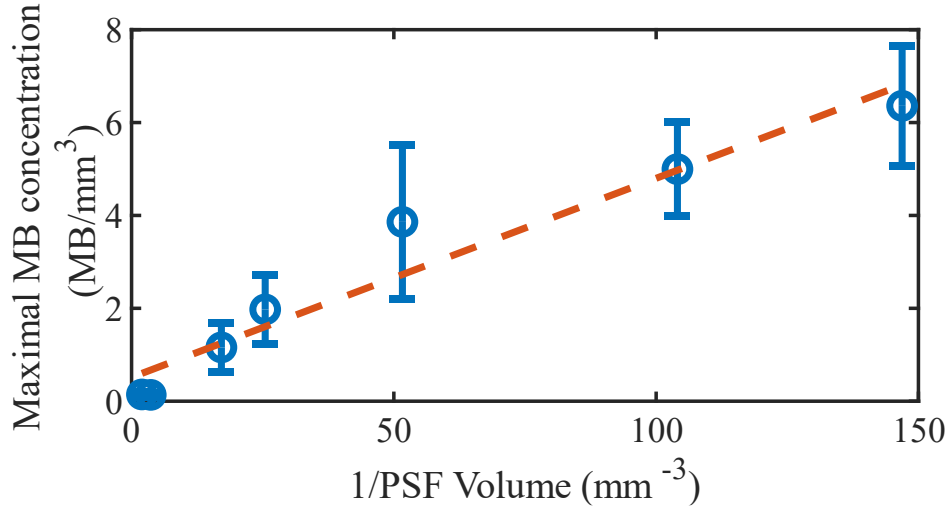


Figure 8: Concentration at which MB count is maximal (100%) is depicted as a function of the inverse of the beamformed PSF volume. From left to right in blue, inverse PSF volumes correspond to transmit frequencies of 3, 3.5, 6, 7, 9, 12 and 15 MHz of the matrix arrays. The dashed orange line represents a linear fit as  $y = 0.043x + 0.51$ ,  $R^2 = 0.94$ . The inverse PSF volume  $x$  is in  $\text{mm}^{-3}$  and maximal MB concentration  $y$  is in  $\text{MB}/\text{mm}^3$ . The uncertainty bars span the mean  $\pm$  the standard deviation of the maximal MB concentration from the 6 vascular networks.

#### 4.4.6 PSF volume dictates effective reconstruction time

Figure 9 shows the network filling using the Sørensen-Dice similarity index over time for the optimal concentrations corresponding to each transmit frequency.

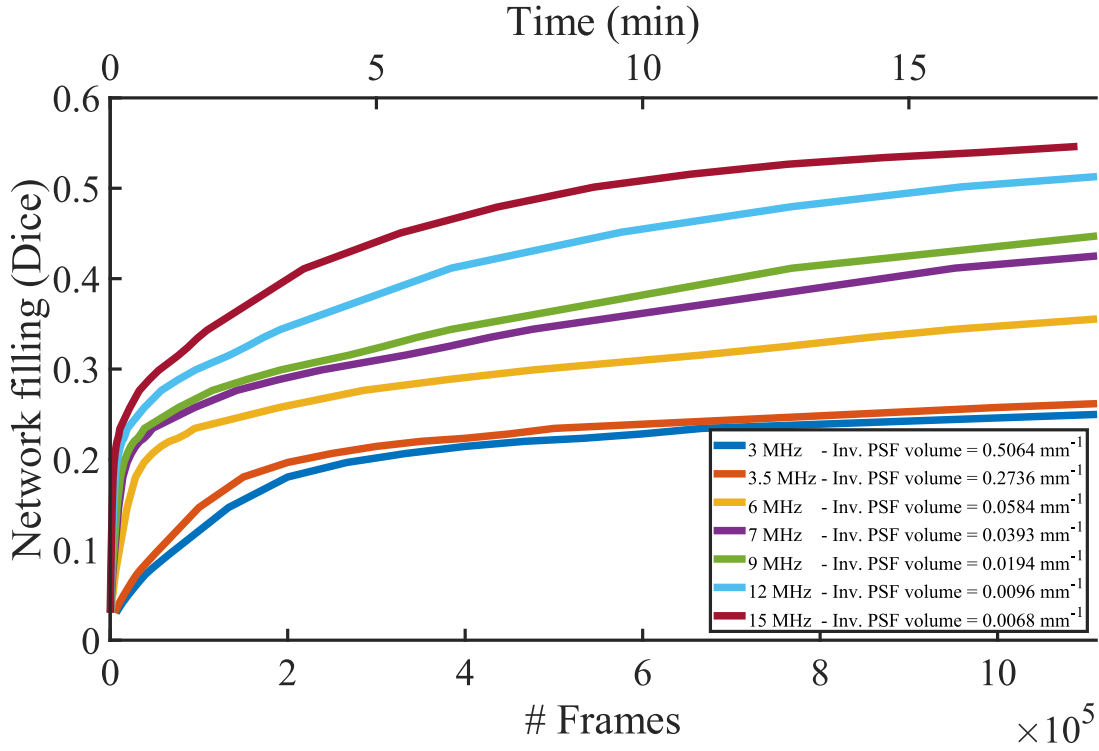


Figure 9: Network filling is shown using the similarity index between density maps at different acquisition times compared to a reference density map of a fully populated vascular network. MB concentrations correspond to 10% of the maximal MB concentration at each transmit frequency. Time is computed considering a framerate of 1000 frames per second, where each frame corresponds to an imaging volume.

#### 4.5 Discussion

In this study, we took advantage of a novel 3D anatomically-realistic framework, where mice brain vasculature obtained from 2PM was used to propagate virtual MBs with velocities and MB distribution replicating behavior from in-vivo data. Having access to known MB positions at all times allowed for quantitative measurements to determine ULM capabilities as well as reference qualitative imaging. 2D and 3D localization error could be computed as well as MB count for different MB concentrations and transmit frequencies. A link between maximal MB concentration and PSF volume was found and network filling as a function of time was calculated. Results allow to answer fundamental questions related to in-vivo imaging such as whether the vasculature is

precisely or fully depicted as imaging parameters such as the probe or concentrations used are varied.

Simulations were conducted on the 6 vascular networks separately. The variety of vascular morphologies allowed to generalize the link between MB concentration and acquisition parameters while reducing potential overfitting.

#### **4.5.1 MB simulation**

Figure 4 shows that our MB simulation framework was successful at replicating observed MB behavior from in-vivo dependencies, namely the MB count and velocity vs vessel diameter. Due to these dependencies, realistic MB flow and MB distribution are possible in subsequent ultrasound simulations.

Figure 5 shows that constraints on MB flow favor MB distribution towards larger vessels. Visually, fewer small vessels are mapped for a set amount of MBs, but large vessels appear fuller. This means that for a set acquisition time and a set MB concentration, some small vessels will not or will not be fully mapped in the final density map regardless of imaging resolution.

#### **4.5.2 MB localization**

In Figure 7, we see that as concentration increases, even though most vessels are preserved, they appear blurred, are missing, or are inaccurately depicted from the reference density map. This is in accordance with theory since ULM requires isolated MB signals. The higher the concentration, the more likely MBs will interact with each other. However, relative concentration around 10% of the concentration at maximal MB count allows to depict most of the original vasculature. Furthermore, reference density map shows that because of realistic MB count vs diameter, some small vessels are not present. Probability of a MB flowing in vessels of only a few micrometers is so low that it would require a longer acquisition time than the equivalent of 10 minutes at 15 MHz, according to results in Figure 9. This means that in current in-vivo imaging, some vessels of only a few micrometers are most likely not mapped if the transmit frequency is not high enough or the acquisition time not long enough.

In Figure 6, the decrease in MB count at high MB concentrations shows that thresholding MBs using their correlation with beamformed PSF allows to screen for intensely interacting MBs. Localization error increases with concentration as predicted by theory and is in conjunction with vessels blurring or missing. Localization error can reach a plateau at higher frequencies when selected MBs becomes constant due to correlation thresholding. Higher transmit frequencies are associated with lower localization errors as predicted by theory [37]. Higher frequencies are associated with smaller PSFs; hence a higher concentration is possible while maintaining isolated sources.

In Figure 6, the rate at which MB count increases eventually slows down with higher frequencies. This is mainly due to the size of the PSF only decreasing in the axial direction because of a constant element pitch and width. This is due to current manufacturing capabilities that limit piezoelectric element size.

The dependency in Figure 8 shows that PSF volume can be used to predict maximal MB concentration. In theory, to reduce MB interactions, MB concentration must be decreased. We see here that reducing PSF size also reduces MB interactions. Since MB concentration should be as high as possible to reduce acquisition time, this dependency can be used for choosing optimal concentration for a specific probe's acquisition parameters.

In Figure 9, the network filling represents the intersection between reference density maps and density maps resulting from MB localization at different transmit frequencies. The higher the network filling index, the more of reference vessels are present in the mapped vasculature from the imaging setup. Results in Figure 9 show that acquisition time is drastically reduced using smaller PSF volumes (or higher inverse PSF volumes). This means that a higher transmit frequency should be prioritized over a lower transmit frequency if the required penetration depth allows for it. Also, for a set acquisition time, depending on MB concentration and PSF volume, only a portion of total vasculature is mapped.



## 4.6 Limitations

This study set forth some limitations of the proposed simulation framework.

- A graph model was generated from 2PM, through automated segmentation, surface modeling and contraction. From that, MB trajectories were generated using MB velocities and number of MB as a function of diameter from two models derived from in-vivo data. This approach guarantees anatomically-realistic modelling since vasculature is derived from an ex-vivo model. Another avenue would consist of generating a fully synthetic fluid flow-driven graph model as in [38], where vasculature is generated using constraining parameters, namely vascular resistance, diameter, pressure, and bifurcation position. Whole cortical circulation can be generated while distinguishing between arterial and venal flow. This framework combines anatomical data with artificial construction laws to overcome limitations in coverage and resolution in reference anatomical data.
- In ultrasound localization microscopy, there are many parameters that can influence SNR, contrast, resolution, network filling and so forth, hence influencing the accuracy of the vascular reconstruction. In this study, we chose parameters that are most closely linked to our ability to maintain isolated sources in a spatiotemporal referential as stated in [2]. For that reason, we focused primarily on MB concentration [7] and transmit frequency [6].
- In Figure 4, variability in the MB count vs vessel diameter is due to the specificity of the vascular network. The smaller the vascular network, the more significant this variability is. Variability in MB velocities vs vessel diameter can be due to abrupt vessel diameter change due to rough vascular segmentation, which can affect the accuracy of a MB's corresponding vessel diameter prediction.
- As for ultrasound signals, they were generated using either readily available or realistic ultrasound probes acquisition parameters. The rationale behind this was to assess current limitations and seek for optimal ULM parameters. White Gaussian noise was added in

radio frequency data to improve realism, but no tissue was modeled. Since PSF size and shape greatly influences our ability to precisely detect single MB events, any alteration to the PSF from higher noise or lower contrast from neighboring tissue could have an impact on MB localization and ultimately maximal MB concentration. Other studies with tissue modelling are therefore to be conducted with tissue modelling as in [39], [40].

- In Figure 6, we can see that thresholding does not completely prevent MB interactions, as depicted in the increasing localization error as a function of concentration. Therefore, correlation threshold must be selected wisely to maximize MB detection events for a fuller network while minimizing strongly interreacting MBs which is depicted as blurred vasculature in density maps.
- All simulations were conducted on networks of brain mice vasculature where MB flow reflected behavior from in-vivo data. However, the vascular networks were relatively small in terms of field of view. This means that MB trajectories are limited to a small range of vessel sizes (mainly small vessels). This reduced vessel size range increases inter-network variability which can be seen through results from Figure , where MB count variability is not proportional to the inverse of PSF volume. In the medium, MBs were spread uniformly to artificially cover a large portion of space, but realism could be improved by having access to a larger network and ultimately a whole brain or whole organ vasculature, where the vascular network is closer to real-life vascular size distribution, which will increase metrics repeatability.
- In subsequent studies, acquisition parameters such as number of compound angles [34], number of pulse cycles, pulse frequency modulation (chirp) [41], SNR, probe elements geometry, MB size distribution just to name a few could be interesting to better understand the underlying limitations of ULM and progress towards finding optimal imaging parameters.

## 4.7 Conclusion

In conclusion, we have developed a framework capable of characterizing ULM image formation algorithms. We described how to obtain virtual anatomically-realistic MB positions from 2PM data. We have shown and quantified the impact of concentration on MB localization and acquisition time. We quantified the link between maximal MB concentration and PSF volume. Standardized anatomically-realistic MB simulations could become a useful tool in the validation of an ULM imaging setup and the PSF volume a straightforward metric for a specific probe's acquisition parameters since it would define the appropriate MB concentration. In practice, we hope that these results can be used to achieve optimal vasculature reconstruction at lowest acquisition time for a specific imaging setup.

## 4.8 References

- [1] Rayleigh, “XXXI. Investigations in optics, with special reference to the spectroscope” London, Edinburgh, Dublin Philos. Mag. J. Sci., vol. 8, no. 49, pp. 261–274, 1879.
- [2] O. Couture, V. Hingot, B. Heiles, P. Muleki-Seya, and M. Tanter, “Ultrasound localization microscopy and super-resolution: A state of the art,” IEEE Trans. Ultrason. Ferroelectr. Freq. Control, vol. 65, no. 8, pp. 1304–1320, 2018.
- [3] E. Betzig et al., “Imaging intracellular fluorescent proteins at nanometer resolution,” Science (80-.), vol. 313, no. 5793, pp. 1642–1645, 2006.
- [4] C. Errico et al., “Ultrafast ultrasound localization microscopy for deep super-resolution vascular imaging,” Nature, vol. 527, no. 7579, pp. 499–502, 2015.
- [5] K. Christensen-Jeffries et al., “Super-resolution Ultrasound Imaging,” Ultrasound Med. Biol., vol. 1, no. 1, pp. 1–6, 2020.
- [6] Y. Desailly, J. Pierre, O. Couture, and M. Tanter, “Resolution limits of ultrafast ultrasound localization microscopy,” Phys. Med. Biol., vol. 60, no. 22, pp. 8723–8740, 2015.

- [7] V. Hingot, C. Errico, B. Heiles, L. Rahal, M. Tanter, and O. Couture, “Microvascular flow dictates the compromise between spatial resolution and acquisition time in Ultrasound Localization Microscopy,” *Sci. Rep.*, vol. 9, no. 1, p. 2456, 2019.
- [8] O. M. Viessmann, R. J. Eckersley, K. Christensen-Jeffries, M. X. Tang, and C. Dunsby, “Acoustic super-resolution with ultrasound and microbubbles,” *Phys. Med. Biol.*, vol. 58, no. 18, pp. 6447–6458, 2013.
- [9] M. A. O’Reilly and K. Hynynen, “A super-resolution ultrasound method for brain vascular mapping,” *Med. Phys.*, vol. 40, no. 11, pp. 1–7, 2013.
- [10] O. Couture, B. Besson, G. Montaldo, M. Fink, and M. Tanter, “Microbubble ultrasound super-localization imaging (MUSLI),” *IEEE Int. Ultrason. Symp. IUS*, pp. 1285–1287, 2011.
- [11] Y. Desailly, O. Couture, M. Fink, and M. Tanter, “Sono-activated ultrasound localization microscopy,” *Appl. Phys. Lett.*, vol. 103, no. 17, 2013.
- [12] B. Qian, R. F. Rudy, T. Cai, and R. Du, “Cerebral artery diameter in inbred mice varies as a function of strain,” *Front. Neuroanat.*, vol. 12, no. February, 2018.
- [13] B. Xiong et al., “Precise cerebral vascular atlas in stereotaxic coordinates of whole mouse brain,” *Front. Neuroanat.*, vol. 11, no. December, pp. 1–17, 2017.
- [14] K. A. Bohn et al., “Semi-automated Rapid Quantification of Brain Vessel Density Utilizing Fluorescent Microscopy,” *J Neurosci Methods*, no. 270, pp. 124–131, 2016.
- [15] F. Helmchen and W. Denk, “Deep tissue two-photon microscopy,” *Nat. Methods*, vol. 2, no. 12, pp. 932–940, 2005.
- [16] C. Lefort, “A review of biomedical multiphoton microscopy and its laser sources,” *J. Phys. D. Appl. Phys.*, vol. 50, no. 42, 2017.
- [17] T. Ragan et al., “Serial two-photon tomography: an automated method for ex-vivo mouse brain imaging,” *Physiol. Behav.*, vol. 176, no. 5, pp. 139–148, 2018.

- [18] P. Delafontaine-Martel, J. Lefebvre, P.-L. Tardif, B. I. Lévy, P. Pouliot, and F. Lesage, “Whole brain vascular imaging in a mouse model of Alzheimer’s disease with two-photon microscopy,” *J. Biomed. Opt.*, vol. 23, no. 07, p. 1, 2018.
- [19] R. Damseh et al., “A simulation study investigating potential diffusion-based MRI signatures of microstrokes,” *Sci. Rep.*, vol. 11, no. 1, pp. 0–11, 2021.
- [20] L. Milecki et al., “A Deep Learning Framework for Spatiotemporal Ultrasound Localization Microscopy,” *IEEE Trans. Med. Imaging*, vol. 40, no. 5, pp. 1428–1437, 2021.
- [21] E. Hardy, J. Porée, H. Belgharbi, C. Bourquin, F. Lesage, and J. Provost, “Sparse channel sampling for ultrasound localization microscopy (SPARSE-ULM),” *Phys. Med. Biol.*, 2021.
- [22] R. Damseh et al., “Automatic Graph-based Modeling of Brain Microvessels Captured with Two-Photon Microscopy,” *IEEE J. Biomed. Heal. Informatics*, vol. PP, no. c, p. 1, 2018.
- [23] L. Gagnon et al., “Quantifying the microvascular origin of bold-fMRI from first principles with two-photon microscopy and an oxygen-sensitive nanoprobe,” *J. Neurosci.*, vol. 35, no. 8, pp. 3663–3675, 2015.
- [24] S. Sakadžić et al., “Two-photon high-resolution measurement of partial pressure of oxygen in cerebral vasculature and tissue,” *Nat. Methods*, vol. 7, no. 9, pp. 755–759, 2010.
- [25] R. Damseh, P. Delafontaine-Martel, P. Pouliot, F. Cheriet, and F. Lesage, “Laplacian Flow Dynamics on Geometric Graphs for Anatomical Modeling of Cerebrovascular Networks,” *IEEE Trans. Med. Imaging*, vol. 40, no. 1, pp. 381–394, 2021.
- [26] J. Bergstra et al., “Theano: A CPU and GPU Math Expression Compiler,” *Proc. Python Sci. Comput. Conf.*, no. Scipy, pp. 1–7, 2010.
- [27] S. Rashad et al., “Epigenetic response of endothelial cells to different wall shear stress magnitudes: A report of new mechano-miRNAs,” *J. Cell. Physiol.*, vol. 235, no. 11, pp. 7827–7839, 2020.
- [28] J. Provost et al., “3D ultrafast ultrasound imaging in vivo,” *Phys. Med. Biol.*, vol. 59, no. 19, pp. L1–L13, 2014.

- [29] B. Heiles et al., “Ultrafast 3D Ultrasound Localization Microscopy using a  $32 \times 32$  Matrix Array,” *IEEE Trans. Med. Imaging*, vol. PP, pp. 1–1, 2019.
- [30] C. Rabut et al., “4D functional ultrasound imaging of whole-brain activity in rodents,” *Nat. Methods*, vol. 16, no. 10, pp. 994–997, 2019.
- [31] C. Brunner et al., “A Platform for Brain-Wide Functional Ultrasound Imaging and Analysis of Circuit Dynamics in Behaving Mice,” *SSRN Electron. J.*, pp. 1–15, 2020.
- [32] D. Garcia, “SIMUS : an open-source simulator for ultrasound imaging . Part I : theory & examples,” 2021.
- [33] A. Cigier, F. Varray, and D. Garcia, “SIMUS: an open-source simulator for ultrasound imaging. Part II: comparison with three popular simulators,” p. 6, 2021.
- [34] G. Montaldo, M. Tanter, J. Bercoff, N. Benez, and M. Fink, “Coherent plane-wave compounding for very high frame rate ultrasonography and transient elastography,” *IEEE Trans. Ultrason. Ferroelectr. Freq. Control*, vol. 56, no. 3, pp. 489–506, 2009.
- [35] L. R. Dice, “Measures of the Amount of Ecologic Association Between Species Author ( s ): Lee R . Dice Published by : Ecological Society of America Stable URL : <http://www.jstor.org/stable/1932409>,” *Ecology*, vol. 26, no. 3, pp. 297–302, 1945.
- [36] T. J. Sørensen, “Estimation of the mean floristic similarity between and within sets of vegetational relevés,” in *A method of establishing groups of equal amplitude in plant sociology based on similarity of species content and its application to analyses of the vegetation on Danish commons*, I. kommission hos E. M. København, Ed. 1948, pp. 1–34.
- [37] Y. Desailly, J. Pierre, O. Couture, and M. Tanter, “Resolution limits of ultrafast ultrasound localization microscopy,” *Phys. Med. Biol.*, vol. 60, no. 22, pp. 8723–8740, 2015.
- [38] A. Linniger, G. Hartung, S. Badr, and R. Morley, “Mathematical synthesis of the cortical circulation for the whole mouse brain-part I. theory and image integration,” *Comput. Biol. Med.*, 2019.

- [39] G. Pinton, “Ultrasound imaging of the human body with three dimensional full-wave nonlinear acoustics. Part 1: simulations methods,” arXiv, pp. 1–14, 2020.
- [40] G. Pinton, “Ultrasound imaging with three dimensional full-wave nonlinear acoustic simulations. Part 2: sources of image degradation in intercostal imaging,” arXiv, pp. 0–9, 2020.
- [41] S. Harput, “Use of chirps in medical ultrasound imaging,” The University of Leeds, 2012.

## Chapter 5 GENERAL DISCUSSION

This chapter presents a discussion on the specific objectives of this project by reflecting on potential betterments to the work conducted.

### **5.1 Develop an anatomically-realistic framework for the validation of Ultrasound Localization Microscopy in a mouse model.**

Having access to a simulation framework for the validation of ULM opens a few possibilities in the betterment of current practices.

For example, it could be used to assess the performance of MB tracking algorithms. This could be done by introducing incomplete or random microbubble trajectories and assessing the ability of the tracking algorithm to recover the original trajectories.

As for machine learning, availability of reference data is an issue. MB flow from this work can hence be used to create reference maps for the training and validation of ULM frameworks based on neural networks [107].

This simulation framework could also be used to develop and improve in vitro-phantoms. A 3D model of the vasculature could be extracted and printed in a soluble material, which could be dissolved to create a wall-less phantom. Input and output ports however must be mitigated to allow for fluid flow in every vessel. Results from the in-vitro phantom can be compared with reference metrics obtained from simulation results.

In terms of biomarker development, this framework could be used to generate groups of healthy and abnormal flow datasets. These could be differentiated according to metrics such as vascular density, hemodynamic response, vessel stiffness, vessel tortuosity and pulsatility just to name a few. Moreover, these metrics should ideally be presented with spatial information, such that a local abnormality could be differentiated from surrounding tissue.

As for limitations of the current framework, they are discussed below with avenues for betterment.

As for microbubbles' velocities and distribution, they follow realistic behavior from in-vivo data. However, since it was based on a rodent model, the results, as they are, accurately depict rodent behavior. However, for other animal models, a similar study on blood velocity and microbubble distribution would be needed to confirm microbubble behavior for that specific model. The



experiment would consist of in-vivo imaging of individual microbubbles and measuring their velocity and corresponding vessel diameter as was done in [6].

Concerning the graph models, since the vascular networks were relatively small, there was only one inlet blood vessel supplying flow to the smaller ones and the graph model was a tree graph, which means that there were no recirculation and loops in the graph. Future larger datasets will most probably contain multiple input blood vessels and loops which will have to be accounted for.

As for flow, it was modelled as being laminar and exhibiting a Poiseuille velocity distribution, which results in faster flow in the center of the vessel and a slower flow close to the vessel wall. For the smaller capillaries, where sometimes only one microbubble can fit in the vessel, modelling should be modified to be limited to a single velocity for a certain diameter range, or a more realistic behavior accounting for more realistic interactions between the microbubble and the surrounding vessel when the microbubble is in the order of the vessel size.

Lastly, the modelled pulsatility wave propagation is currently a constant velocity extracted from the literature. Future work could include a pulsatility wave propagation that is function of vessel diameter and ideally function of age, vessel stiffness, patient medical condition, just to name a few. The simplest implementation would consist of combining all mentioned parameters into a function of vessel diameter for the velocity distribution.

## **5.2 Establish a link between optimal MB concentration and acquisition parameters of an imaging setup.**

In our example application, we established a link between microbubble concentration and PSF volume for transmit frequencies in the 3-15 MHz range for a matrix array. This can be leveraged to predict the performance of an imaging setup. With fewer unknown variables, less testing must be conducted for a specific experiment. Hence, this could reduce the number of required animals for a study. Moreover, as we saw in section 4.4.2, optimal MB concentration range is narrower for lower transmit frequencies. Therefore, it would be difficult to find an optimal MB concentration only using a trial-and-error method for deep vascular imaging. Therefore, this could possibly allow

for smaller vessels reconstruction. Since small vascular lesions have been linked with tissue disfunction [26], this could lead to more sensitive biomarkers.

A discussion on limitations is presented below.

The relationship between optimal MB concentration and PSF volume could benefit from further work where other acquisition parameters are studied, such as the effect of transducer shape, such as the sparse spiral array as in [117] or row-column as in [48] to ultimately generalize to any 3D-capable ultrasound imaging probe. SNR and contrast of such probes in simulation must match SNR and contrast in in-vivo experiments.

As for the simulation medium, white gaussian noise was added to RF data to a level similar to in-vivo data. However, it would be beneficial to add tissue modelling as in [115], where SNR and contrast would be affected by more realistic wave interference. Clutter would also be present and caused by blood vessels or other anechoic or hypoechoic regions modelled in the tissue [118]. This would most probably reduce the predicted microbubble concentration since they would be more difficult to localize for a certain PSF of the imaging system.

Moreover, since the impulse response of the system is non uniform throughout the field of view, unique microbubble positions were distributed across a larger region, but the microbubbles were simulated using the same vascular network. By doing so, we can better assess the variability in the field of view, but we expect that with a larger vascular dataset (as a whole brain) with a larger vessel size distribution, the study would account for more varied and realistic microbubble interactions, which would result in a more robust relationship with lower microbubble concentration variability.

Lastly, since ultrasound localization microscopy would ultimately be used to develop novel biomarkers, this framework could be used to compare healthy and unhealthy vasculature. Implementation would consist of either two vascular datasets or prior knowledge on vascular morphology to transform a healthy dataset into an unhealthy one. The biomarker would have to be extracted from the output microbubble positions at the end of the ULM pipeline and be significantly different for the unhealthy group compared to the healthy one.

## Chapter 6 **CONCLUSION AND RECOMMENDATIONS**

This project has led to the development of the first anatomically and hemodynamically realistic simulation framework for ultrasound localization microscopy for the validation of image-formation algorithms. After conducting an example parametric study on microbubble concentration and probe transmit frequency, we established a relationship between the maximal microbubble concentration and the inverse point spread function volume. In the process, we proposed significant innovations in terms of flow modelling and validation pipeline. The proposed framework can be leveraged for a variety of vascular networks to conduct parametric studies while quantifying the performance of the imaging system. The validation of an imaging system is as reliable as the validating framework. In this case, robustness of the validation can be related to the fidelity of reference vasculature and ultrasound simulation. For that reason, we suggest that future work is globally oriented towards using a large reference dataset, adding tissue-like interaction in the simulation medium to reduce variability and enhance real-world fidelity, and generating normal and abnormal flows where pulsatility could be modulated to simulate different stages of atherosclerosis.

The potential application of this simulation framework on human datasets would represent a natural culmination of this work. Ultrasound localization microscopy was recently performed on human subjects in 2D and will soon be possible in 3D, where validation of such imaging systems will be essential for their acceptance and success in the clinic.

This project is therefore a natural fit in biomedical engineering, where technical developments are matched with validation counterparts for the betterment of medical practices.

## REFERENCES

- [1] K. Seitz and D. Strobel, “A Milestone: Approval of CEUS for Diagnostic Liver Imaging in Adults and Children in the USA,” *Ultraschall der Medizin*, vol. 37, no. 3, pp. 229–232, 2016.
- [2] Rayleigh, “ XXXI. Investigations in optics, with special reference to the spectroscope ,” *London, Edinburgh, Dublin Philos. Mag. J. Sci.*, vol. 8, no. 49, pp. 261–274, 1879.
- [3] C. Errico *et al.*, “Ultrafast ultrasound localization microscopy for deep super-resolution vascular imaging,” *Nature*, vol. 527, no. 7579, pp. 499–502, 2015.
- [4] Y. Desailly, J. Pierre, O. Couture, and M. Tanter, “Resolution limits of ultrafast ultrasound localization microscopy,” *Phys. Med. Biol.*, vol. 60, no. 22, pp. 8723–8740, 2015.
- [5] O. Couture, V. Hingot, B. Heiles, P. Muleki-Seya, and M. Tanter, “Ultrasound localization microscopy and super-resolution: A state of the art,” *IEEE Trans. Ultrason. Ferroelectr. Freq. Control*, vol. 65, no. 8, pp. 1304–1320, 2018.
- [6] V. Hingot, C. Errico, B. Heiles, L. Rahal, M. Tanter, and O. Couture, “Microvascular flow dictates the compromise between spatial resolution and acquisition time in Ultrasound Localization Microscopy,” *Sci. Rep.*, vol. 9, no. 1, p. 2456, 2019.
- [7] K. Christensen-Jeffries, R. J. Browning, M. Tang, C. Dunsby, and R. J. Eckersley, “In Vivo Acoustic Super-Resolution and Super-Resolved Velocity Mapping Using Microbubbles,” *IEEE Trans. Med. Imaging*, vol. 34, no. 2, pp. 433–440, Feb. 2015.
- [8] T. Opacic *et al.*, “Motion model ultrasound localization microscopy for preclinical and clinical multiparametric tumor characterization,” *Nat. Commun.*, vol. 9, no. 1, pp. 1–13, 2018.
- [9] D. Ghosh *et al.*, “Super-Resolution Ultrasound Imaging of Skeletal Muscle Microvascular Dysfunction in an Animal Model of Type 2 Diabetes,” *J. Ultrasound Med.*, vol. 38, no. 10, pp. 2589–2599, 2019.
- [10] J. Foiret, H. Zhang, T. Ilovitsh, L. Mahakian, S. Tam, and K. W. Ferrara, “Ultrasound localization microscopy to image and assess microvasculature in a rat kidney,” *Sci. Rep.*,

- vol. 7, no. 1, pp. 1–12, 2017.
- [11] F. Lin, S. E. Shelton, D. Espíndola, J. D. Rojas, G. Pinton, and P. A. Dayton, “3-D ultrasound localization microscopy for identifying microvascular morphology features of tumor angiogenesis at a resolution beyond the diffraction limit of conventional ultrasound,” *Theranostics*, vol. 7, no. 1, pp. 196–204, 2017.
  - [12] T. M. Kierski *et al.*, “Superharmonic Ultrasound for Motion-Independent Localization Microscopy: Applications to Microvascular Imaging from Low to High Flow Rates,” *IEEE Trans. Ultrason. Ferroelectr. Freq. Control*, vol. 67, no. 5, pp. 957–967, 2020.
  - [13] R. J. G. van Sloun *et al.*, “Super-resolution Ultrasound Localization Microscopy through Deep Learning,” 2018.
  - [14] X. Liu, T. Zhou, M. Lu, Y. Yang, Q. He, and J. Luo, “Deep Learning for Ultrasound Localization Microscopy,” *IEEE Trans. Med. Imaging*, vol. 39, no. 10, pp. 3064–3078, Oct. 2020.
  - [15] Y. Yang *et al.*, “Assessment of Diabetic Kidney Disease Using Ultrasound Localization Microscopy: An in Vivo Feasibility Study in Rats,” in *2018 IEEE International Ultrasonics Symposium (IUS)*, 2018, pp. 1–4.
  - [16] P. Song *et al.*, “Improved Super-Resolution Ultrasound Microvessel Imaging with Spatiotemporal Nonlocal Means Filtering and Bipartite Graph-Based Microbubble Tracking,” *IEEE Trans. Ultrason. Ferroelectr. Freq. Control*, vol. 65, no. 2, pp. 149–167, 2018.
  - [17] J. Zhu *et al.*, “3D super-resolution US imaging of rabbit lymph node vasculature in vivo by using microbubbles,” *Radiology*, vol. 291, no. 3, pp. 642–650, 2019.
  - [18] J. Yu, L. Lavery, and K. Kim, “Super-resolution ultrasound imaging method for microvasculature in vivo with a high temporal accuracy,” *Sci. Rep.*, vol. 8, no. 1, pp. 1–11, 2018.
  - [19] M. R. Lowerison, C. Huang, F. Lucien, S. Chen, and P. Song, “Ultrasound localization microscopy of renal tumor xenografts in chicken embryo is correlated to hypoxia,” *Sci. Rep.*,

- vol. 10, no. 1, pp. 1–13, 2020.
- [20] C. Huang *et al.*, “Short Acquisition Time Super-Resolution Ultrasound Microvessel Imaging via Microbubble Separation,” *Sci. Rep.*, vol. 10, no. 1, pp. 1–13, 2020.
  - [21] S. Dencks *et al.*, “Clinical Pilot Application of Super-Resolution US Imaging in Breast Cancer,” *IEEE Trans. Ultrason. Ferroelectr. Freq. Control*, vol. 66, no. 3, pp. 517–526, 2019.
  - [22] C. Huang *et al.*, “Super-resolution ultrasound localization microscopy based on a high frame-rate clinical ultrasound scanner: An in-human feasibility study,” *Phys. Med. Biol.*, vol. 66, no. 8, 2021.
  - [23] E. Kanoulas *et al.*, “Super-Resolution Contrast-Enhanced Ultrasound Methodology for the Identification of In Vivo Vascular Dynamics in 2D,” *Invest. Radiol.*, vol. 54, no. 8, pp. 500–516, 2019.
  - [24] S. Harput *et al.*, “Two-Stage Motion Correction for Super-Resolution Ultrasound Imaging in Human Lower Limb,” *IEEE Trans. Ultrason. Ferroelectr. Freq. Control*, vol. 65, no. 5, pp. 803–814, 2018.
  - [25] C. Demené *et al.*, “Transcranial ultrafast ultrasound localization microscopy of brain vasculature in patients,” *Nat. Biomed. Eng.*, vol. 5, no. 3, pp. 219–228, 2021.
  - [26] E. E. Smith, J. A. Schneider, J. M. Wardlaw, and S. M. Greenberg, “Cerebral microinfarcts: The invisible lesions,” *Lancet Neurol.*, vol. 11, no. 3, pp. 272–282, 2012.
  - [27] Y. Shi and A. W. Toga, “Connectome imaging for mapping human brain pathways,” *Mol. Psychiatry*, vol. 22, no. 9, pp. 1230–1240, 2017.
  - [28] M. R. T. Sinke *et al.*, “Diffusion MRI-based cortical connectome reconstruction: dependency on tractography procedures and neuroanatomical characteristics,” *Brain Struct. Funct.*, vol. 223, no. 5, pp. 2269–2285, 2018.
  - [29] B. Jeurissen, M. Descoteaux, S. Mori, and A. Leemans, “Diffusion MRI fiber tractography of the brain,” *NMR Biomed.*, vol. 32, no. 4, pp. 1–22, 2019.
  - [30] C. H. Yeh, D. K. Jones, X. Liang, M. Descoteaux, and A. Connelly, “Mapping Structural

- Connectivity Using Diffusion MRI: Challenges and Opportunities,” *J. Magn. Reson. Imaging*, pp. 1–17, 2020.
- [31] P. Delafontaine-Martel, J. Lefebvre, P.-L. Tardif, B. I. Lévy, P. Pouliot, and F. Lesage, “Whole brain vascular imaging in a mouse model of Alzheimer’s disease with two-photon microscopy,” *J. Biomed. Opt.*, vol. 23, no. 07, p. 1, 2018.
  - [32] R. Damseh *et al.*, “Automatic Graph-based Modeling of Brain Microvessels Captured with Two-Photon Microscopy,” *IEEE J. Biomed. Heal. Informatics*, vol. PP, no. c, p. 1, 2018.
  - [33] L. Zagorchev *et al.*, “Micro computed tomography for vascular exploration,” *J. Angiogenes. Res.*, vol. 2, no. 1, pp. 1–11, 2010.
  - [34] B. Lemasson, S. Valable, R. Farion, A. Krainik, C. Rémy, and E. L. Barbier, “In vivo imaging of vessel diameter, size, and density: A comparative study between MRI and histology,” *Magn. Reson. Med.*, vol. 69, no. 1, pp. 18–26, 2013.
  - [35] K. A. Bohn *et al.*, “Semi-automated Rapid Quantification of Brain Vessel Density Utilizing Fluorescent Microscopy,” *J Neurosci Methods*, no. 270, pp. 124–131, 2016.
  - [36] S. Tang *et al.*, “Kalman Filter-Based Microbubble Tracking for Robust Super-Resolution Ultrasound Microvessel Imaging,” *IEEE Trans. Ultrason. Ferroelectr. Freq. Control*, vol. 67, no. 9, pp. 1738–1751, 2020.
  - [37] C. Bourquin, J. Porée, F. Lesage, and J. Provost, “Brain-wide pulsatility mapping with gated ultrasound localization microscopy in vivo,” *J. Acoust. Soc. Am.*, vol. 146, no. 4, pp. 3031–3031, Oct. 2019.
  - [38] S. Harput *et al.*, “Quantitative microvessel analysis with 3-D super-resolution ultrasound and velocity mapping,” *IEEE Int. Ultrason. Symp. IUS*, vol. 2020-Sept, pp. 5–8, 2020.
  - [39] I. G. Newsome *et al.*, “Implementation of a novel 288-element dual-frequency array for acoustic angiography: in vitro & in vivo characterization,” *IEEE Trans. Ultrason. Ferroelectr. Freq. Control*, vol. 3010, no. c, pp. 1–1, 2021.
  - [40] O. M. Viessmann, R. J. Eckersley, K. Christensen-Jeffries, M. X. Tang, and C. Dunsby, “Acoustic super-resolution with ultrasound and microbubbles,” *Phys. Med. Biol.*, vol. 58,

- no. 18, pp. 6447–6458, 2013.
- [41] M. A. O'Reilly and K. Hynynen, "A super-resolution ultrasound method for brain vascular mapping," *Med. Phys.*, vol. 40, no. 11, pp. 1–7, 2013.
  - [42] O. Couture, B. Besson, G. Montaldo, M. Fink, and M. Tanter, "Microbubble ultrasound super-localization imaging (MUSLI)," *IEEE Int. Ultrason. Symp. IUS*, pp. 1285–1287, 2011.
  - [43] Y. Desailly, O. Couture, M. Fink, and M. Tanter, "Sono-activated ultrasound localization microscopy," *Appl. Phys. Lett.*, vol. 103, no. 17, 2013.
  - [44] K. T. Dussik, "Über die Möglichkeit, hochfrequente mechanische Schwingungen als diagnostisches Hilfsmittel zu verwerten," *Zeitschrift für die gesamte Neurol. und Psychiatr. Vol.*, vol. 174, pp. 153–168, 1942.
  - [45] S. J. Kleinman and J. E. Rabiner, *Diagnostic ultrasound*. 2017.
  - [46] W. L. Yang, *Atlas of Human Body Ultrasound Scanning*. Singapore: Springer Singapore, 2018.
  - [47] C. Rabut *et al.*, "4D functional ultrasound imaging of whole-brain activity in rodents," *Nat. Methods*, vol. 16, no. 10, pp. 994–997, 2019.
  - [48] J. Sauvage *et al.*, "4D Functional Imaging of the Rat Brain Using a Large Aperture Row-Column Array," *IEEE Trans. Med. Imaging*, vol. 39, no. 6, pp. 1884–1893, 2020.
  - [49] D. L. Miller, N. B. Smith, M. R. Bailey, G. J. Czarnota, K. Hynynen, and I. R. S. Makin, "Overview of therapeutic ultrasound applications and safety considerations," *J. Ultrasound Med.*, vol. 31, no. 4, pp. 623–634, 2012.
  - [50] E. Maloney and J. H. Hwang, "Emerging HIFU applications in cancer therapy," *Int. J. Hyperth.*, vol. 31, no. 3, pp. 302–309, 2015.
  - [51] M. K. Turagam *et al.*, "Automated Noncontact Ultrasound Imaging and Ablation System for the Treatment of Atrial Fibrillation: Outcomes of the First-in-Human VALUE Trial," *Circ. Arrhythmia Electrophysiol.*, no. March, 2020.
  - [52] E. E. Konofagou, Y.-S. Tunga, J. Choia, T. Deffieuxa, B. Baseria, and F. Vlachosa,



- “Ultrasound-Induced Blood-Brain Barrier Opening,” *Curr. Pharm. Biotechnol.*, vol. 13, no. 7, pp. 1332–1345, 2012.
- [53] H. A. S. Kamimura, A. Conti, N. Toschi, and E. E. Konofagou, “Ultrasound neuromodulation: Mechanisms and the potential of multimodal stimulation for neuronal function assessment,” *Front. Phys.*, vol. 8, no. May, pp. 1–9, 2020.
- [54] J. E. Lingeman, J. A. McAteer, E. Gnessin, and A. P. Evan, “Shock wave lithotripsy: advances in technology and technique,” *Nat. Rev. Urol.*, vol. 6, no. 12, pp. 660–670, Dec. 2009.
- [55] K. B. Bader, G. Bouchoux, and C. K. Holland, “Sonothrombolysis,” in *Physiology & behavior*, vol. 176, no. 1, 2016, pp. 339–362.
- [56] I. Donald, J. Macvicar, and T. . Brown, “INVESTIGATION OF ABDOMINAL MASSES BY PULSED ULTRASOUND,” *Lancet*, vol. 271, no. 7032, pp. 1188–1195, Jun. 1958.
- [57] C. E. Brennen, “Cavitation in medicine,” *Interface Focus*, vol. 5, no. 5, pp. 1–12, 2015.
- [58] S. Harput *et al.*, “3-D Super-Resolution Ultrasound Imaging with a 2-D Sparse Array,” *IEEE Trans. Ultrason. Ferroelectr. Freq. Control*, vol. 67, no. 2, pp. 269–277, 2020.
- [59] K. J. Parker, “Correspondence: Apodization and windowing functions,” *IEEE Trans. Ultrason. Ferroelectr. Freq. Control*, vol. 60, no. 6, pp. 1263–1271, 2013.
- [60] J. A. Jensen and N. B. Svendsen, “Calculation of pressure fields from arbitrarily shaped, apodized, and excited ultrasound transducers,” *IEEE Trans. Ultrason. Ferroelectr. Freq. Control*, vol. 39, no. 2, pp. 262–267, Mar. 1992.
- [61] V. Perrot, “Ultrafast ultrasound imaging for simultaneous extraction of flow and arterial wall motion with linear array probe,” Universite de Lyon, 2019.
- [62] G. E. Tupholme, “Generation of acoustic pulses by baffled plane pistons,” *Mathematika*, vol. 16, no. 2, pp. 209–224, 1969.
- [63] P. R. Stepanishen, “Travel Time Across the Piston,” *J. Acoust. Soc. Am.*, no. February, pp. 1629–1638, 1970.
- [64] J. A. Jensen, “Deconvolution of Ultrasound Images,” *Ultrason. Imaging*, vol. 14, no. 1, pp.

1–15, Jan. 1992.

- [65] J. A. Jensen, “New approach to calculating spatial impulse responses,” *Proc. IEEE Ultrason. Symp.*, vol. 2, pp. 1755–1759, 1997.
- [66] V. Hingot, “Development of ultrasound localization microscopy to measure cerebral perfusion during stroke : a study in mouse models prior to its translation in humans,” Sorbonne University, 2021.
- [67] J. Porée, “Évaluation de la biomécanique cardiovasculaire par élastographie ultrasonore non-invasive,” Université de Montréal Faculté, 2016.
- [68] B. Delannoy, R. Torguet, C. Bruneel, E. Bridoux, J. M. Rouvaen, and H. Lasota, “Acoustical image reconstruction in parallel-processing analog electronic systems,” *J. Appl. Phys.*, vol. 50, no. 5, pp. 3153–3159, 1979.
- [69] D. Shattuck, M. D. Weinshenker, S. W. Smith, and O. T. von Ramm, “Explososcan: A parallel processing technique for high speed ultrasound imaging with linear phased arrays,” *J. Acoust. Soc. Am.*, vol. 75, no. 4, pp. 1273–1282, 1984.
- [70] L. Sandrin, S. Catheline, M. Tanter, X. Hennequin, and M. Fink, “Time-resolved pulsed elastography with ultrafast ultrasonic imaging,” *Ultrason. Imaging*, vol. 21, no. 4, pp. 259–272, 1999.
- [71] J. Vappou, J. Luo, and E. E. Konofagou, “Pulse wave imaging for noninvasive and quantitative measurement of arterial stiffness in vivo,” *Am. J. Hypertens.*, vol. 23, no. 4, pp. 393–398, 2010.
- [72] J. Provost, W. N. Lee, K. Fujikura, and E. E. Konofagou, “Imaging the electromechanical activity of the heart in vivo,” *Proc. Natl. Acad. Sci. U. S. A.*, vol. 108, no. 21, pp. 8565–8570, 2011.
- [73] J. Provost *et al.*, “3D ultrafast ultrasound imaging in vivo,” *Phys. Med. Biol.*, vol. 59, no. 19, pp. L1–L13, 2014.
- [74] C. Rabut *et al.*, “4D functional ultrasound imaging of whole-brain activity in rodents,” *Nat. Methods*, vol. 16, no. 10, pp. 994–997, 2019.

- [75] G. Montaldo, M. Tanter, J. Bercoff, N. Benech, and M. Fink, "Coherent plane-wave compounding for very high frame rate ultrasonography and transient elastography," *IEEE Trans. Ultrason. Ferroelectr. Freq. Control*, vol. 56, no. 3, pp. 489–506, 2009.
- [76] B. Denarie *et al.*, "Coherent plane wave compounding for very high frame rate ultrasonography of rapidly moving targets," *IEEE Trans. Med. Imaging*, vol. 32, no. 7, pp. 1265–1276, 2013.
- [77] Verasonics, "Single Crystal High Frequency Linear Arrays," p. 98034, 2020.
- [78] K. Blaize *et al.*, "Functional ultrasound imaging of deep visual cortex in awake nonhuman primates," *Proc. Natl. Acad. Sci.*, no. 40, p. 201916787, 2020.
- [79] C. Brunner *et al.*, "A Platform for Brain-Wide Functional Ultrasound Imaging and Analysis of Circuit Dynamics in Behaving Mice," *SSRN Electron. J.*, pp. 1–15, 2020.
- [80] Y. Desailly, J. Pierre, O. Couture, and M. Tanter, "Resolution limits of ultrafast ultrasound localization microscopy," *Phys. Med. Biol.*, vol. 60, no. 22, pp. 8723–8740, 2015.
- [81] W. F. Walker and G. E. Trahey, "A fundamental limit on delay estimation using partially correlated speckle signals," *IEEE Trans. Ultrason. Ferroelectr. Freq. Control*, vol. 42, no. 2, pp. 301–308, Mar. 1995.
- [82] M. A. Transducers and M. A. Transducers, "Vantage<sup>TM</sup> Volume Vantage<sup>TM</sup> Volume," pp. 3–4.
- [83] R. Gramiak, P. M. Shah, and D. H. Kramer, "Ultrasound cardiography: contrast studies in anatomy and function," *Radiology*, vol. 92, no. 5, pp. 939–948, 1969.
- [84] G. M. Moore, "Cramming more components onto integrated circuits With unit cost," *Electronics*, vol. 38, no. 8, p. 114, 1965.
- [85] E. Betzig *et al.*, "Imaging intracellular fluorescent proteins at nanometer resolution," *Science* (80-. ), vol. 313, no. 5793, pp. 1642–1645, 2006.
- [86] K. Christensen-Jeffries *et al.*, "Super-resolution Ultrasound Imaging," *Ultrasound Med. Biol.*, vol. 1, no. 1, pp. 1–6, 2020.
- [87] B. Heiles *et al.*, "Ultrafast 3D Ultrasound Localization Microscopy using a 32×32 Matrix

- Array,” *IEEE Trans. Med. Imaging*, vol. PP, pp. 1–1, 2019.
- [88] M. Salih, S. M. Ali, N. Jena, and K. Ananthasubramaniam, “Review of ultrasound contrast agents in current clinical practice with special focus on DEFINITY® in cardiac imaging,” *Future Cardiol.*, vol. 17, no. 2, pp. 197–214, 2021.
  - [89] K. N. Kearns *et al.*, “The role of contrast-enhanced ultrasound in neurosurgical disease,” *Neurosurg. Focus*, vol. 47, no. 6, pp. 1–8, 2019.
  - [90] M. A. Borden and K. H. Song, “Reverse engineering the ultrasound contrast agent,” *Adv. Colloid Interface Sci.*, vol. 262, pp. 39–49, 2018.
  - [91] L. Hoff and P. C. Sontum, *Acoustic characterization of contrast agents for medical ultrasound imaging*, vol. 103, no. 5. 2001.
  - [92] M. I. Lantheus, “Definity - FULL PRESCRIBING INFORMATION,” 2018.
  - [93] T. Şen, O. Tüfekçioğlu, and Y. Koza, “Mechanical index,” *Anadolu Kardiyol. Derg.*, vol. 15, no. 4, pp. 334–336, 2015.
  - [94] V. Perrot, M. Polichetti, F. Varray, and D. Garcia, “So you think you can DAS? A viewpoint on delay-and-sum beamforming,” *Ultrasonics*, vol. 111, pp. 1–12, 2021.
  - [95] E. J. Candès, X. Li, Y. Ma, and J. Wright, “Robust principal component analysis?,” *J. ACM*, vol. 58, no. 3, 2011.
  - [96] J. Baranger, B. Arnal, F. Perren, O. Baud, M. Tanter, and C. Demene, “Adaptive Spatiotemporal SVD Clutter Filtering for Ultrafast Doppler Imaging Using Similarity of Spatial Singular Vectors,” *IEEE Trans. Med. Imaging*, vol. 37, no. 7, pp. 1574–1586, 2018.
  - [97] D. Ackermann and G. Schmitz, “Detection and tracking of multiple microbubbles in ultrasound B-mode images,” *IEEE Trans. Ultrason. Ferroelectr. Freq. Control*, vol. 63, no. 1, pp. 72–82, 2016.
  - [98] M. Antoniou *et al.*, “Biomarker-guided trials: Challenges in practice,” *Contemp. Clin. Trials Commun.*, vol. 16, no. July 2019, p. 100493, 2019.
  - [99] G. C. Kagadis *et al.*, “Medical imaging displays and their use in image interpretation,” *Radiographics*, vol. 33, no. 1, pp. 275–290, 2013.

- [100] S. Amur, L. Lavange, I. Zineh, S. Buckman-Garner, and J. Woodcock, “Biomarker qualification: Toward a multiple stakeholder framework for biomarker development, regulatory acceptance, and utilization,” *Clin. Pharmacol. Ther.*, vol. 98, no. 1, pp. 34–46, 2015.
- [101] O. Solomon, R. J. G. van Sloun, H. Wijkstra, M. Mischi, and Y. C. Eldar, “Exploiting flow dynamics for super-resolution in contrast-enhanced ultrasound,” pp. 1–11, 2018.
- [102] G. S. Alberti, H. Ammari, F. Romero, and T. Wintz, “Dynamic Spike Superresolution and Applications to Ultrafast Ultrasound Imaging,” *SIAM J. Imaging Sci.*, vol. 12, no. 3, pp. 1501–1527, Jan. 2018.
- [103] V. Hingot, C. Errico, M. Tanter, and O. Couture, “Subwavelength motion-correction for ultrafast ultrasound localization microscopy,” *Ultrasonics*, vol. 77, pp. 17–21, 2017.
- [104] P. Cormier, J. Poree, C. Bourquin, and J. Provost, “Dynamic Myocardial Ultrasound Localization Angiography,” *IEEE Trans. Med. Imaging*, vol. xx, no. X, pp. 1–1, 2021.
- [105] C. Kasai, K. Namekawa, A. Koyano, and R. Omoto, “Real-Time Two-Dimensional Blood Flow Imaging Using an Autocorrelation Technique,” *IEEE Trans. Sonics Ultrason.*, vol. 32, no. 3, pp. 458–464, 1985.
- [106] J. Zhang, X. Zhang, Y. Yang, Q. He, and J. Luo, “A deep learning method for reduction of microbubble accumulation time in ultrasound localization microscopy,” *IEEE Int. Ultrason. Symp. IUS*, vol. 2020-Sept, pp. 20–23, 2020.
- [107] L. Milecki *et al.*, “A Deep Learning Framework for Spatiotemporal Ultrasound Localization Microscopy,” *IEEE Trans. Med. Imaging*, vol. 40, no. 5, pp. 1428–1437, 2021.
- [108] T. Ye, N. Phan-Thien, and C. T. Lim, “Particle-based simulations of red blood cells—A review,” *J. Biomech.*, vol. 49, no. 11, pp. 2255–2266, 2016.
- [109] D. Markauskas, H. Kruggel-Emden, R. Sivanapillai, and H. Steeb, “Comparative study on mesh-based and mesh-less coupled CFD-DEM methods to model particle-laden flow,” *Powder Technol.*, vol. 305, pp. 78–88, 2017.
- [110] Z. Tyfa, D. Obidowski, P. Reorowicz, L. Stefańczyk, J. Fortuniak, and K. Jóźwik,

- “Numerical simulations of the pulsatile blood flow in the different types of arterial fenestrations: Comparable analysis of multiple vascular geometries,” *Biocybern. Biomed. Eng.*, vol. 38, no. 2, pp. 228–242, 2018.
- [111] C. Sun and L. L. Munn, “Lattice-Boltzmann simulation of blood flow in digitized vessel networks,” *Comput. Math. with Appl.*, vol. 55, no. 7, pp. 1594–1600, 2008.
- [112] L. Gagnon *et al.*, “Quantifying the microvascular origin of bold-fMRI from first principles with two-photon microscopy and an oxygen-sensitive nanoprobe,” *J. Neurosci.*, vol. 35, no. 8, pp. 3663–3675, 2015.
- [113] S. Sakadžić *et al.*, “Large arteriolar component of oxygen delivery implies a safe margin of oxygen supply to cerebral tissue,” *Nat. Commun.*, vol. 5, 2014.
- [114] T. P. Santisakultarm *et al.*, “In vivo two-photon excited fluorescence microscopy reveals cardiac- and respiration-dependent pulsatile blood flow in cortical blood vessels in mice,” *Am. J. Physiol. - Hear. Circ. Physiol.*, vol. 302, no. 7, pp. 1367–1377, 2012.
- [115] G. Pinton, “Ultrasound imaging with three dimensional full-wave nonlinear acoustic simulations. Part 2: sources of image degradation in intercostal imaging,” *arXiv*, pp. 0–9, 2020.
- [116] H. Belgharbi *et al.*, “An Anatomically and Hemodynamically Realistic Simulation Framework for 3D Ultrasound Localization Microscopy,” *bioRxiv*, pp. 2–10, 2021.
- [117] A. Ramalli, E. Boni, A. S. Savoia, and P. Tortoli, “Density-tapered spiral arrays for ultrasound 3-D imaging,” *IEEE Trans. Ultrason. Ferroelectr. Freq. Control*, vol. 62, no. 8, pp. 1580–1588, 2015.
- [118] M. A. Lediju, M. J. Pihl, J. J. Dahl, and G. E. Trahey, “Quantitative assessment of the magnitude, impact and spatial extent of ultrasonic clutter,” *Ultrason. Imaging*, vol. 30, no. 3, pp. 151–168, 2008.